Untersuchungen zur Mikrointegration optischer Übertragungssysteme im Kurzstreckenbereich

Inauguraldissertation
zur Erlangung des akademischen Grades
eines Doktors der Naturwissenschaften
der Universität Mannheim

vorgelegt von

Elektronik Ingenieur, M.Sc, José Fernando Merchán Alba
aus Bogotá D.C., Kolumbien

Mannheim, 2012

Dekan:	Prof. Dr. Heinz Jürgen Müller, Universität Mannheim
Referent:	Prof. Dr Karl-Heinz Brenner, Universität Heidelberg
Korreferent:	Prof. Dr Jürgen Jahns, FernUniversität in Hagen

Tag der mündlichen Prüfung: 10.10.2012

Abstract

The integration of optical micro-systems and high speed electronics has been of great interest in the last few years. Optical fibres offer attractive advantages for the transmission of information over distances, from a few centimetres up to some kilometres, but they also suffer from the accuracy requirements for the adjusting of coupling systems. In order to make more efficient, faster and smaller interconnects the application of MOEMS (Micro Opto-Electro-Mechanical Systems) to this type of communication systems is mandatory.

In this thesis, the integration of micro-optical and electronic devices is investigated. The contributions of the author are:

- Design of a novel optical micro-coupler: several mechanical and optical systems are embedded in a monolithic construction that facilitates the adjustment of the optical and electronic devices by using self-guiding structures.
- Implementation of a simulation tool using the angular spectrum method: the propagation of plane waves between tilted planes described by Brenner [36] was implemented in order to predict the characteristics of the optical coupler. With regard to the simulations, the adjusting systems were designed and constructed, and the fabrication accuracies for the optical coupler were set.
- Examination of GRIN-rod lenses properties: considering the focusing properties of this type of lenses, theoretical and laboratory results were compared in order to predict the improvement on the coupling efficiency by using the GRIN-rod lenses in the designed coupling concept.
- Fabrication of the optical coupler: based on the design and simulation results the optical coupler was manufactured using plastic replication of metal masters.
- Construction of an active optical cable (AOC): the microelectronic systems for the integration with the manufactured optical coupler were designed and fabricated.
- Design and construction of the integration system: a concept for the integration of the optical with the electronic systems was developed. The adjustment was simplified by including alignment structures in the design of the optical and electronic systems.
- Design and construction of a high speed video transfer system: to test the optical systems, electronic boards were designed and manufactured. The characteristics of the electrical transmission lines are determined for the specific design, and some strategies to minimise negative effects inherent to the construction are suggested.
- At the end of the thesis, some forward-looking models are presented, to show how the concept could be implemented in the future.

Zusammenfassung

Die Integration optischer Mikrosysteme und Hochgeschwindigkeitselektronik ist in den letzten Jahren von großem Interesse gewesen. Optische Faser bieten attraktive Vorteile für die Übertragung von Information über Abstände von einigen Zentimetern bis eineigen Kilometern, aber diese leiden unter den hohen Genauigkeitsanforderungen für die Justier- und Koppelsysteme. Um diese Verbindungen effizienter, schneller, und kleiner zu machen, die Anwendung von MOEMS (Micro Opto-Electro-Mechanical Systems) in dieser Art Kommunikationssysteme ist erforderlich.

Die Integration von mikro-optische- und elektronische Bauteile wird in dieser Doktorarbeit untersucht. Die Beiträge des Autors sind:

- Design eines neuartigen optischen Mikrokopplers: mehrere mechanische und optische Systeme wurden in einem monolithischen Konstrukt eingebettet, dass durch die Benutzung von selbstjustierenden Strukturen die Justage der optischen und elektronischen Bauteile vereinfacht.
- Implementierung eines auf der ”angular spectrum” Methode basierten Simulationswerkzeugs: die Ausbreitung von ebenen Wellen zwischen gekippten Flächen von Brenner [36], wurde implementiert um die Eigenschaften des optischen Kopplers vorherzusagen. Die Justiersysteme wurden unter Berücksichtigung der Simulationen gestalten und konstruiert. Die Fabrikationsgenauigkeitenwurden mithilfe der Simulation gesetzt.
- Untersuchung der Eigenschaften von GRIN-rod Linsen: um die Abbildeigenschaften dieser Linsen zu charakterisieren wurden theoretische- und Laborergebnisse verglichen. Die Effizienz des vorgestellten Koppelkonzeptes wurde durch die Benutzung von GRIN-rod Linsen erhöht.
- Fabrikation des optische Kopplers: der optische Koppler wurde unter Berücksichtigung der Simulationsergebnissen hergestellt.
- Konstriktion eines aktiven optischen Kabels (AOC): die mikroelektronische Systeme wurden erfolgreich mit den optischen Bauteilen integriert.
- Gestaltung und Konstruktion des Integrationssystems: ein Konzept zur Integration der optischen und elektronischen Bauteile wurde entworfen. Die Justage wurde durch die Integration von Justierelementen in das System vereinfacht.
- Gestaltung und Konstruktion eines Hochgeschwindigkeitsübertragungs-system: elektronische Systeme wurden gestalten und hergestellt um die optische Systeme zu überprüfen. Die Eigenschaften der elektrische Übertragungskanäle wurden für ein spezifisches Design festgestellt, und einige Strategien um die negative Einflusse zu vermeiden wurden vorgeschlagen.

Am Ende der Arbeit einige zukunftweisende Modelle werden präsentiert.

Contents

1. Introduction

In the modern world, the increasing demand for high-speed communication systems encourages the research of new approaches aimed at the faster and easier transmission of information, and the search for solutions that are applicable not only in complex computing centres or sensing systems but also in everyday situations.

The efforts of researchers and engineers for the design of faster and smaller systems are challenged by the physical limitations. Until 2006, Moore's law was maintained by making semi-conductor devices smaller. Consequently, the threshold voltages needed by a transistor to switch between states were reduced, resulting in an increase in its switching speed. For that time, single core processors supported a maximum clock rate of 2.6 GHz.

With the introduction of dual-core architecture in June 2007, another way to maintain the increase was implemented. Since clocking semi-conductors with high frequencies resulted in thermally inefficient and the requirements for the design became too complex, the devices were made smaller, but the clocking frequencies remained at a maximum of a few GHz. In order to be able to process more information, processors were placed in parallel.

Parallelisation is the key strategy for processing and transmitting more information. Modern logic devices such as FPGAs (Field Programmable Gate Array) are equipped with up to 32 high-speed channels, that are able to transmit and receive serial streams at bit-rates of up to 12.5 Gbps (Giga bits per second). The communication channel is often limited by the length of the electrical path and the electromagnetic noise in the environment. In most of cases, the signals cannot be transmitted over more than a few centimetres.

In cases in which the signal has to be transmitted over longer paths, the conversion from an electrical signal to an optical one, for its transmission over optical fibre, is inevitable. The systems used for this conversion are based on the VCSEL (Vertical Cavity Side Emitting Laser) and the PIN photodiode. Their mechanical and electro-optical properties make them attractive. Some of these include the small form factor, high efficiency and, nowadays, the availability of cost-effective arrays.

The purpose of this thesis is the study, design, construction and testing of a novel coupling concept, based on previous studies at the Chair of Optoelectronics, University of Heidelberg. It started with the idea of replicating micro-optical elements, using plastic moulding techniques from moulds that were fabricated using lithographic methods. In the work of Jahns et al [1] and Brenner et al [2] cost-effective methods for high quality replication of negative moulds, using PMMA (Polymethylmethacrylat), was demonstrated.

Moreover, the development of a new photoresist for the fabrication of DOE (Diffractive Optical Elements), and the dependency of their characteristics on mechanical and environmental parameters, were studied [3].

Studies were made in other areas, such as beam collimation and coupling systems for fibre optics on the basis of GRIN (Gradient Index) optics. Curiously, one of the motivations for the studies of Sinzinger et al [4] was the development of a cost-effective coupling system on the basis of edge emitting laser diodes because, at that time, the fabrication of side-emitting laser diodes demanded high technological efforts. Today, thanks to technological advances, VCSELs constitute the basis of almost all communication systems.

Furthermore, the optical chip to chip interconnections, based on GRIN, systems was studied by Moisel et al [5], and a solution for very short range interconnects, also using V-grooves, was purposed.

In the field of optical interconnects, the replacement of electrical- via optical waveguides has been studied, and some proposals concerning the interconnection of electronic chips with optical fibres [6], as well as initial studies of parallel interconnection for high bandwidth systems [7],[8], have been made.

In order to target the micro-integration of optical devices, some considerations about the importance of an accurate alignment of the different optical devices have been suggested [9]. Subsequently, some systems for the simplification of that alignment were constructed [10].

2. Electrical and optical interconnects

The ever growing user requirements for bandwidth of communication systems, and for the flexibility and reliability of digital data, set the criteria for choosing the technology that fits their needs. Whether in a supercomputer or on a private laptop these three characteristics describe the performance of digital systems.

A familiar example from the modern everyday life helps to understand these requirements:

A ten-minute video has become very popular on the Internet and a user wants to download and save it to his USB Stick.

Although the video is available in three different resolutions, the user 'tends' (just to consider that someone might prefer low definition video) to choose the high definition alternative. That is, the user wishes to watch 25 frames per second (the lowest frame rate) with a resolution of 1,920 x 1,080 pixels each. The raw data rate for RGB (Red Green Blue) video is about 1.2 Gbit/s. With data compression techniques this data rate is currently reduced to about 5 Mbit/s. It does not sound astonishing, but considering that popular videos have a request frequency of tens to hundreds of requests per minute, the server would need a bit rate of about 500 Mbit/s to serve to the requests for just one video. Measurements show that a unicast server[1] requires up to 8 Gbit/s and a multicast server up to 1.4 Gbit/s to serve only the video requests if the server contains 2,600 videos of low to average popularity [11]. Many of the downloads take up to one hour for a ten-minute HD video, and others are cancelled or not attended to. One of the causes of this inability to satisfy requirements is the low bandwidth of many servers, and those that manage to supply the demand might not be able to transfer uncompressed video.

Inside a server, the information is transferred from the hard disk to the processor and vice versa, or between the processor and the memory modules, and subsequently between the processor and communication busses i.e. PCIe (Peripheral Component Interconnect Express). Regarding the bit rate, the slowest component is the hard disk. A 15000 rpm disk reaches a bit rate of about 1.4 Gbit/s, without taking an access time of some milliseconds into account. Modern solid state hard drives reach up to 16 Gbit/s, as well as DDR3 and PCIe. The bandwidth of the different components inside a modern server are all comparable, but the actual bottleneck appears when the servers communicate among one another. They suffer from the same problem as other high speed electronic systems: the short range communication systems do not offer the required bandwidth.

Depending on the type, modern digital systems evolve and demand higher resolution, higher sampling rate, redundant information or, in some cases, all of these together. Examples of these are an array of cameras in a television studio, high-speed cameras and measurement systems that produce high data volumes. The huge

[1]A unicast server is able to send only one packet to another host. A multicast server is able to send a packet to a set of hosts.

amount of information produced in these devices has to be transferred to destinations that are usually not near the information source, so that normally it has to be transferred over distances that go from a few metres to several hundreds of metres for further analysis or visualisation. For this reason, the optical transmission systems constitute a solution to mane of the present problems of copper transmission lines: cross talk, electromagnetic compatibility, high losses, high weight and high costs.

The propagation of light in optical fibres is possible as a result of the total internal reflection of the beam inside the fibre. In this way, the energy is confined to the optical fibre and the optical signal experiences a very low attenuation, so that the transmission of digital signals at high data rates — currently some Gigabits a second — is achieved easily using optical fibres. However, if the physical barriers concerning bandwidth and attenuation are not set by the optical systems, what is the limiting factor?

The bottleneck in optical communication systems is the electronics. Before the signal is transmitted over fibre optics it suffers changes and is affected by factors that are inherent to the systems. Starting at the source, switching transistors are bandwidth limited by the parasitic capacitances on their junctions. Then, the electrical signal has to be transmitted over lossy media, passing from one device to the next in the presence of parasitic capacitance and inductance. The electrical signal is also distorted by reflections in the transmission lines and suffers an attenuation that depends on the length of the paths. After the signal is converted to an optical one it has to be coupled into the fibre. Unfortunately, this process is also not free of losses and the coupled signal intensity is limited by the efficiency of the coupling system.

The bandwidth of a communication system is defined as the amount of data that the system is able to transfer per time unit. The flexibility of the system is the ability to serve as the communication channel between different systems, and reliability is the ability of the communication system to transfer the requested information without losses or changes to the information.

In this chapter, the characteristics of the constructed optoelectronic communication system are described, emphasising the devices present in the short-range interconnect, such as electronic devices for the transmission and receipt of digital signals, coupled transmission lines on the PCB (Printed Circuit Board), and passive and parasitic elements. All these factors are described qualitatively and quantitatively so that the adopted measures to diminish them can be understood in further sections.

The signal flow in the constructed optoelectronic communication path is shown in Figure 1. The signal starts at the high-speed transistors of a FPGA (Field Programmable Gate Array), and is transmitted to the VCSEL-Driver over copper transmission lines and high-speed connectors. There, the offset and the amplitude of the electrical signal are adjusted to drive the laser diode correctly.

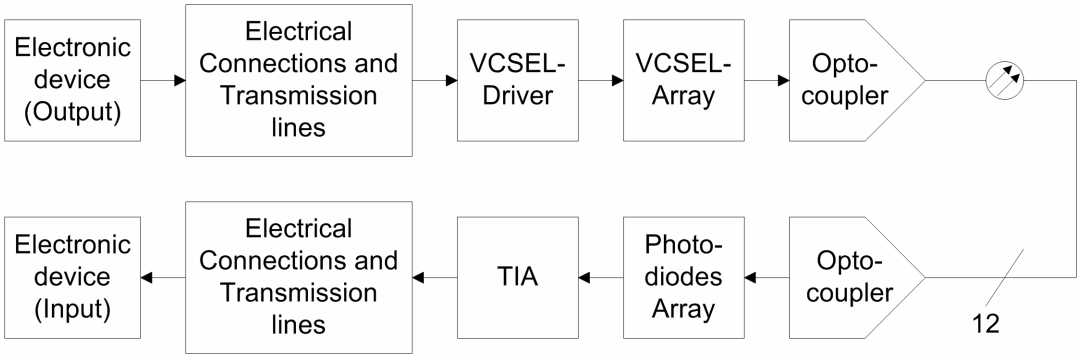

Figure 1. Block diagram of the constructed high speed communication path

The electrical signal is converted to an optical one by the VCSEL, then the optical signal is coupled into the fibre using an optical coupler, and the signal is transmitted optically. At the counterpart, the signal coming out from the fibre is coupled into the photodiode. There, the signal is converted to an electrical one. The electrical signal from the photodiode is amplified and transmitted over copper transmission lines to the FPGA that receives it for further processing.

2.1. Electrical interconnects

The development of telecommunications has been linked strongly with scientists' and engineers' understanding of electromagnetism. At the beginning of wired communications, a macroscopic description of the interaction of electromagnetic fields with conductive, dielectric and magnetic materials was sufficient for the development of the first wired communication. Karl Friedrich Gauss described the net flux of electric and magnetic fields in a closed surface at the same time as other scientists, such as Ampère, were working on the relationships between magnetic and electric fields. These laws and, for that period, complicated implementations of galvanometers and electromagnets were the basis for the first telegraph by Gauss and Weber in 1833, at the University of Göttingen. It can be considered as the first wired digital communication and, curiously, precedes any type of analogue communication.[2]

Inventions such as the telephone, television and computer, among others, have encouraged the development of electrical, electronic and optical systems, in order to enable high bandwidths for the transmission of information over long distances with wired connections. Nowadays a more accurate description of the interaction of electromagnetic fields with diverse electrical and electronic devices is mandatory, in order to predict the behaviour of modern systems designed to work at very high clock rates. Modern wired communication systems, on the basis of electrical transmission lines, offer a bandwidth of about 10 GHz over a coaxial cable of 1m length [12].

With the improvement of semi-conductor technologies, the size of the devices has been optimised to reduce the effect of transistor dimensions on the frequency

[2]The electromagnetic telegraph, J.B. Calvert.http://mysite.de.edu/~jcalvert/tel/morse.htm

performance of the devices. Often, the unity-gain frequency f_T is used as a figure of merit for the frequency behaviour of a device. This is the frequency at which the gain-bandwidth characteristic of the device crosses unity. Working at f_T the device can be considered as a short circuit.

The frequency f_T is inversely proportional to the dimensions of the transistors [13]. As already mentioned, current manufacture techniques have minimised the dimensions of the junctions so that the effect of parasitic capacitance can be neglected, compared to the effects relative to the layout [12].

The dependency of the bandwidth on the length of the transmission line, and the effect of parasitic frequency dependant capacitance and inductance on the behaviour of electric and electronic devices is treated in this section, on the basis of the description of electric microstructures and transmission lines at high frequencies. The understanding of the interaction of electromagnetic fields with microscopic electronic structures and electrical transmission lines allows the identification of physical barriers for the high-speed transmission of data in this type of system, with regard to the frequency and quality of the signal.

2.1.1. Physical Barriers

Every system is a compound of many elements, some of them unwanted. In the case of an electronic high speed circuit, there are energy storing elements, decoupling devices, transmission lines and semiconductors that are placed very close to each other. Each of them has a frequency dependant response that is limited by physical factors. In this section, each of the desired and also of the parasitic players in the interconnection is explained individually.

2.1.1.1 Ordinary Capacitance

Between two conducting bodies that are charged to different electric potentials there is always an electric field. The reluctance of the voltage, which is proportional to the electric field, to build up or to decay quickly in response to injected power is called 'capacitance' [14]. Before expressing the last sentence mathematically, two parallel conductive plates will serve as example, in order to solve the equation that describes the electric potential between them.

In the charge-free region the potential is:

$$\nabla^2 V = \frac{\partial^2 V}{\partial z^2} = 0 \tag{2.1}$$

The solution is the linear function,

$$V(z) = \frac{V_0}{d} z \tag{2.2}$$

where V_0 is the total potential and d is the distance between the plates.
The electric field is given by:

$$E = -\nabla V \tag{2.3}$$

Thus is the electric field inside the plates constant,

$$\vec{E} = -\frac{V_0}{d}\hat{k} \tag{2.4}$$

Where $\hat{k}$ is the unitary vector perpendicular to the plates.
According to Gauss' law, the normal component of the electric flux density is equal to the charge density on the plates,

$$\vec{D} \cdot \hat{n} = \varepsilon_r \varepsilon_0 \vec{E} \cdot \hat{n} = \sigma \tag{2.5}$$

where ε_r is the relative permittivity of the dielectric between the plates and ε_0 is the permittivity of vacuum in Farad per meter (F/m). The absolute value (the direction of the field can be positive or negative) of the charge density on one of the plates is,

$$\sigma = \left|\vec{D} \cdot \hat{n}\right| = \left|\varepsilon_r \varepsilon_0 \vec{E} \cdot \hat{k}\right| = \varepsilon_r \varepsilon_0 \frac{V_0}{d} \tag{2.6}$$

The total charge on one plate is

$$q = \sigma A = \varepsilon_r \varepsilon_0 A \frac{V_0}{d} \tag{2.7}$$

where A is the area of one of the parallel plates. The constant $\frac{\varepsilon_r \varepsilon_0 A}{d}$ is the capacitance of the two plates and is defined as the ability of the two plates to store energy in form of an electric field.

In general, for two conductors of any shape, the capacitance is defined as:

$$C_{12} = \frac{q}{V_{12}} \tag{2.8}$$

where C_{12} is the capacitance and V_{12} the electric potential between the two conductors.

This equation can be expressed in terms of the corresponding time derivatives as:

$$\frac{dq}{dt} = I = C\frac{dV}{dt} \tag{2.9}$$

and shows that an instantaneous change on the current does not cause an instantaneous change on the electric potential. That is called in the bibliography: the reluctance of the voltage to make quick power changes.

The ordinary capacitance is present in passive devices that are designed for storing energy or decoupling signals, as well as in transmission lines, electrical contacts and pads as parasitics.

2.1.1.2 Capacitance of junctions

In a p-n semiconductor junction there is a capacitance due to the charge of dopants near the depletion region. It is the junction or depletion capacitance.
In the section 2 was shown that the capacitance is defined as

$$C = \frac{dq}{dV} \tag{2.10}$$

The distribution of carriers is given by Boltzmann statistics and states that the carrier distribution is nearly constant inside the depletion region.

$$\rho(x) = -q_e N_A \quad -x_{p0} < x < 0 \tag{2.11}$$

For the acceptors' (holes) density inside the depletion region in the p-doped material x_{p0}. q_e is the electric charge of the electron and N_A the total number of holes. For the donors density, the expression is identical with the corresponding sub indices.

The charge per unit area is given by

$$Q_A = \frac{Q}{A} = x_{p0} N_A q_e \tag{2.12}$$

The depletion region is defined as:

$$x_{p0} = \sqrt{\frac{2\varepsilon}{q_e N_A}(V_D - V)\left(\frac{N_D}{N_D + N_A}\right)} \tag{2.13}$$

where V_D is the junction voltage, ε the permittivity of the semiconductor and N_A the total number of electrons in the depletion region, at the n-material side of the junction.

The capacitance can be calculated as:

$$\begin{aligned} C = \frac{dq}{dV} &= \frac{d\left(N_A q_e \sqrt{\frac{2\varepsilon}{q_e N_A}(V_D - V)\left(\frac{N_D}{N_D + N_A}\right)}\right)}{dV} \\ &= q_e \left(\frac{1}{N_D} + \frac{1}{N_A}\right)^{-1/2} \left(\frac{2\varepsilon}{q_e}\right)^{1/2} \frac{1}{2}\left(\frac{-1}{\sqrt{V_D - V}}\right) \end{aligned} \tag{2.14}$$

Depletion capacitances are only present in reverse biased junctions, and are very small compared to parasitic capacitances in the circuit, in the order of a few femtofarads. Transistors in modern high-speed circuits are manufactured with very fine (28 nm) technologies so that the junctions have very small surfaces, and the resulting junction capacitances, for direct biased junction, are negligible [16].

2.1.1.3 Ordinary Inductance

Wherever a current flows there is a magnetic field proportional and perpendicular to that current, as stated by Ampère's law. The reluctance of the current, which is proportional to the magnetic field, to build up or decay quickly, in response to injected power, is called 'inductance' [14]. In order to express the last sentence in a mathematical formula, the induced voltage in a loop will be considered. By integrating the electric field along the path of the circuit and using Stokes' theorem,

$$V_L = -\oint_C \vec{E} \cdot d\vec{l} = -\int_S \left(\nabla \times \vec{E}\right) \cdot d\vec{S} \tag{2.15}$$

where V_L is the electric potential difference between the ends of the path C , and S is the surface bounded by this path. The electric field $\vec{E}$ is associated with the current that induces the voltage, and only tangential components to the path C contribute to a rise in the voltage. $\nabla \times \vec{E}$ is perpendicular to the electric field and is related to the magnetic field, as follows from the Maxwell equations:

$$\nabla \times \vec{E} = -\frac{d\vec{B}}{dt} \tag{2.16}$$

Then the voltage is:

$$V_L = \frac{d}{dt} \int_S \vec{B} \cdot d\vec{S} \tag{2.17}$$

The quantity $\int_S \vec{B} \cdot d\vec{S}$ is the magnetic flux through the surface bounded by the path C and is proportional to the current,

$$LI = \int_S \vec{B} \cdot d\vec{S} \tag{2.18}$$

or,

$$L\frac{dI}{dt} = V_L \tag{2.19}$$

In a loop transmission line (Figure 2), e.g. a high-speed differential signal, there is an inherent inductance that can be obtained easily for DC or even slow AC signals, as follows:

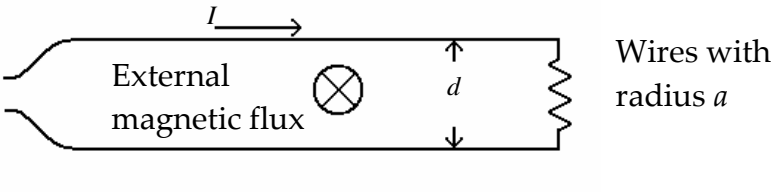

Figure 2. Current and related magnetic flux in a loop transmission line

It can be shown that the total inductance of the transmission line is the result of the addition of the internal inductance, the inductance owing to the magnetic flux inside the wires and the external inductance, as a result of the flux through the surface bounded by the wires [12].

After Niknejad [12], the internal inductance of the wires per unit length is given by:

$$L_{\text{int}} = \frac{\mu_r \mu_0}{8\pi} \tag{2.20}$$

Where μ_r is the relative permeability of the medium and μ_0 is the permeability of vacuum in Henry per meter (H/m). The external inductance of the wires is given by:

$$L_{\text{ext}} = \frac{\mu_r \mu_0}{\pi} \ln\left(\frac{d-a}{a}\right) \tag{2.21}$$

In chapter 4 these quantities will be compared with parameters of a concrete design.

2.1.1.4 Resistance

The Ohm's law can be expressed equivalently as:

$$\vec{J} = \sigma \vec{E} \tag{2.22}$$

where $\vec{J}$ is the current density in a conductor, σ the conductivity of the conductor, and $\vec{E}$ the electric field in the conductor in which this current density is present.

This relationship applies to fields that change very slowly with respect to time. At high frequencies the current, e.g. in a planar conductor, decreases exponentially owing to the skin effect. The effect of the skin effect is that there is not only a resistive impedance, as predicted by Ohm's law, but there is also a reactive impedance [15]. This relationship is shown as follows:

$$Z_S = (1-j) R_{AC} \sqrt{f} \cot\left((1-j) R_{AC} \sqrt{f} \frac{1}{R_{DC}}\right) \tag{2.23}$$

where $R_{DC} = \frac{1}{\sigma d}$, $R_{AC} = \sqrt{\frac{\pi\mu}{\sigma}}$ and f is the frequency of the current.

Most modern circuits work at high frequencies so the impact of the skin effect must be taken into account in the design.

2.1.1.5 Coupled Reactances

As already mentioned, between conductors charged to different potentials there is an electric field and, on the other hand, wherever a current flows a magnetic field is induced. These two phenomena are the causes of most parasitic noise and can be described as parasitic, or mutual, capacitance and inductance, respectively.

The mutual capacitance C_M between two circuits A and B injects a current I_{BM} into circuit B, proportional to the rate of change of the voltage in circuit A, as follows:

$$I_{BM} = C_M \frac{dV_A}{dt} \tag{2.24}$$

This equation applies under some logical assumptions and which can be guaranteed in a low noise design. First, the noise or coupled current I_{BM} is much smaller than the signal current of the circuit A. Second, the coupled voltage V_{BM} is much smaller than the signal voltage of the circuit A. Third, there is no response from the affected circuit B to the aggressor circuit A.

As already shown, the capacitance can be calculated easily if the geometry of the charged conductors, and the distance between them, are known, even though a measurement of this capacitance often results more easily and more realistically than the calculation, since the calculation is based on an exact description of the geometry. An important index to quantify the disturbing influence of one circuit on another is the crosstalk. In terms of voltage it can be described as the ratio between the coupled voltage and the voltage change that caused the parasitic noise[14],

$$Crosstalk_C = \frac{R_B I_{BM}}{\Delta V_A} \tag{2.25}$$

where ΔV_A is the voltage difference or voltage step occurred in a time T_{rA}, the waveform rise time, and R_B is the impedance of the affected circuit. In terms of the rise time and the voltage step, the capacitance can be written as:

$$C_M = \frac{I_{BM}}{\left(\frac{dV_A}{dt}\right)} = \frac{I_{BM}}{\left(\frac{\Delta V_A}{T_{rA}}\right)} \tag{2.26}$$

and the crosstalk, owing to coupled capacitance:

$$Crosstalk_C = \frac{R_B I_{BM}}{\Delta V_A} = \frac{R_B C_M}{T_{rA}} \tag{2.27}$$

Similarly, the mutual inductance L_M injects a noise voltage into a circuit B, V_{BM} depending on the rate of change of the current of the circuit A, I_A.

$$V_{BM} = L_M \frac{dI_A}{dt} \tag{2.28}$$

In high-speed circuits this fact has great importance: if the current in circuit A could change as an ideal step, it would produce a voltage peak of infinite amplitude in circuit B. The faster the signal, the worse this effect.

In the same way as for the equation of mutual capacitance, this equation applies under some assumptions. First, the noise or coupled voltage V_{BM} is much smaller than the signal voltage of circuit A. Second, the coupled current I_{BM} is much smaller than the signal current of circuit A. Third, there is no response from the affected circuit B to the aggressor circuit A.

In order to find a mathematical expression for the inductive crosstalk, the temporal change of the current in the circuit A will be written as:

$$\frac{dI_A}{dt} = \frac{1}{R_A}\frac{dV_A}{dt} = \frac{\Delta V_A}{R_A T_{rA}} \tag{2.29}$$

where R_A is the impedance of the circuit A. Then the induced voltage into circuit B can be written as:

$$V_{BM} = L_M \frac{\Delta V_A}{R_A T_{rA}} \tag{2.30}$$

and the crosstalk is,

$$Crosstalk_L = \frac{V_{BM}}{\Delta V_A} = \frac{L_M}{R_A T_{rA}} \tag{2.31}$$

2.1.1.6 Thermal noise

Thermal noise is present in every conductor and is proportional to the temperature. Some characteristics of the thermal noise are:

- Its average is zero
- Its RMS (Root Mean Square) value is not zero
- Its amplitude is Gaussian distributed

For practical purposes only the thermal noise in a resistor and in a capacitor will be analysed. These are the most important sources of thermal noise in a digital circuit.

The noise power of any impedance Z is given by

$$\overline{v_Z^{\,2}} = 4kTZB \tag{2.32}$$

where v_Z is the voltage over the impedance, k is the Boltzmann constant, T the temperature of observation, Z the value or the impedance and B the bandwidth of observation.
The noise power of a resistor R is:

$$\overline{v_R^{\,2}} = 4kTRB \tag{2.33}$$

A real capacitor can be modelled as an ideal capacitor C, in parallel with a resistor R_C. The impedance of this shunt circuit is:

$$Z = \frac{R_C}{(j\omega CR_C + 1)} \tag{2.34}$$

The noise power over all frequencies for a real capacitor is:

$$\overline{v_R^{\,2}} = 4kT\int_0^\infty \frac{R_C^{\,2}}{\left((\omega CR_C)^2 + 1\right)} df = \frac{kT}{C} \tag{2.35}$$

2.1.2 High Speed Design

The bottleneck in optical communication systems is the electronics. This affirmation suggests that special attention has to be paid to the electronic design, in order to achieve the desired results in the complete system; that is, a high signal to noise ratio.

For the test of the optical systems, electronic systems were designed, taking into account the integration of the couplers and the electronic devices on a PCB. In a first phase, a single channel prototype allowed the proof of principle of the optic communication path. In the second phase, the 12-channel system was tested.

At the beginning of this chapter the block diagram of the communication path was presented. In the Figure 3 the detailed electrical path, as it was implemented in the multi-channel system, is shown.
Here, the construction of the PCB for a single channel is shown from the side view. It corresponds to the implementation of the 12-channel system. The electrical-signal path is shown in detail. Associated with each path and connection is a parasitic that can be modelled as shown in Figure 4 [15].

The electronic devices are modelled as ideal amplifiers connected to discrete devices, which represent the intrinsic parasitics of the semi-conductor parts. The only devices in this scheme that are not parasitics are the AC-coupling capacitor after the FPGA-output, and the AC-coupling capacitor before the FPGA-input.

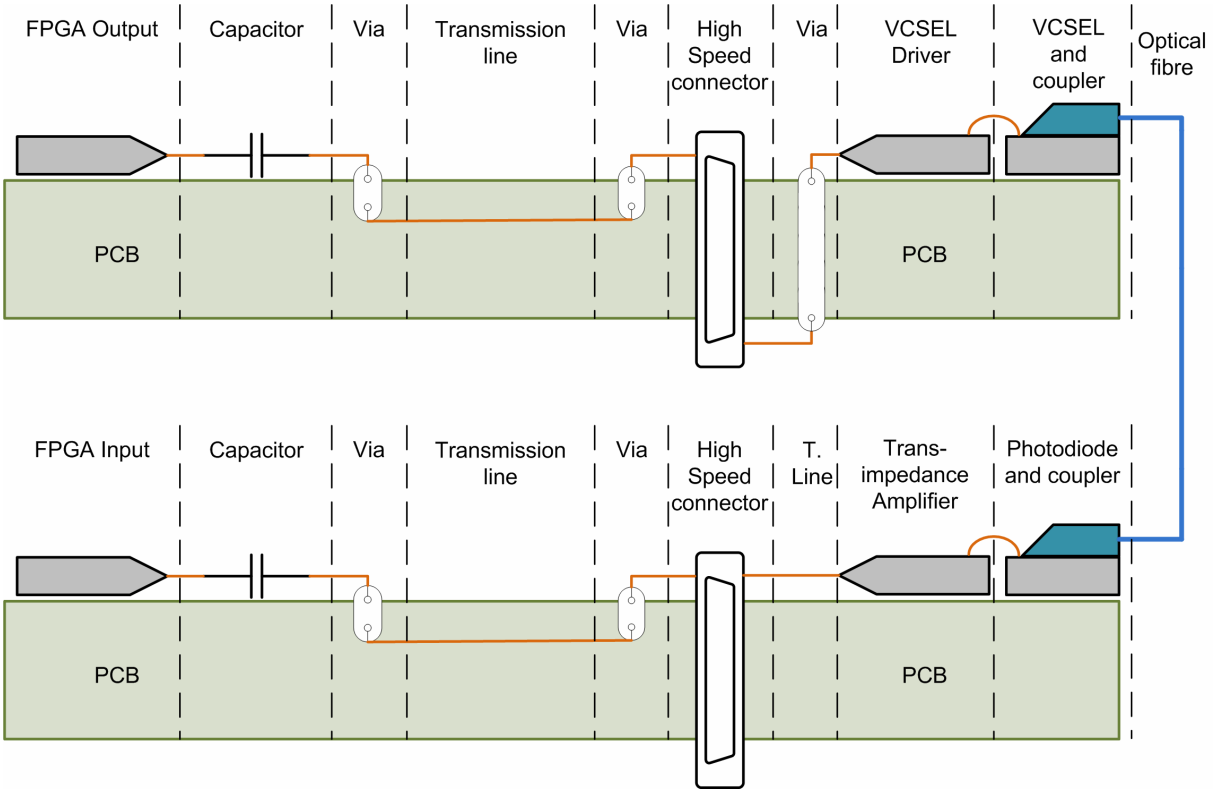

Figure 3. Detailed view of the electrical path

All other devices shown in the model represent the inherent parasitics of the components involved in the electric path. The transformers represent the presence of coupled noise coming from the neighbouring signals.

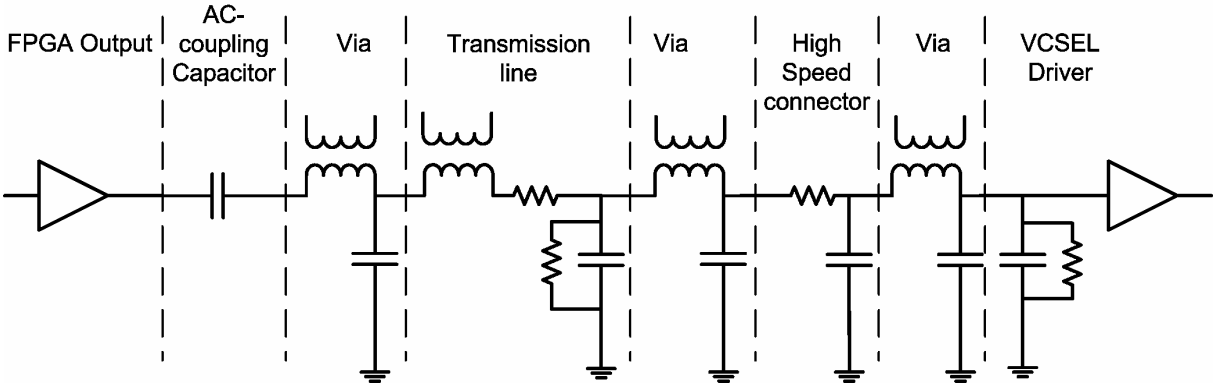

Figure 4. Electrical model of the send path

Figure 5 shows the receive path. It is somewhat simpler than the send path because it contains one less 'via'.

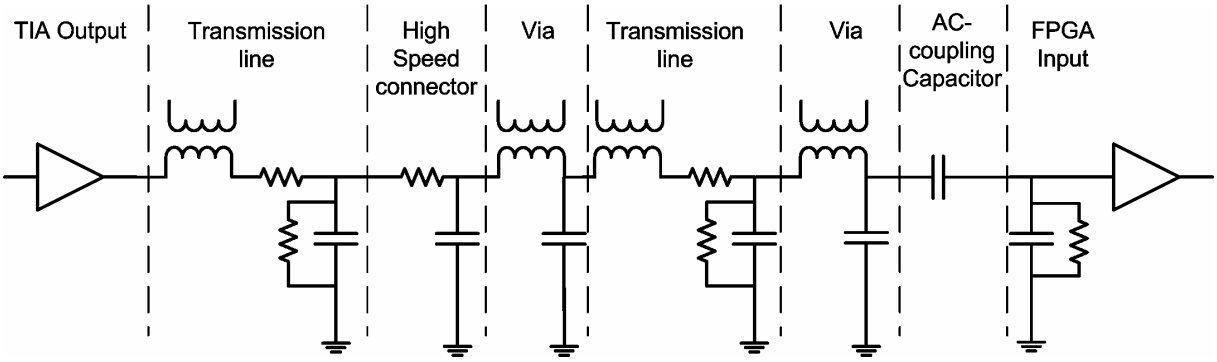

Figure 5. Electrical model of the receive path

The signal is received by the VCSEL-driver and transmitted electrically to the VCSEL over bonded wires. The model [17] of the bond wire is shown in the Figure 6.

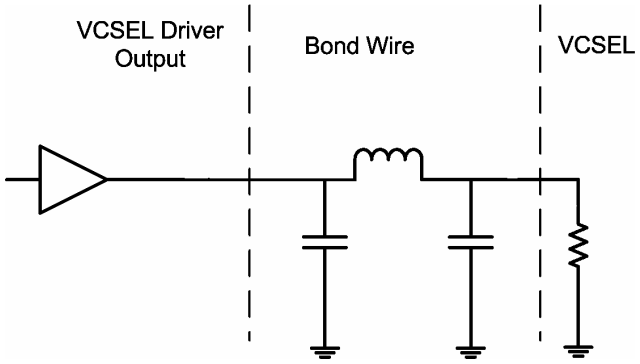

Figure 6. Model of the bond wire

2.1.2.1 Calculation of parasitics in the design, and measures to avoid the parasitics

In order to quantify the bandwidth of the design it is necessary to characterise the electrical paths quantitatively. The scatter parameters description is useful for determining relationships such as voltage gain and reflection coefficients [19]. They do not provide information for an analysis of the critical parasitics in the design. Better than the calculation of the scatter parameters is an analysis of the dominant parasitics, which allows the simplification of the above complex circuits.

2.1.2.1.1. Vias

Starting with the send path, the first parasitic impedance is a result of the via after the AC capacitor. The capacitance of a via is given by:

$$C_V = \frac{\sqrt{2}\varepsilon_r T D_P}{D_H - D_P} \cdot \frac{1}{25.4} \tag{2.36}$$

where ε_r is the relative permittivity of the PCB, T is the thickness of the substrate between the via pads, D_P is the diameter of the metal pad, D_H is the diameter of the clearance pad in the ground plane, and the factor 25.4 sets the calculation in SI units. For the constructed circuit the values are as shown in the Table 1.

Symbol		Units
ε_r	4.5	
T	1.4	mm
D_P	0.45	mm
D_H	0.7	mm
C_V	0.63	pF

Table 1. Parameters for calculation of the via's capacitance

For a via that goes from layer 1 to layer 5 the substrate has a thickness of 0.5 mm. The total thickness of the PCB is 1.6 mm.

This calculation supposes the elimination of pads in non-signal layers. It means that between the pads in layers 1 and 12 there is only substrate material.
The via also has a parasitic inductance that is calculated [14] as:

$$L_V = 0.2 \cdot h \left[\ln\left(\frac{4h}{d}\right) + 1 \right] \tag{2.37}$$

where h is the length of the via and d is the via-hole diameter. Table 2 shows the values for the constructed circuit.

Symbol		Units
h	0.6	mm
d	0.3	mm
L_V	0.33	nH

Table 2. Parameters for calculation of the via's inductance

The via-capacitance is measurable but has an almost negligible effect while the via-inductance affects the bandwidth of the transmission line directly. Another negative aspect of the via is the ability to couple noise since, in the direction perpendicular to the PCB plane, there is no electrical isolation of the signals. In order to minimise the coupled noise in a signal via, ground vias are placed near them. In this way, the radiated noise is coupled into the ground planes. This vias' array is called GSSG for a differential pair, as shown in Figure 7 taken from UG169 Xilinx.

The signal paths are shown in red and orange. The ground vias and planes are shown in blue.

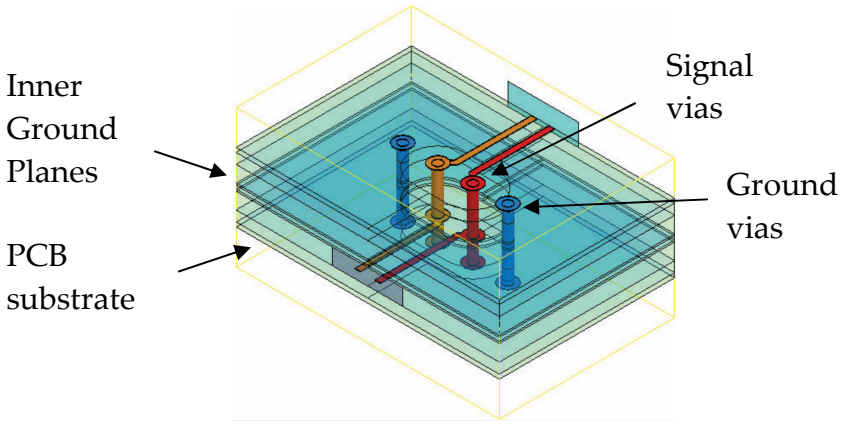

Figure 7. GSSG vias to minimise crosstalk

Using these design techniques the via-capacitance and the via-coupled inductance are reduced drastically, and the model of the via can be simplified to a single inductor of the calculated value.

2.1.2.1.2. Transmission lines

In the Figure 4 and Figure 5 the static model of the transmission line provides information about its frequency dependant impedance. This model can be simplified by replacing the static model by the impedance that the signal really 'sees': the characteristic impedance of the transmission line. The striplines were designed to have a 50Ω characteristic impedance calculated after the model of Kirschning and Jansen [18] with the parameters shown in the Figure 8.

Symbol		Units
W	80	μm
S	127	μm
B	218	μm
T	18	μm
σ	$5.88 \cdot 10^7$	S/m
ε_r	4.5	

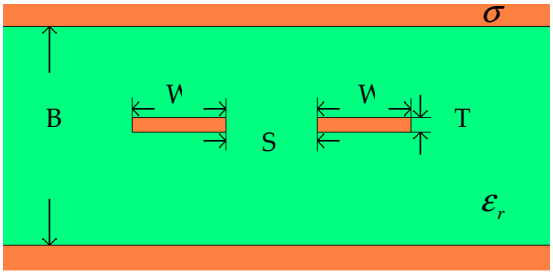

Figure 8. (Left) Parameters for calculation of the characteristic impedance of the striplines. (Right) Cross section of the transmission line.

Novàk [20] showed that the crosstalk amplitude to the signal amplitude ratio in coupled striplines is about one to thousand. The crosstalk becomes important when the amplitude of the signal is comparable to that of the crosstalk-noise. Owing to the construction of the coupled striplines, this happens only when the lines are extremely long; that is, more than 200 mm.

2.1.2.1.3. High speed connector

The connector has also a complex distributed model that is not available for customers. From the datasheet can be deduced that the connector was designed for frequencies higher than 20 GHz; more that the needed bandwidth for the system. The characteristic impedance is also 50Ω for the differential pairs.

2.1.2.1.4. Excess capacitance and on-chip crosstalk

The AC-coupling capacitors can introduce excess capacitance and, if using capacitors-arrays, the crosstalk will definitely afflict the signal quality. In order to avoid cross-talk because of the package density of chip arrayed capacitors, discrete chip capacitors were used in the design.

In the previous section, it was shown that there is always a capacitance between parallel conductive planes. In the case of the AC-coupling capacitors, when the devices are placed, for example, on the top layer over a ground plane, there is an excess capacitance between the signal traces and the ground plane. This capacitance couples the signal path and the corresponding plane electrically. In order to have a controlled characteristic impedance, the dimensions of the signal path are calculated accurately so that any variation of these dimensions varies the characteristic impedance of the path, which results in a degradation of the signal quality.

The transmission lines are placed on the top layer of the PCB as a differential pair. In order to maintain a constant characteristic impedance over the whole path, the distance between microstrips and their thickness is kept constant. For placing of the capacitors, these distances have to be increased, so that the impedance increases slightly. In order to reduce the excess capacitance, owing to the pads of the discrete capacitors, void planes areas were placed under the pads on the plane used to couple the transmission lines, as shown in Figure 9.

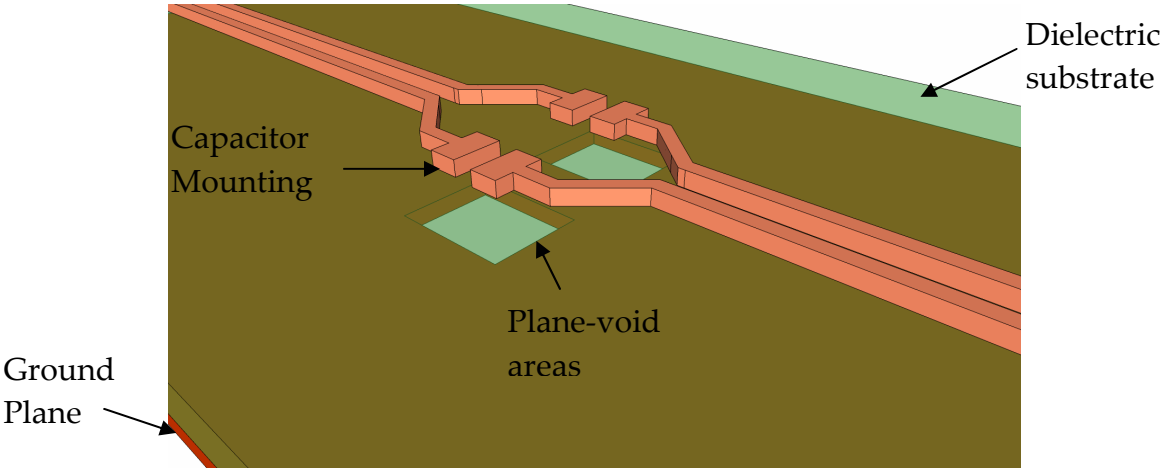

Figure 9. Minimisation of excess capacitance

2.1.2.1.5. Wirebonds

The impedance of the wirebonds is calculated after Gupta et al [21]. The inductance of the wire is given by

$$L_{WB} = 5,08 \cdot 10^{-3} \cdot h \left[\ln\left(\frac{4h}{d}\right) - 1 \right] \tag{2.38}$$

where h is the length and d is the thickness of the wire.

Symbol		Units
H	1	mm
D	0.025	mm
L_V	21	pH

Table 3. Parameters for calculation of the wirebond's inductance

The capacitances are a result of the contact between the wirebonds and the pads, and are typically 0.5 pF [21].

2.1.2.2 Bandwidth of the electrical path

The bandwidth of the electrical path can be now calculated using the simplified model of Figure 10. The inductance of the vias (1.1 nH) is multiplied by three owing to the same amount of vias present on the electrical path.

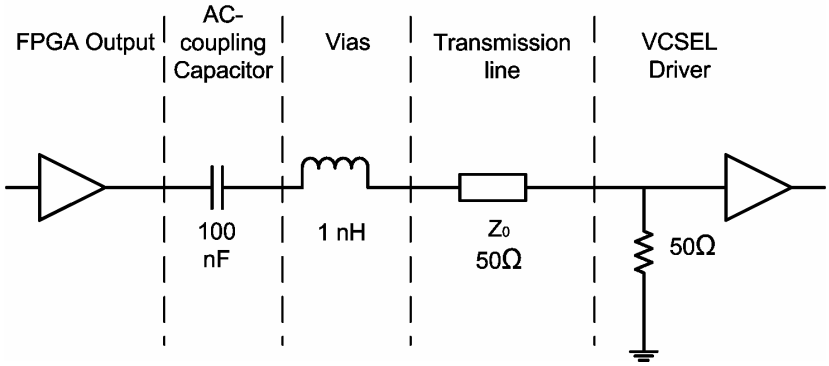

Figure 10. Simplified model of the send path

It can be easily seen that the topology corresponds to a low pass filter which dominating pole is given by the inductivity of the vias. The voltage transfer function is given by:

$$H(j\omega) = \frac{R_{inVD}}{\frac{1}{j\omega C_{AC}} + j\omega L_{VIA} + Z_0 + R_{inVD}} \tag{2.39}$$

where R_{inVD} is the input resistance of the VCSEL Driver, C_{AC} is the AC-coupling capacitance, L_{VIA} is the parasitic impedance of the via, and Z_0 is the characteristic impedance of the strip lines. The AC-coupling capacitor works as a high pass filter, it blocks low frequent signals and can be omitted for the high frequency analysis:

$$H(j\omega) = \frac{R_{inVD}}{j\omega L_{VIA} + Z_0 + R_{inVD}} \tag{2.40}$$

The 3 dB frequency of the low pass filter is:

$$f_{3dB} = \frac{Z_0 + R_{inVD}}{2\pi L_{VIA}} = 15.92 \text{ GHz} \tag{2.41}$$

2.1.2.3 Simulation of the electrical path

For verification of this analysis, the paths shown in Figure 4 and Figure 10 were simulated with RFSim99 and compared. A frequency-sweep from 100 kHz to 100 GHz shows the results shown in Figure 11 and Figure 12.

At low frequencies, the frequency dependant impedances do not have any effect so that the Power transferred to the load is a half (~-3dB) of the input Power.

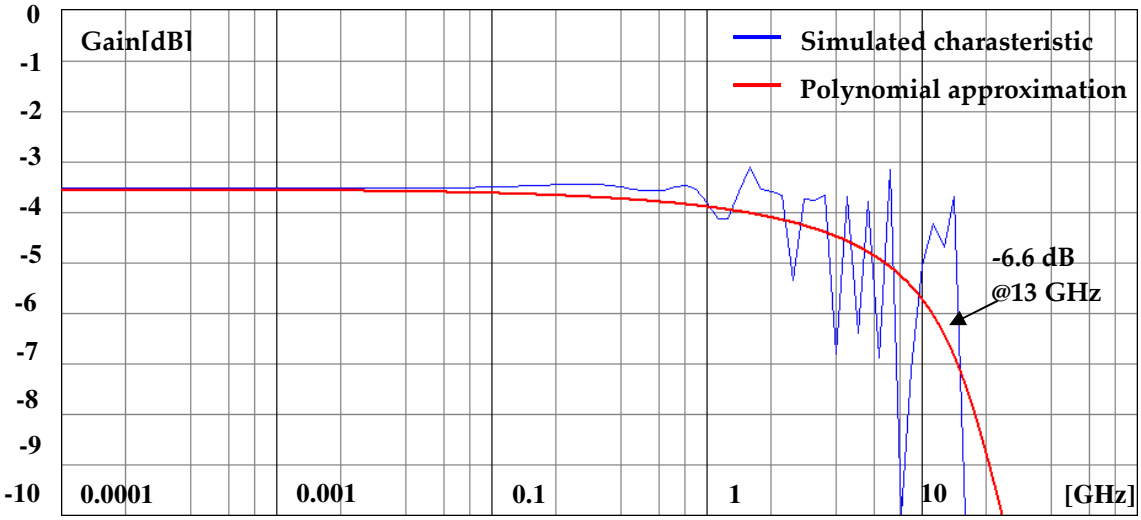

Figure 11. Frequency response corresponding to the electrical path of Figure 4

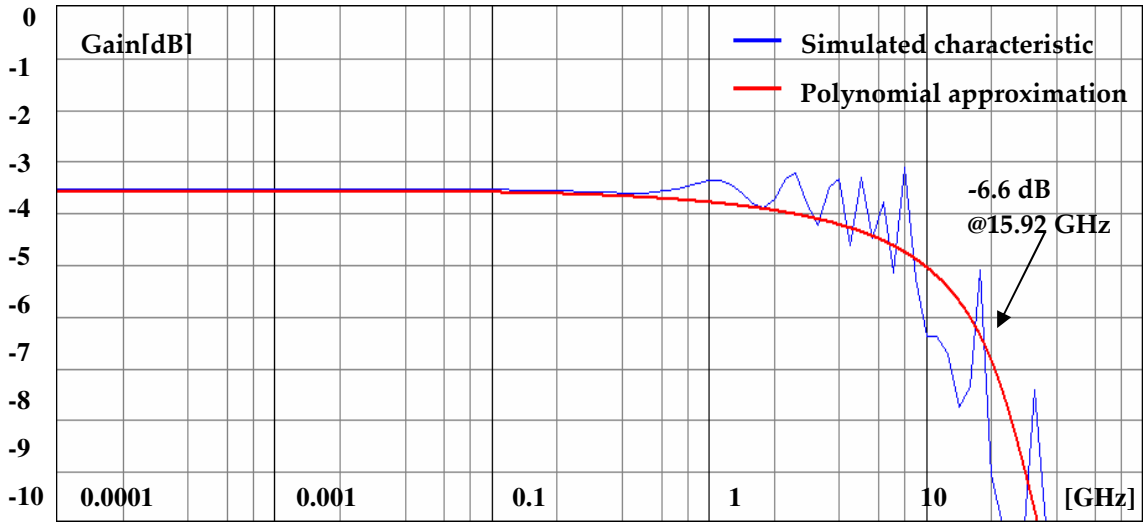

Figure 12. Frequency response corresponding to the simplified electrical path of Figure 10

The analysis of the electrical path simplifying the circuit is accurate and gives useful information about the critical parasitics.

The wirebond was also simulated and the results of a frequency-sweep from 1 MHz to 25 GHz are shown in the Figure 13.

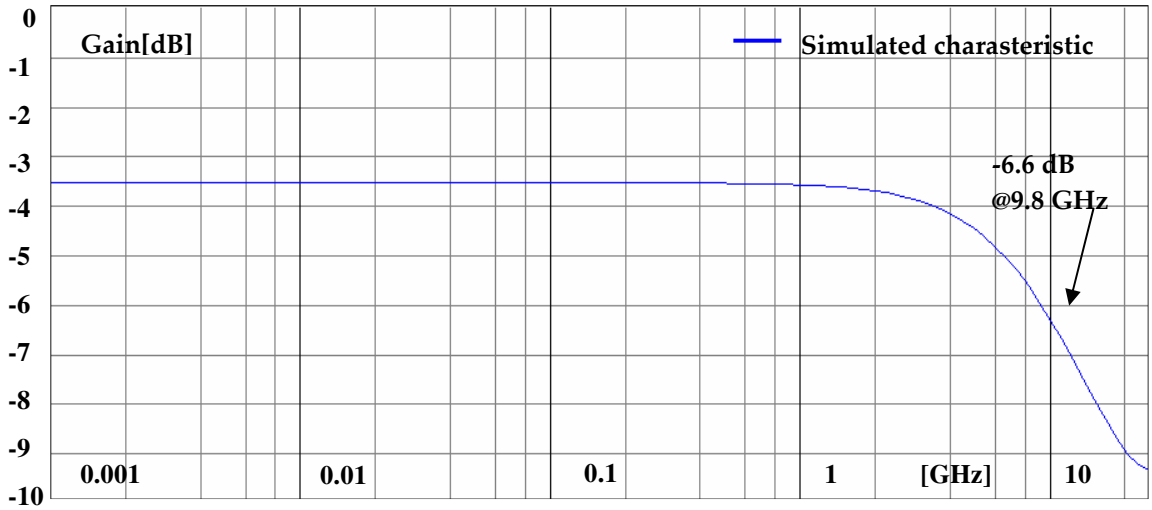

Figure 13. Frequency response corresponding to the electrical path of Figure 6

2.2. Optical Interconnects

The first optical communication system dates back to the 1790s, when the French inventor Claude Chappe invented the semaphore telegraph. Almost 100 years later, Alexander Graham Bell patented the Photophone; an optical telephone system. At that time, the implementation of the Photophone was not as practical as that of the telephone, so the Photophone remained an experimental invention. The first attempt

to transfer information over an optical medium was done in the 1920s, by John Logie Baird, in England, and Clarence W. Hansell, in the United States. They used arrays of hollow pipes or transparent rods to transmit images for television, or facsimile systems.

Thirty years later in 1954, Dutch scientist Abraham Van Heel reported on simple bundles of clad fibres. He covered a bare fibre with a transparent cladding of a lower refractive index. This protected the fibre's reflection surface from outside distortion and reduced interference between fibres, thus making the crucial innovation of cladding fibre-optic cables. By that time, glass fibres with plastic cladding had attenuation of about 1 decibel (dB) per metre; still too high for a communication system.

By 1964, a theoretical specification was identified by Charles K. Kao for long-range communication devices: the 10 or 20 dB of light loss per kilometre standard. Kao also illustrated the need for a purer form of glass to help reduce light loss.

In the early 1970s, R. Maurer, D. Keck, and P. Schultz developed 'optical waveguide fibres', and developed a single mode fibre with low losses: 17 dB/km at 633 nm by doping the fibre core with titanium. After that, the same group developed the multimode germanium-doped fibre, which had a loss of 4 dB per kilometre, and was more stable with respect to mechanical stress than titanium-doped fibre. In 1973, John MacChesney at Bell Labs modified the chemical vapour-deposition process for fibre manufacture. This process spearheaded the commercial manufacture of fibre-optic cables [22].

In April 1977, the world's first live telephone traffic through a fibre-optic system was tested by General Telephone and Electronics in Long Beach, California. It reached a transfer rate of 6 Mbps. Just a month later, Bell installed an optical telephone communication system in downtown Chicago. The optical-fibre-based communication over a distance of 2.4 km carried the equivalent of 672 voice channels per pair of optical channels. Today more than 80 per cent of the world's long-distance voice and data traffic is carried over optical-fibre cables.

In the late 1970s, just as optical communication systems seemed to work commercially for first time, Kenichi Iga of Tokyo Institute of Technology invented the vertical cavity surface emitting laser (VCSEL)[23]. Low power consumption, wafer level testing, low profile layout and availability in small pitch arrays are some of the advantages that aided the development of optical communication systems and made them cost-effective. One of the most challenging problems in optical communication systems is the coupling of light into the fibre. The small sizes and the low tolerances set high requirements for the design and fabrication of Micro-Opto-Electro-Mechanical Systems (MOEMS).

2.2.1 Components of an Optical Communication System

Apart from the optical fibre, modern optical communications use high-speed sources and detectors. The sources used for short range interconnects are usually Light Emitting Diodes (LEDs) and semi-conductor lasers. For the detection of the signal pin

diodes, avalanche photodetectors, metal-semi-conductor-metal photodetectors and travelling wave detectors are used. In the first part of this section, these optoelectronic devices are briefly explained, and the optical characteristics of devices used in the design are presented in the second part.

2.2.1.1 Light-Emitting Diode (LED)

Semi-conductor light sources require the creation of hole-electron pairs via 'electrical pumping'. The p-n junction is biased positively and minority carriers are injected into both sides of the junction. The holes pass to the electrons-excess side and the electrons pass to the holes-excess side. The 'free' hole-electron pair has gained energy and is at the conduction energy level. The hole-electron pair can recombine radiatively, emitting photons with an energy of $h \cdot \nu$, approximately equal to the bandgap energy. The recombination is spontaneous. That implies that the emission has a random phase and is incoherent.

The most important parameter of an LED, relative to its bandwidth, is the lifetime of the recombining carriers, and is defined as follows [24]:

$$\frac{1}{\tau_{total}} = \frac{1}{\tau_{rr}} + \frac{1}{\tau_{nr}} \tag{2.42}$$

where τ_{rr} is the lifetime of the radiative recombining carriers, and τ_{nr} is the lifetime of the non-radiative recombining carriers. It depends on the material and doping characteristics, as well as on the geometry of the diode.

For example, typical lifetimes for GaAs and InGaAsP diodes vary from 2ns to 10 ns [25].

The bandwidth of the LED is defined as:

$$f_{3dB} = \sqrt{3}\frac{1}{2\pi\tau_{total}} \tag{2.43}$$

For the considered examples, the bandwidth will be between 28 and 138 MHz.

Concerning the emitting efficiency of a LED, the emitted optical power is given by:

$$P_{opt} = \eta_{int}\eta_{ext} \cdot h\nu \frac{I}{q} \tag{2.44}$$

where $\frac{I}{q}$ is the number of electrons or holes that are injected into the junction in a second, η_{int} is the internal quantum efficiency and represents the fraction of hole-electron pairs that recombine radiatively, η_{ext} is the external quantum efficiency and represents the fraction of generated photons that escape from the active layer.

The internal quantum efficiency η_{int} is the ratio of the recombination rate of radiative combining carriers to the sum of radiative recombination rate and non-radiative recombination rate:

$$\eta_{int} = \frac{R_{rr}}{R_{rr} + R_{nr}} \tag{2.45}$$

These parameters are extracted from the description of the recombination mechanism with Boltzmann statistics [26].

The external quantum efficiency η_{ext} depends on optical properties of the device.

The transmissivity is for s-polarisation given by [27]:

$$\mathrm{T}(\vartheta_e) = \frac{4 n_e n_t \cos(\vartheta_e)\cos(\vartheta_t)}{\left(n_e \cos(\vartheta_e) + n_t \cos(\vartheta_t)\right)^2} \tag{2.46}$$

where n_e is the refractive index of the incidence medium; for example, Galium-Arsenide, n_t is the refractive index of the medium to which light is transmitted, ϑ_e is the incidence angle, and ϑ_t is the angle of the beam in the transmitted medium. They are related to each other by Snell's law:

$$n_e \cos(\vartheta_e) = n_t \sin(\vartheta_t) \tag{2.47}$$

For the calculation of the external quantum efficiency only the beams capable of transmission are regarded:

$$\eta_{ext} = \frac{1}{4\pi} \int_0^{\vartheta_c} 2\pi T(\vartheta_e) \sin(\vartheta_e)\, d\vartheta_e \tag{2.48}$$

where ϑ_c is the critical angle of total internal reflection.

For perpendicular incidence this expression is

$$\eta_{ext} = \frac{1}{n_e (n_e + n_t)^2} \tag{2.49}$$

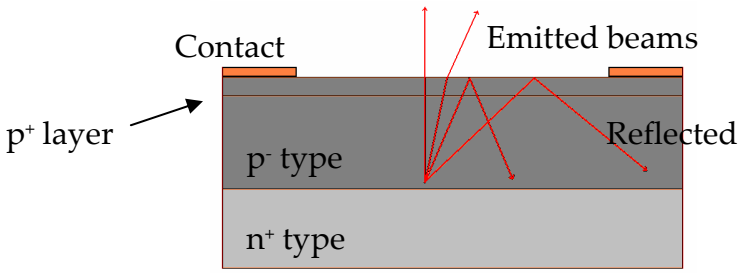

Figure 14. Sketch of the p-n junction and emitted light in a LED

For GaAs this value is about 1.5%, which suggests that most of the light generated is trapped inside the device. For this reason, in modern devices, LED-packages are designed to maximise the optical efficiency [52] i.e. by placing lenses with different shapes depending on the application [53].

2.2.1.2 Semiconductor Lasers

Other than LEDs, lasers operate on the basis of stimulated emission-generated light. Light oscillates in a gain medium between reflective surfaces. When the gain medium becomes saturated the laser reaches its steady state.

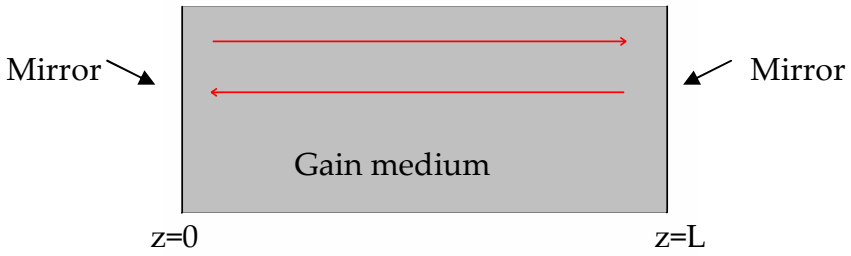

Figure 15. Schematic diagram of the resonator in a laser diode

The electric field in the gain medium oscillates between the reflective surfaces, and suffers attenuation because of the interaction with the gain medium and reflection at each mirror, which are not ideal. The electric field is given by:

$$E(z) = E_0 e^{-jk_z z} e^{\left(g/2 - \alpha_{\text{int}}/2\right)z} |r_1||r_2| \tag{2.50}$$

E_0 is the electric field at the starting point, r_1 and r_2 are the amplitude-reflection coefficients of the mirrors, $g/2$ is the gain of the medium and $\alpha_{\text{int}}/2$ is the internal loss of the medium. In order to maintain the amplitude of the starting electric field, the gain has to equal the losses after the wave has travelled the distance L through the medium, was reflected by the second mirror and went back to the start point:

$$g = \alpha_{\text{int}} + \frac{1}{L}\ln\left(\frac{1}{|r_1||r_2|}\right) = \alpha_{\text{int}} + \alpha_{mir} \tag{2.51}$$

where α_{mir} is the mirror loss term.

For perpendicular incidence in a GaAs (n_e=3.45)-air (n_t=1) boundary the reflection coefficient is [27]:

$$r_{1,2} = \frac{n_e - n_t}{n_e + n_t} = 0,551 \tag{2.52}$$

The phase requirement is given by:

$$2k_0 nL = 2m\pi \tag{2.53}$$

In order to describe the efficiency and the bandwidth of a laser diode, the rate equations will be explained.

The behaviour of the laser diode can be described by two equations

$$\frac{dN}{dt} = \eta_{inj}\frac{1}{qV} - R_{sp} - R_{nr} - g\upsilon_g N_p \tag{2.54}$$

Equation 3.49 is related to the carriers.

$$\frac{dN_p}{dt} = \Gamma g\upsilon_g N_p + \Gamma\beta_{sp}R_{sp} - \frac{N_p}{\tau_p} \tag{2.55}$$

Equation 3.50 relates the photons.

The injection efficiency η_{inj} is the fraction of the terminal current that provides carriers that recombine in the active region; q is the electronic charge; V is the active region volume; R_{sp} is the spontaneous recombination rate R_{nr} is the non-radiative recombination rate; $g\upsilon_g N_p$ is the generation rate of photons, in which g is the incremental optical gain in the active material; υ_g is the group velocity in axial direction of the mode in question; Γ is the three-dimensional mode confinement factor; and τ_p is the photon lifetime in the cavity [28].

The frequency response of the laser diode is determined by the relaxation frequency [25]

$$\Omega_r = \left(\frac{1+\Gamma\upsilon_g aN_0\tau_p}{\tau_p\tau_e}\left(\frac{I}{I_{th}}-1\right)\right)^{1/2} \tag{2.56}$$

where N_0 is the transparency carrier density, a measure of the net number of carriers that emit light. τ_e is the lifetime of the carrier that recombines. I is the modulation current, and I_{th} is the threshold current needed to stimulate the emission.

The bandwidth of the laser is given by:

$$f_{3dB} = \sqrt{3}\frac{\Omega_r}{2\pi} \tag{2.57}$$

2.2.1.3 Photodiodes

The reverse process of emitting light from the change of energy bands by hole-electron pairs is that of generating hole-electron pairs by the absorbed photons in a reverse biased junction. The energy needed by an electron in the valence band to change to the conducting band is approximately $h\nu$.

The created hole-electron pair diffuses across the depletion region to reach the corresponding majority region: n for the electrons and p for the holes. The diffusion process is slow. Therefore, an alternative to the p-n structure is used; the pin structure. An additional i layer expands the depletion region and consequently the absorbing region, as shown in Figure 16.

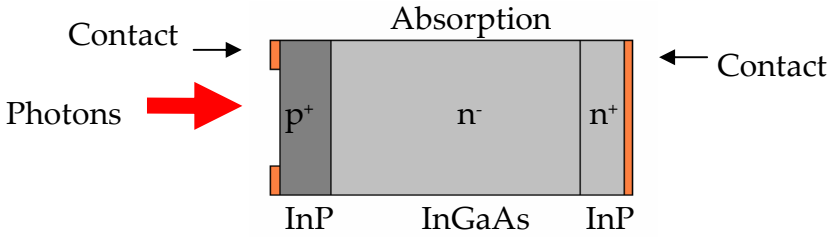

Figure 16. Schematic diagram of the pin diode

The quantum efficiency of a pin diode is given by [25]:

$$\eta_{ext} = \frac{J_{tot}/q}{P_{opt}/h\nu} = \left(1-|r|^2\right)\left(1-\frac{e^{-\alpha w}}{1+\alpha L_p}\right) \tag{2.58}$$

where J_{tot} is the total current density in the device, P_{opt} is the optical power irradiated on the absorbing region, r is the reflectivity of the absorbing surface, α is a normalisation term, w is the length of the i-region; and L_p is defined as follows:

$$L_p = \sqrt{D_p \tau_p} \tag{2.59}$$

where D_p is the diffusion coefficient for holes and τ_p the lifetime of a hole.

The frequency response of a laser depends on the geometry of the i-region and the carrier velocity inside this region:

$$f_{3dB} = \frac{2.4}{2\pi t_{tr}} = \frac{0.38 v_s}{w} \tag{2.60}$$

where $t_{tr} = \frac{w}{v_s}$ is the transit time, or the transit that a carrier needs to diffuse through the depletion or i-region.

The pin diode has no gain. The hole-electron pair recombines depending only on the absorbed photons. A mechanism to increase the gain of a pin diode is the increment of the reverse bias, so that the carriers are accelerated to a higher velocity, becoming able to create new carriers after the collision with hole-electron pairs, in a region with different carrier density. This device is called the 'avalanche diode' after its operating principle. It is made by adding another i-region of another material, as shown in Figure 17.

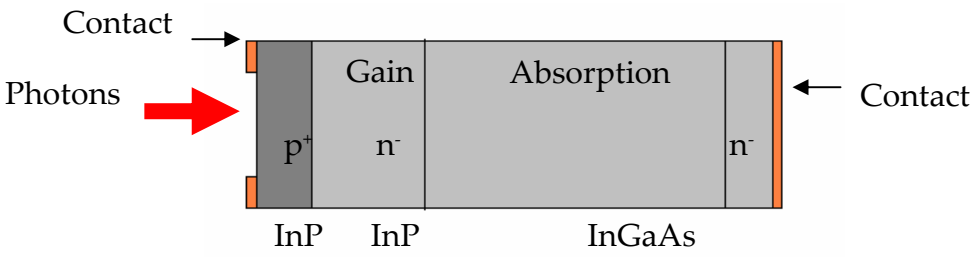

Figure 17. Schematic diagram of the avalanche diode

2.2.1.4 Other photodetectors

It was already shown that the key parameter for the frequency response of a photodiode is the transit time, and depends on the distance the carrier has to travel in the depletion region, and on the reverse bias voltage used to accelerate the carriers.

The Metal-Semi-conductor-Metal (MSM) detector is a pin diode that uses metal contact Schottky barrier diodes and a thin undoped semi-conductor between the metal contacts. The construction is a finger structure, as shown in Figure 18.

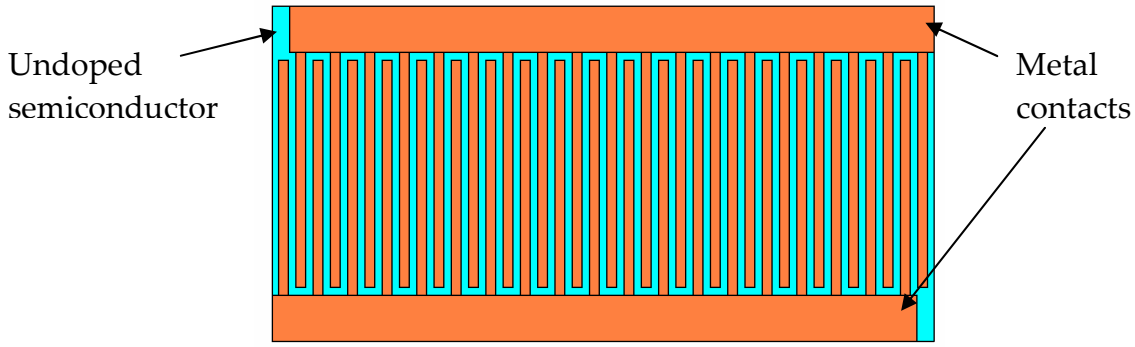

Figure 18. Schematic diagram of the MSM photodiode

The gap between the fingers is minimised. Therefore the transit time is somewhat shorter than in a pin photodiode. The junction capacitance, and the capacitance between the electrodes and the reference ground, may be minimised by the metallic contact. This type of detector can reach easily bandwidths of tens of Gigahertz.

Other advances have been made in order to increase the bandwidth of the photodetectors and overcome the transit time limitation. The waveguide photodetector (WPD) [29][30] is an optical waveguide, with a thin absorption layer that absorbs only a small fraction of the light per unit length. The electrodes on top of the guide and at the sides form a coplanar transmission line, in which the detected signal travels in the form of a current. The schematic of the WDP is shown in Figure 19.

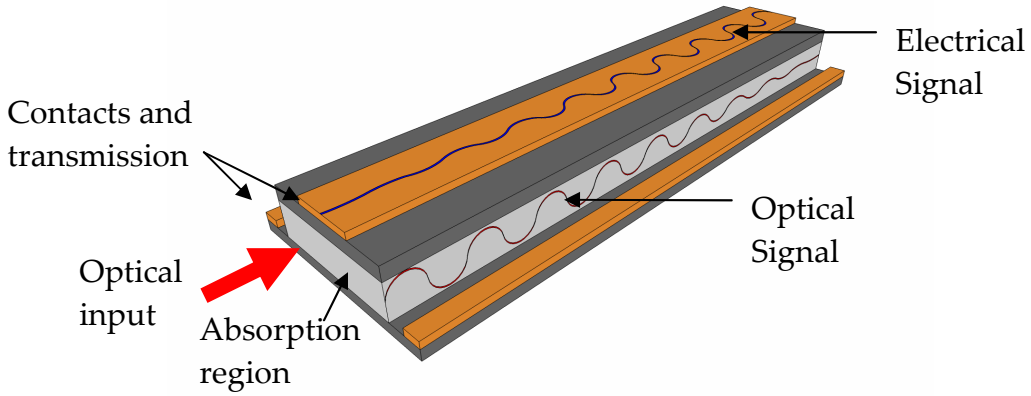

Figure 19. Schematic diagram of the WPD

2.2.1.5 Fibre optics

The simplest fibre is a cylindrical dielectric comprising a core covered by a concentric cladding. This structure is covered by a plastic coating for protection against mechanical stress (see Figure 20) [31].

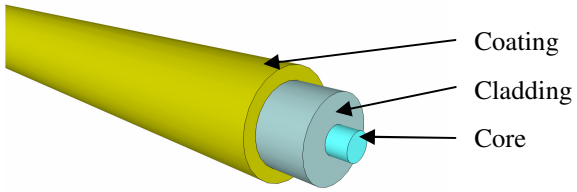

Figure 20. Cylindrical optical fibre

The refractive indexes of the core and the cladding are n_1 and n_2, respectively, with $n_1 > n_2$. This is called the step-index profile.

The behaviour of light in the optical fibre can be described by tracing the rays inside the waveguide and applying the boundary conditions (see Figure 21).

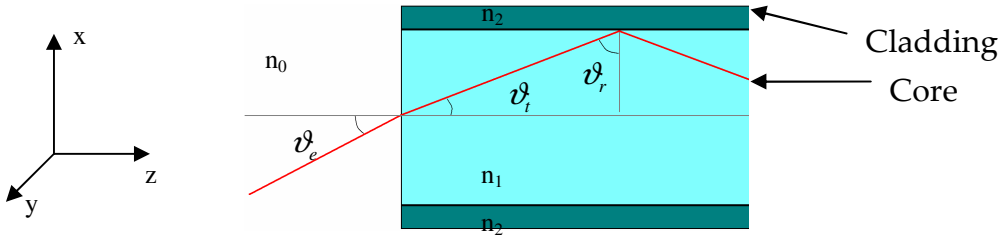

Figure 21. Cylindrical optical fibre (section along the fibre axis)

A light ray travelling within the core meets the core-cladding boundary at an angle ϑ_r and is reflected if this angle is above ϑ_{c12}; the critical angle for total reflection in the boundary between n_1 and n_2 (Figure 21).

This angle is after Snell's law:

$$\vartheta_{c12} = \arcsin\left(\frac{n_2}{n_1}\sin\left(\pi/2\right)\right) = \arcsin\left(\frac{n_2}{n_1}\right) \tag{2.61}$$

In order to find a quantity that characterises the complete construction, the maximal incidence angle at the boundary between n_0 and n_1 is written in terms of ϑ_{c12}.

$$\vartheta_{01\max} = \arcsin\left(\frac{n_1}{n_0}\sin\left(\vartheta_{t\max}\right)\right) \tag{2.62}$$

ϑ_{c12} and $\vartheta_{t\max}$ are related as follows:

$$\vartheta_{t\max} = \pi/2 - \vartheta_{c12} \tag{2.63}$$

Then the equation (2.57) can be rewritten as:

$$n_0 \sin\left(\vartheta_{01\max}\right) = n_1 \cos\left(\vartheta_{c12}\right) = n_1\sqrt{1-\left(\sin\left(\vartheta_{c12}\right)\right)^2} = n_1\sqrt{1-\left(\frac{n_2}{n_1}\right)^2} = \sqrt{n_1^{\,2} - n_2^{\,2}} \tag{2.64}$$

The quantity $n_0 \sin\left(\vartheta_{01\max}\right) = \sqrt{n_1^{\,2} - n_2^{\,2}}$ is called the numerical aperture for a fibre immersed in a medium with refractive index n_0.

$$NA = n_0 \sin\left(\vartheta_{01\max}\right) = \sqrt{n_1^{\,2} - n_2^{\,2}} \tag{2.65}$$

The ray tracing description sets only one condition for the propagation of light in the fibre, but this assertion is not accurate. For the plane wave description, consider a waveguide with a cross-section, as shown in Figure 21, expanded infinitely in the y-z plane. The propagation of the wave depends on the wave phase as follows:

$$2akn_1 \cos\vartheta_r + \delta = m\pi \ \ (m = 0,\ 1,\ 2,\ 3\ldots) \tag{2.66}$$

where a is the thickness of the optical waveguide, δ is the phase change at the reflection, $n_1 k \cos\vartheta_r = \beta$ is the perpendicular component of the wave vector, where $k = 2\pi/\lambda_0$ is the wavenumber and λ_0 is the wavelength of the propagating light in vacuum.

Thus there is only a discrete and finite number of modes for the propagation of the wave under the given conditions.

β is called the propagation constant. Using the equation (2.59), the limits for β are:

$$kn_2 < \beta < kn_1 \tag{2.67}$$

For a cylindrical wave guide, the light within the fibre must be described by a wave solution of the Maxwell's equations. The solution is complicated but can be

simplified using the `weakly guiding approximation´, in which the refractive index of the core is only slightly higher than that of the cladding.

The solutions are, therefore, for the electric field:

$$E_x \propto J_v(\kappa r)\cos(v\phi) \text{ in core} \tag{2.68}$$

$$E_x \propto H_v(i\gamma r)\cos(v\phi) \text{ in cladding} \tag{2.69}$$

where $J_v(\kappa r)$ is the Bessel function, $H_v(i\gamma r)$ is the Hankel function, κ and γ are related to the wave number, and ϕ is the azimuthal angle of the cylindrical coordinate system. Under the `weakly guiding approximation´ the fields are dominated by their transverse components with orthogonal polarisations. These are called linear polarised ($LP_{v\mu}$) modes, where v describes the ϕ dependence and μ is the number of radial maxima of the Bessel function. Some LP modes in the core, also called 'guided modes', are shown in Figure 22 [32].

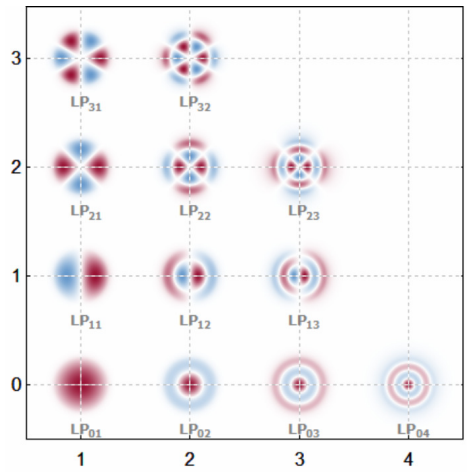

Figure 22. LP modes in an optical fibre with circular cross section

A helpful parameter for describing the number of guided modes in a fibre is the number of the fibre $N = 1/2V^2$ where V is given by

$$V = \frac{2\pi}{\lambda} a\sqrt{n_1^2 - n_2^2} \tag{2.70}$$

where a is the radius of the fibre's core. An obvious problem with this type of waveguide is that the optical path lengths, corresponding to different modes, are different. This limitation is overcome by the graded-index fibre. In such a waveguide, the refractive index changes softly with the radius, as shown in Figure 23. As a result, the different guided modes travel the same optical path lengths, avoiding distortion of the signal owing to the propagation of the light beam in the optical fibre.

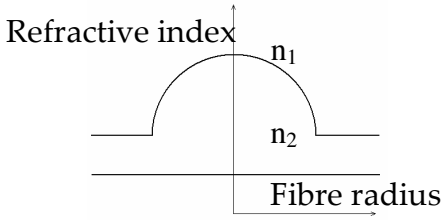

Figure 23. Graded index profile

2.2.1.6 Coupling methods

2.2.1.6.1. Butt coupling

Intuitively, the easiest method to couple the outcoming beam from a laser into an optical fibre is to adjust the fibre end in front of the emitting surface of the laser. This method is called 'butt coupling' and is shown in the Figure 24.

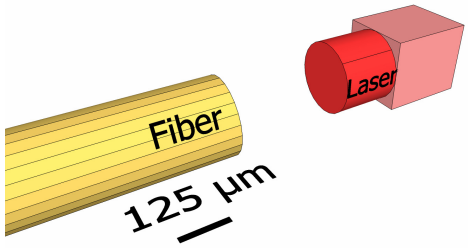

Figure 24. Schematic of the components to adjust in a butt coupling

The handling of the devices requires very precise mechanical systems. Moreover, the problem becomes much more complex if focusing elements are introduced, or if the devices are arrayed. Many degrees of freedom have to be taken under control while the adjustment tolerances are very small.

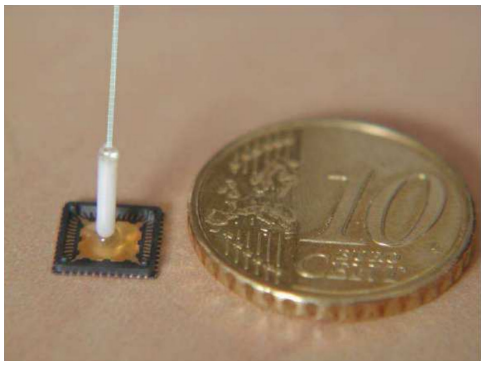

Figure 25. Butt coupling on a GE-on-Si Photodiode [33]

There are several fibre-to-fibre and laser-to-fibre coupling mechanisms. Plastic ferrules are often used to centre the optical fibres in metallic sleeves, where other

fibres or optoelectronic devices are embedded. This works well for single fibres, but for arrayed components, V-Grooves are better than the plastic ferrules.

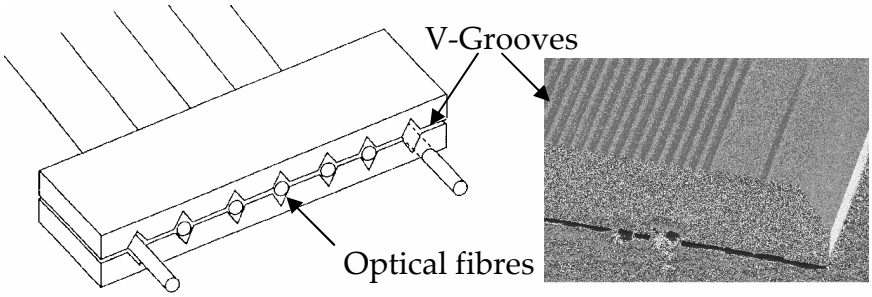

Figure 26. Butt coupling using V-Grooves (SEM Picture from Nanostructures Co.)

With this method, very accurate distances between the fibres can be defined, and a very efficient coupling can be achieved if the end surface of the fibres is parallel to the emitting surface of the laser diodes.

2.2.1.6.2. Tilt coupling

Often the end surface of the fibre and the emitting surface, for a VCSEL, or the sensitive surface, for a Photodiode, are at an angle different from 0° to each other. In this case an additional device is needed for redirecting the beam so that it is coupled efficiently.

The most common configuration is that in which the angle between the devices is 90°. There are different approximations. Some applications use diamond-cutting machines to cut the end of the optical fibre at a 45° angle, and take advantage of the total reflection in the core to redirect the beam by 90°.

The most common approximation is the fabrication of mirrors with plastic polymers.

As already shown, the total reflection condition depends strongly on the media surrounding the boundary. These media are, in practice, plastic polymers and glasses, whose refractive index difference is not very high so that steep angles are needed to achieve reflection. In order to increase the reflectivity, the mirrors are metallic coated. One of these implementations is shown in Figure 27. There, not only the mirror is made from the polymer, but also the waveguides.

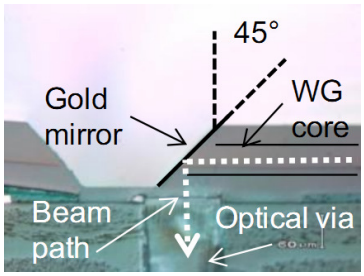

Figure 27. Tilt coupling [34]

2.2.2 Designed optical path and its components, rough description

The light source used in the designed system is a VCSEL. Its mechanical properties allow a flat construction if the outgoing beam, perpendicular to the mount surface, is redirected by 90°. The optical coupler was designed to achieve this function, and then to couple the beam into the optical fibre. The optical signal is transmitted through the fibre and, at its end, the light needs to be coupled into the photodiode. The optical coupler achieves this function again. The coupling concept and its components are shown schematically in Figure 28.

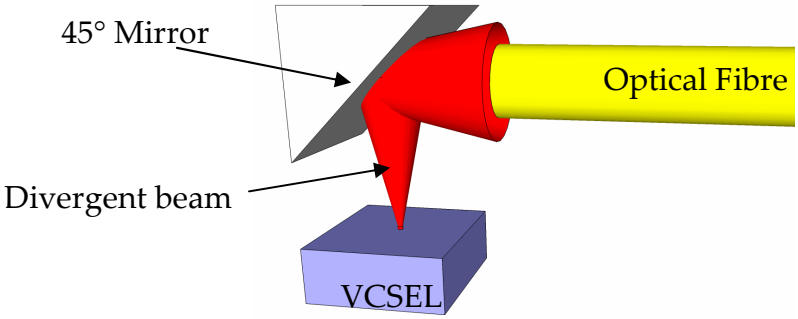

Figure 28. Schematic diagram of the coupling concept at the send side

2.2.2.1 Description of the optical path

The optical path is shown in schematic form in the Figure 29, where an optional component was added. In order to increase the coupling efficiency a Gradient Index Rod Lens can be used to collect the divergent beams coming out from the VCSEL or from the optical fibre.

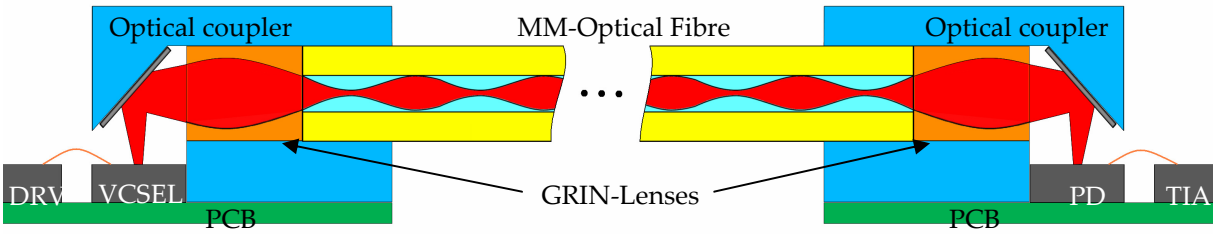

Figure 29. Schematic diagram of the optical path

The optical coupler integrates several optomechanic elements, such as micromirrors, mechanical stops and fibre guides.

2.2.2.2 Optical characteristics of the used VCSEL, the PIN-Photodiode and the Multimode Optical Fibre

The VCSEL used emits a beam whose central wavelength is 850 nm. Its full angle divergence is typically 25°, measured at $1/e^2$ of the maximum irradiance and the typical optical power is 1.2 mW. The efficiency is typically 0.4 W/A, and the specified bandwidth is 7.5 GHz.

The Photodiode used has a spectral response whose maximum is at 850 nm. The optical aperture diameter is 60 μm. The efficiency is typically 0.5 A/W, and the bandwidth is 10 Gbit/s.

The optical fibre has a numerical aperture of 0.22, a core diameter of 50 μm and an attenuation of 2 dB/km.

The optical coupler is explained in detail in the chapter 4.

2.3. Conclusions

- The electrical parasitics present in the high speed PCB design are listed and analysed. The values of the parasitics are calculated regarding the properties of the constructed circuit.
- The frequency response of the electrical transmission line in the PCB was simulated and simplified in order to determine which one of the parasitics contribute with the dominant poles in the bode diagram.
- The dominant parasitic in the design is the vias inherent inductance and it is due to the cylindrical construction of this device.
- In order to minimise the effects of coupled inductance and cross talk due to vias, the GSSG vias configuration is an effective mechanism to couple high speed magnetic fields into the ground planes, and in that way avoid cross talk.
- The optical components that can be used in a short range optical interconnect are listed and briefly described.
- The designed optical system was schematically described in order to identify which of the listed components were used. The characteristics of the components used in the constructed system are listed.
- Because of its small dimensions VCSELs are very attractive for high integrated communication systems. Therefore, the electrical connections represent the most critical factor to take into account in the design: the frequency response of the VCSEL is limited by i.e. the wire bonds.

3. Developed Coupling Concept

The design and fabrication of optical systems are two processes that are linked strongly with each other. For instance, in the design of coupling systems for optical interconnects, the fabrication methods for the coupler and mounting methods for electronic devices on the PCB have to be taken into account, since they affect the efficiency of the coupling directly.

The presented coupling concept integrates several optical subsystems in a monolithic assembly. It reduces the adjustment to only one step: the alignment between the optical coupler and the arrayed microelectronics. In this concept, the optical coupler is manufactured by plastic replication of a metal mould, with the negative shape of the coupler. For replication of the metal master, an ultraviolet curable polymer is used, so that the plastic replicas differ from the metal mould by only a few nanometres.

3.1. Design of the optical coupler

The challenges for the design of the optical coupler are:

- simple coupling structure in order to minimize adjustment complexity
- miniaturized connector, in order to allow multi-gigabit data rates by featuring multi-channel ability
- Integration of several MOEMS in a monolithic structure
- Cost-effective fabrication process
- Light-efficient coupling concept

In the simplest case, the optical coupler only consists of a deflecting mirror. In the proposed concept, the beam emitted from the laser diode (VCSEL) is coupled directly into the optical fibre by using a 45° mirror, placed about 150 μm from the VCSEL. The use of VCSELs has some advantages over edge-emitter lasers. Compared to edge emitters, VCSELs have a lower angle of divergence, lower power consumption and, the most important advantage of this coupling concept: that is, owing to the vertical emission they have a small profile layout, and are therefore integrated easily with micro-optics for high bandwidth communication systems.

In the Figure 30 the integrated micro devices are shown.

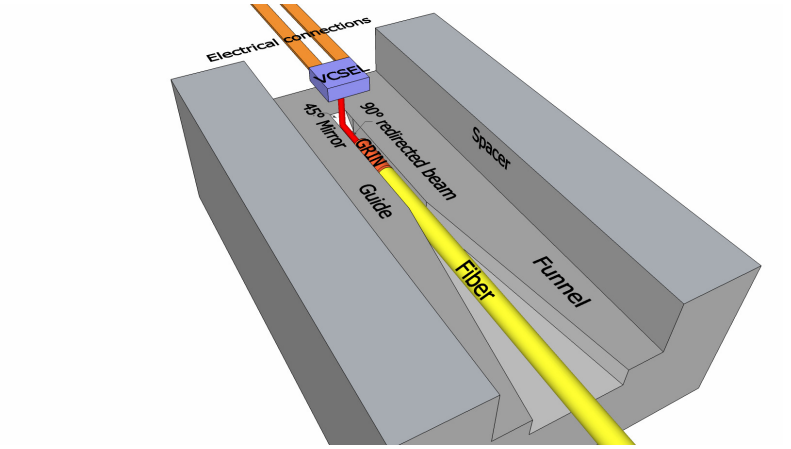

Figure 30. Model single channel microcoupler with the integrated devices

Starting with the assembly of the optical fibre in the coupler, the first components that play a role in the adjustment are the funnel and the guide. The fibre is guided up to the mirror, in the absence of the GRIN-lens. The spacer keeps a defined distance between the optoelectronic components and the mirror.

The optical coupler is the same for the transmitter and the receiver side.

To increase the coupling efficiency, this simple concept was extended with a coupling lens, which is realised as a GRIN-rod, placed in the same channel as the fibres, as shown in Figure 30.

The coupling structures are shown in Figure 31, for the multi-channel version.

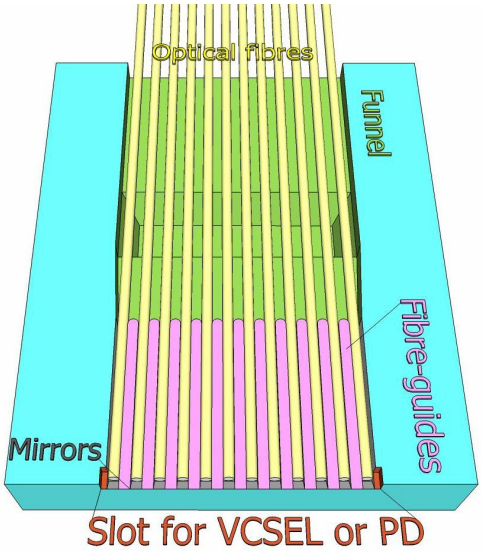

Figure 31. Model of the multi-channel optical coupler

3.2. Simulations

For estimating the coupling efficiency and the tolerances, a wave-optical simulation is used, in order to also include coherence and diffraction effects. For the simulation of light propagation between parallel planes, the Plane Wave Decomposition (PWD) approach is used. Here, the extension of this approach is to simulate propagation of

light, not only between tilted planes, produced by single-axis rotation of coordinate systems as, for example, by Matsushima et al [35], but also between planes that are placed in any arbitrary orientation [36]. This is necessary especially for tolerance analysis, where a general rotation must be considered.

3.2.1. Transformations between Shifted Orthonormal Coordinate Systems

The author follows the description given by Brenner [36].
In order to describe the transformation between coordinate systems the following geometry is used:

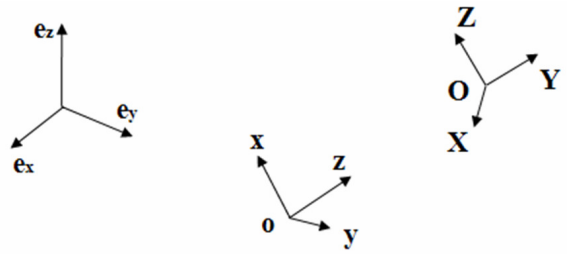

Figure 32. Coordinate systems used for the propagation from system **o** to system **O**

The $\mathbf{e}_x,\mathbf{e}_y,\mathbf{e}_z$ coordinate system is considered the global coordinate system. In the system located at **o,** the orthogonal unit vectors **x,y,z** represent the transmitting coordinate system. Likewise at **O,** the orthogonal unit vectors **X,Y,Z** represent the receiving coordinate system. An arbitrary point P is described in the three coordinate systems as:

$$\begin{aligned} \mathrm{P} &= p_x\mathbf{e}_x + p_y\mathbf{e}_y + p_z\mathbf{e}_z \\ &= \mathbf{o} + x\mathbf{x} + y\mathbf{y} + z\mathbf{z} \\ &= \mathbf{O} + X\mathbf{X} + Y\mathbf{Y} + Z\mathbf{Z} \end{aligned} \tag{3.1}$$

Through arithmetic operations the X,Y,Z components can be found from:

$$\begin{aligned} (\mathbf{o}-\mathbf{O})\mathbf{X} + x\mathbf{x}\mathbf{X} + y\mathbf{y}\mathbf{X} + z\mathbf{z}\mathbf{X} &= X \\ (\mathbf{o}-\mathbf{O})\mathbf{Y} + x\mathbf{x}\mathbf{Y} + y\mathbf{y}\mathbf{Y} + z\mathbf{z}\mathbf{Y} &= Y \\ (\mathbf{o}-\mathbf{O})\mathbf{Z} + x\mathbf{x}\mathbf{Z} + y\mathbf{y}\mathbf{Z} + z\mathbf{z}\mathbf{Z} &= Z \end{aligned} \tag{3.2}$$

Written in matrix form:

$$\begin{pmatrix} X \\ Y \\ Z \end{pmatrix} = \begin{pmatrix} \mathbf{x}\mathbf{X} & \mathbf{y}\mathbf{X} & \mathbf{z}\mathbf{X} \\ \mathbf{x}\mathbf{Y} & \mathbf{y}\mathbf{Y} & \mathbf{z}\mathbf{Y} \\ \mathbf{x}\mathbf{Z} & \mathbf{y}\mathbf{Z} & \mathbf{z}\mathbf{Z} \end{pmatrix} \begin{pmatrix} x \\ y \\ z \end{pmatrix} + \begin{pmatrix} (\mathbf{o}-\mathbf{O})\mathbf{X} \\ (\mathbf{o}-\mathbf{O})\mathbf{Y} \\ (\mathbf{o}-\mathbf{O})\mathbf{Z} \end{pmatrix} \tag{3.3}$$

Similarly for the small lettered coordinate system:

$$\begin{pmatrix} x \\ y \\ z \end{pmatrix} = \begin{pmatrix} \mathbf{Xx} & \mathbf{Yx} & \mathbf{Zx} \\ \mathbf{Xy} & \mathbf{Yy} & \mathbf{Zy} \\ \mathbf{Xz} & \mathbf{Yz} & \mathbf{Zz} \end{pmatrix} \begin{pmatrix} X \\ Y \\ Z \end{pmatrix} + \begin{pmatrix} \mathbf{(O-o)x} \\ \mathbf{(O-o)y} \\ \mathbf{(O-o)z} \end{pmatrix} \tag{3.4}$$

In the subsequent description an even shorter vector notation is used:

$$\mathbf{R} = \mathbf{T} \cdot \mathbf{r} - \Delta\mathbf{O}_{\mathrm{R}} \tag{3.5}$$

$$\mathbf{r} = \mathbf{t} \cdot \mathbf{R} + \Delta\mathbf{O}_{\mathrm{r}} \tag{3.6}$$

Since the bases of the coordinate systems are orthonormal, the transformation matrix has the following property:

$$\mathbf{t}^{-1} = \mathbf{t}^{\mathrm{T}} = \mathbf{T} \tag{3.7}$$

Thus **T** and **t** are unitary matrices.

3.2.2. Propagation between Tilted Planes using Plane Wave Decomposition

For propagation between parallel planes, the plan wave decomposition (PWD) is used (also known as angular spectrum method):

$$u(\mathbf{r}) = \frac{1}{(2\pi)^2} \iint \tilde{u}_0(\mathbf{k}_\perp) e^{i\mathbf{k}\cdot\mathbf{r}} d^2k_\perp \tag{3.8}$$

In order to describe the propagation between tilted planes, the transformations in equations (3.5) and (3.6), have to be applied to the position vectors and the wave vectors. Since the k-vectors are independent of the coordinate origin, these transformations are given by:

$$\begin{aligned} \mathbf{k} &= \mathbf{t} \cdot \mathbf{K} \\ \mathbf{K} &= \mathbf{T} \cdot \mathbf{k} \end{aligned} \tag{3.9}$$

Using the equations 4.6 and 4.9 the dot product $\mathbf{k} \cdot \mathbf{r}$ can be rewritten in terms of **K** and **R** as:

$$\mathbf{k} \cdot \mathbf{r} = (\mathbf{t} \cdot \mathbf{K})(\mathbf{t} \cdot \mathbf{R} + \Delta\mathbf{O}_{\mathrm{r}}) = (\mathbf{K} \cdot \mathbf{T})(\mathbf{t} \cdot \mathbf{R} + \Delta\mathbf{O}_{\mathrm{r}}) = \mathbf{K} \cdot \mathbf{R} + \mathbf{t} \cdot \mathbf{K} \cdot \Delta\mathbf{O}_{\mathrm{r}} \tag{3.10}$$

The difference of the coordinate origins results in an additional propagation phase: $\mathbf{t} \cdot \mathbf{K} \cdot \Delta\mathbf{O}_{\mathrm{r}}$. Introducing these transformations in eq. (3.9):

$$u(\mathbf{r}) = \frac{1}{(2\pi)^2} \iint \tilde{u}_0\left((\mathbf{t} \cdot \mathbf{K})_\perp\right) e^{i\mathbf{t}\cdot\mathbf{K}\cdot\Delta\mathbf{O}_{\mathrm{r}}} e^{i\mathbf{K}\cdot\mathbf{R}} \left|\mathbf{J}_{k,K}\right| d^2K_\perp \tag{3.11}$$

The factor $e^{i\mathbf{K}\cdot\mathbf{R}}$ in equation (3.11) indicates that the propagation between tilted planes can be calculated with an FFT just as the PWD.

The change of the area element $d^2k_\perp$ to the new area element $d^2K_\perp$ results in an additional weight factor, given by the Jacobian of the transformation.

Thus, the Jacobian accounts for an amplitude correction regarding energy conservation, since waves starting from the small-lettered coordinate system with a specific angle arrive at capital-lettered coordinate system with a different angle.

The Jacobian can be calculated in an analytic form, as shown in equation (3.12):

$$\mathbf{J}_{k,K} = \frac{\partial(\mathbf{k}_\perp)}{\partial(\mathbf{K}_\perp)} = \begin{pmatrix} \mathbf{Xx} - \mathbf{Zx}\frac{K_x}{K_z} & \mathbf{Yx} - \mathbf{Zx}\frac{K_y}{K_z} \\ \mathbf{Xy} - \mathbf{Zy}\frac{K_x}{K_z} & \mathbf{Yy} - \mathbf{Zy}\frac{K_y}{K_z} \end{pmatrix} \tag{3.12}$$

3.2.3. Effect of Tilt and Shift in the Coupling System

The optical system to be simulated has the following components: parallel and tilted planes; reflecting surfaces; wave sources with defined beam profiles; and apertures on the different surfaces. For the analysis of tilt and shift on the coupling efficiency, the system shown in Figure 33 was simulated.

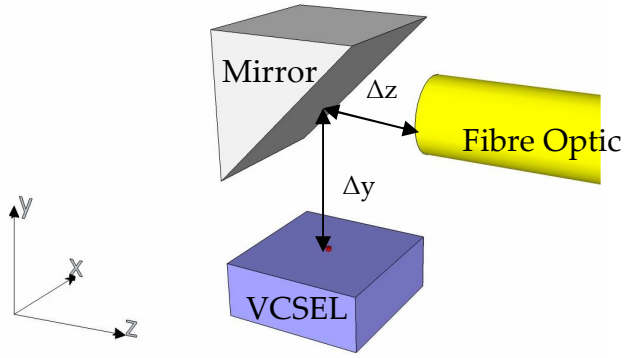

Figure 33. Start set-up for the simulation

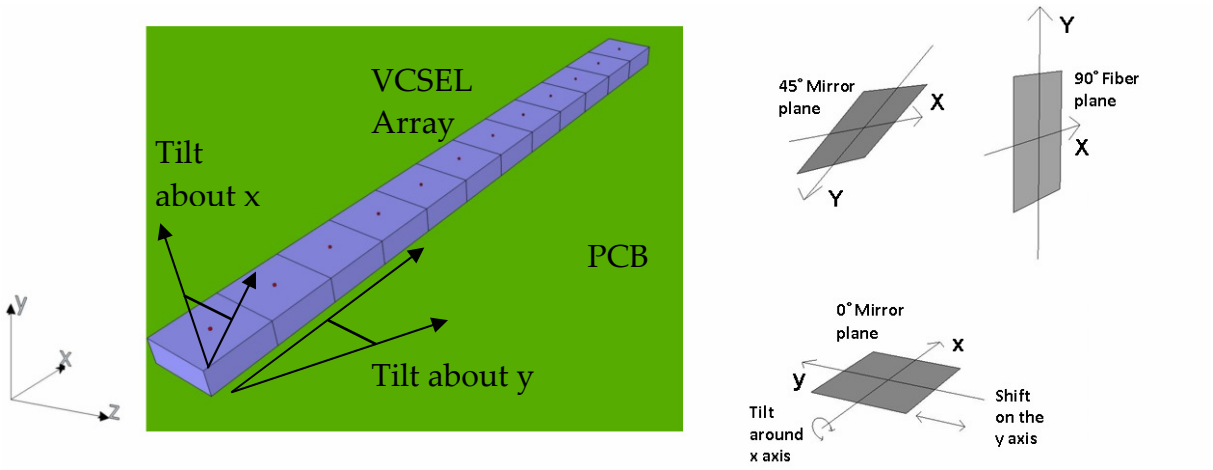

Figure 34. Relevant tilt angles of the VCSEL array with respect to the PCB

According to the fabrication process, the mirror is embedded in the coupler and the fibre optics are fixed to the coupler. Here, a tilt of the VCSEL as a rotation around the x axis is considered, as shown in Figure 34 is considered.

After propagation, the obtained field, i.e. the electrical field, is scalar multiplied with itself to obtain the intensity distribution:

$$I = \sqrt{\frac{\varepsilon\varepsilon_0}{\mu\mu_0}} \left\langle E^2 \right\rangle \tag{3.13}$$

In Figure 35 the intensity distributions at the three surfaces are shown.

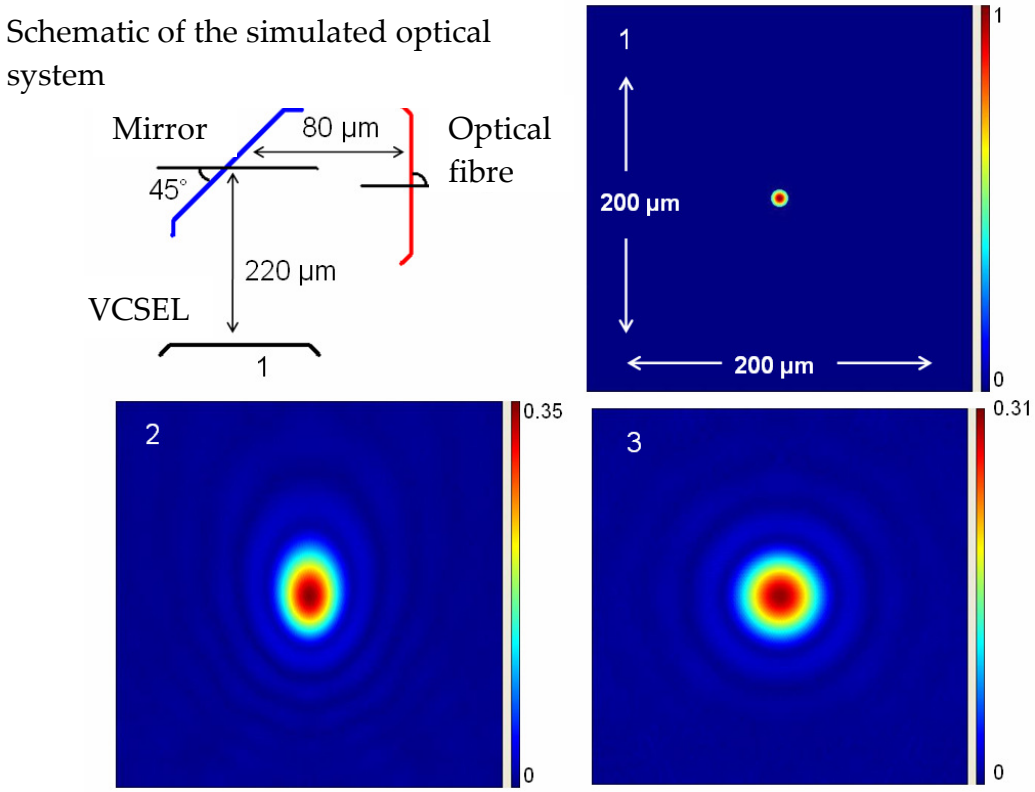

Figure 35. Intensity fields at the surfaces of interest

The system of Figure 33 was simulated using parameters of commercially available VCSELs and multimode fibres. The distances between the individual optical devices were defined, according to the design of the micro optical-coupler.

The simulation parameters are shown in Table 4.

Wavelength [nm]	Divergence half angle of Gauss Beam [Deg]	Diameter of VCSEL's emitting area [µm]	Core diameter of the fibre optic [µm]	Distance VCSEL-Mirror (Δy) [µm]	Distance Mirror-fibre optic (Δz) [µm]
850	10	10	62.5	150	20

Table 4. Parameters for simulation of the coupling system

The tilt angle around the x axis was varied, as shown at the top of Figure 36. Within a tilt angle of ±0.5 degrees, the coupling efficiency has a constant value of approximately 90%. The effect of shift between the optical coupler (mirror and optical fibre) and VCSEL is shown in the bottom graphic of Figure 36.

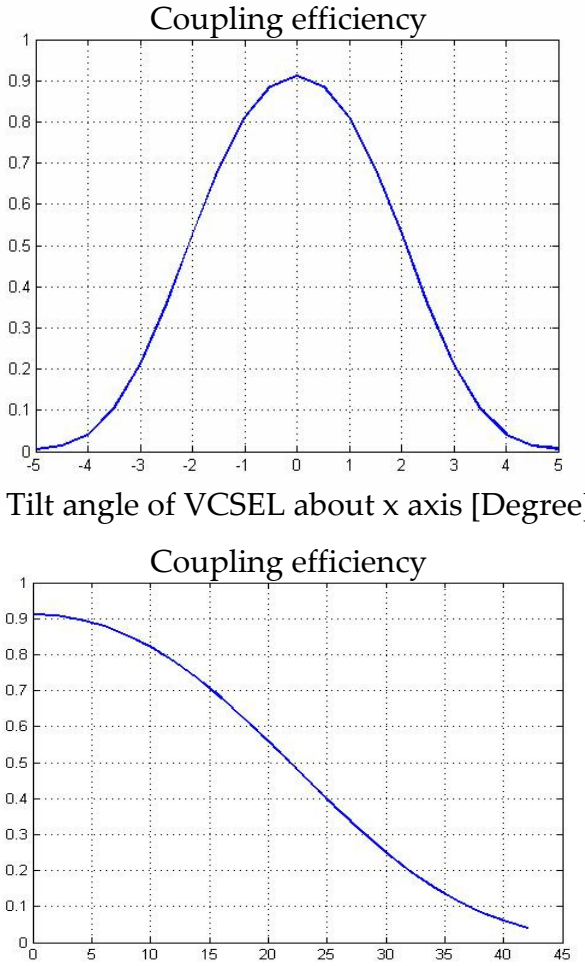

Figure 36. Effect of tilt and shift on the coupling efficiency

The coupling efficiency was calculated comparing the intensities on the source plane and on the fibre plane:

$$Eff. = \frac{\mathbf{I_f}}{\mathbf{I_s}} \tag{3.14}$$

Where $\mathbf{I_f}$ is the total intensity on the end surface of the fibre, taking into account that only the field that falls into the 62.5 diameter core is coupled into the fibre, and $\mathbf{I_s}$ is the total intensity on the emitting surface of the source.

3.2.4. Some Aspects of the Implementation of the Computer-Assisted Wave-Simulation Tool

Some considerations about the implementation of the simulation tool are presented in this chapter.

3.2.4.1. k-space

The procedure to calculate the **k**-vectors is listed bellow:

a. **K**-vectors are calculated with the following sampling:

$$d\nu = \left(\frac{1}{N_x dx}\right) \qquad d\mu = \left(\frac{1}{N_y dy}\right) \tag{3.15}$$

Where $N_x = N_y = 512$ is the size of the square array used to calculate each of the amplitude distributions on the planes of interest.

b. The validity of the **k**-vectors is proven after the Ewald's sphere:

$$k_z = \sqrt{k_0^{\,2} - k_x^{\,2} - k_y^{\,2}} \quad \text{for } k_0^{\,2} > k_x^{\,2} + k_y^{\,2} \tag{3.16}$$

c. For those **K**-vectors that are not able to propagate -that is, those in the Ewald's sphere that were cut by the tilted plane- their phase and amplitude were set to zero.

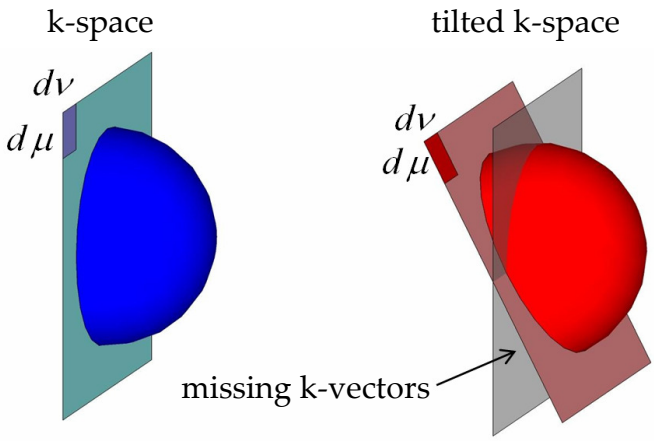

Figure 37. k-space before and after the tilt

d. After the transformation **k=t·K** a mapping of the **k**-vectors to the corresponding **K**-vectors is made.

As shown in Figure 30, there are some k-vectors that were not taken into account. It affects mainly tilted planes in which the amplitude distributions are affected.

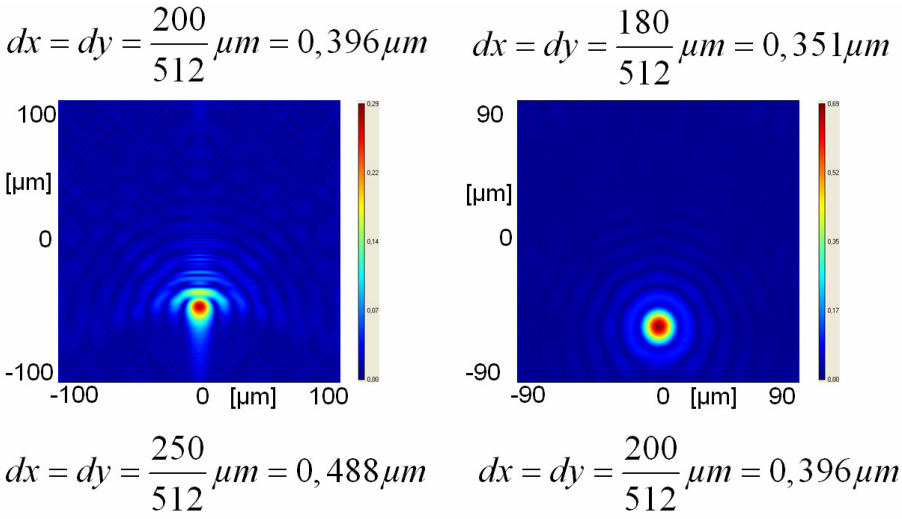

Figure 38. Left: distortion of the undersampled field after reflection by a 55° tilted surface, right: same field with a higher sampling frequency

As shown in Figure 38, there is also a dependency on the sampling frequency.

3.2.4.2. Selection of the coordinate system

The choice of the coordinate system is crucial for the calculation of the amplitude and phase distributions.

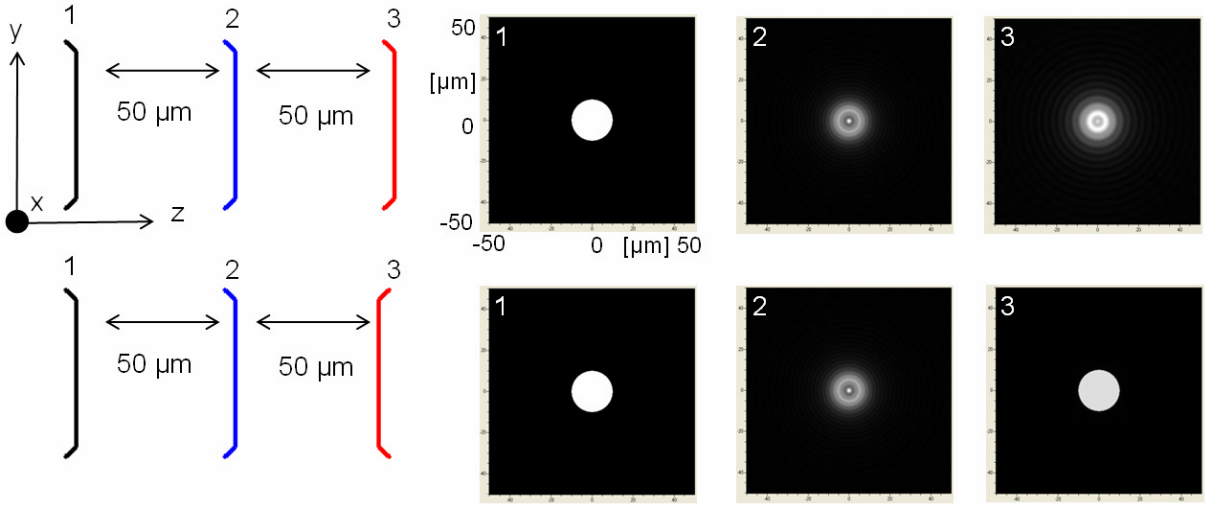

Figure 39. Effect of choosing the direction of propagation in two opposite ways

The brackets on the lines, representing the planes in which the distributions are calculated, indicate the direction of propagation. As shown in Figure 39, if the third surface chosen is 180° degrees relative to the direction of propagation, it is

interpreted as a negative distance in the RDS (Rayleigh-Debye-Sommerfeld) propagation model.

Figure 40. Place of start "**o**" and goal "**O**" coordinate systems

This is shown as an example in the following expressions taking, θ as shown in Figure 40.

$$u(\mathbf{r}) = \frac{1}{(2\pi)^2} \iint \tilde{u}_0 \left((\mathbf{t} \cdot \mathbf{K})_\perp \right) e^{i\mathbf{t}\cdot\mathbf{K}\cdot\Delta\mathbf{O}_r} e^{i\mathbf{K}\cdot\mathbf{R}} \left| \mathbf{J}_{k,K} \right| d^2 K_\perp \tag{3.17}$$

$$\begin{aligned} \mathbf{t}\cdot\mathbf{K}\cdot\Delta\mathbf{O}_r &= \begin{pmatrix} 1 & 0 & 0 \\ 0 & \cos\theta & \sin\theta \\ 0 & -\sin\theta & \cos\theta \end{pmatrix} \begin{pmatrix} K_x \\ K_y \\ K_z \end{pmatrix} \cdot \begin{pmatrix} 0 \\ 0 \\ \Delta z \end{pmatrix} = \left(-K_y \sin\theta + K_z \cos\theta \right) \Delta z \\ &= \begin{pmatrix} 1 & 0 & 0 \\ 0 & -1 & 0 \\ 0 & 0 & -1 \end{pmatrix} \begin{pmatrix} K_x \\ K_y \\ K_z \end{pmatrix} \cdot \begin{pmatrix} 0 \\ 0 \\ \Delta z \end{pmatrix} = \left(-K_z \right) \Delta z \end{aligned} \tag{3.18}$$

Any surface (i.e. blue) is defined as a mirror if the next surface (red) is placed on the side in which a further propagation was negative for the surface in question (see Figure 41).

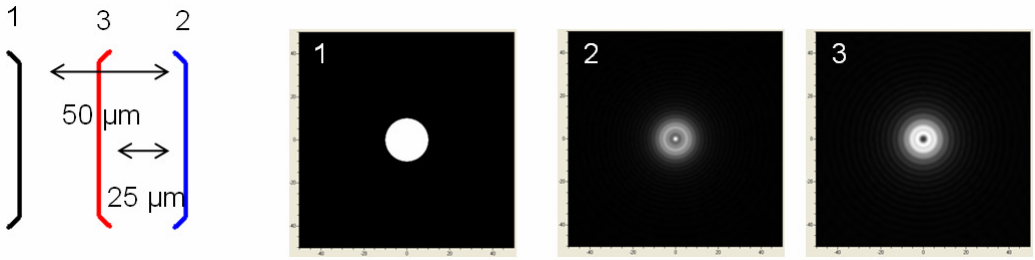

Figure 41. Example of plane choice for propagation after a mirroring surface

If the red plane is placed on the side of the blue plane in which the further propagation is positive, the blue surface does not have any effect (see Figure 42).

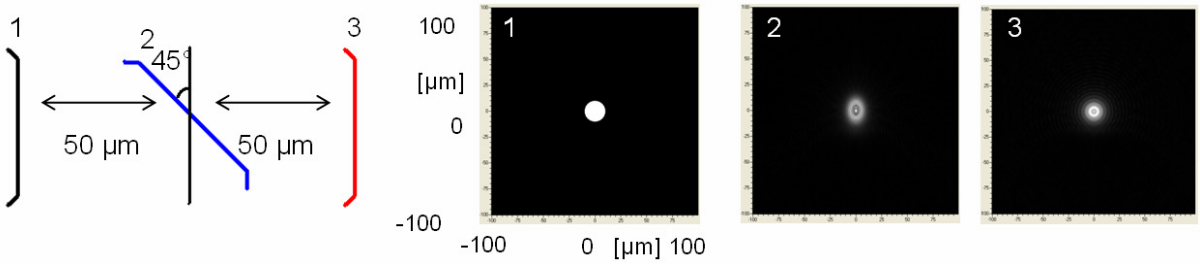

Figure 42. The distribution can be calculated at the second surface but it does not have any effect for the third one

Figure 43 shows the rotation of the image after the reflection of a non-symmetric intensity distribution. The sampling effects can be observed again in the amplitude distributions on the top of the figure.

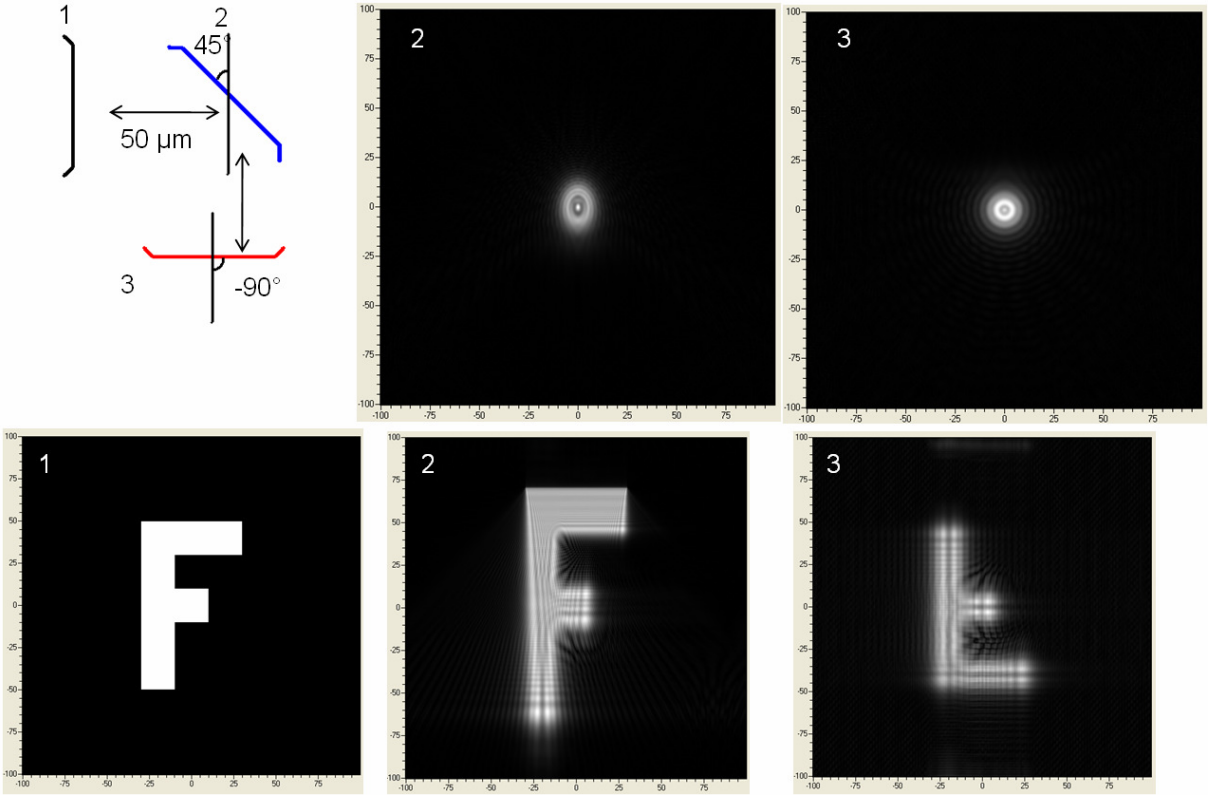

Figure 43. Rotation of the image after reflection

For the specific case of the designed coupling system, the tilt of the VCSEL was modelled as a horizontal source with a mirror that redirects the beam, and whose angle can be varied in order to simulate a tilt of the device. The optical fibre was modelled by the third surface using a pinhole of 50µm diameter that corresponds to the fibre core (see Figure 44).

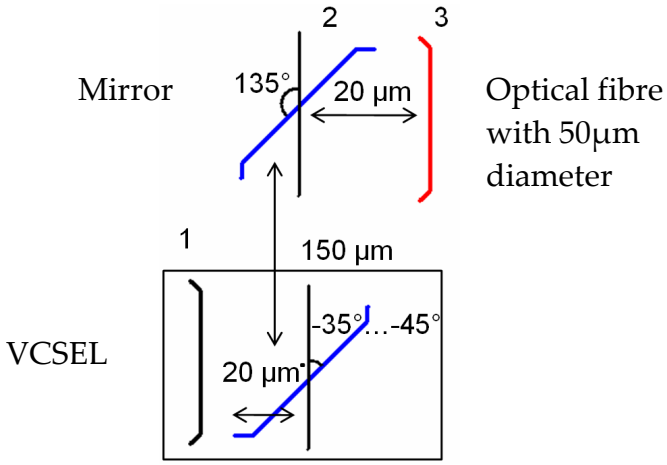

Figure 44. Set-up for the simulation of the constructed system

Some of the obtained distributions are shown in Figure 45; i.e. for simulation of misalignment between the devices of the system.

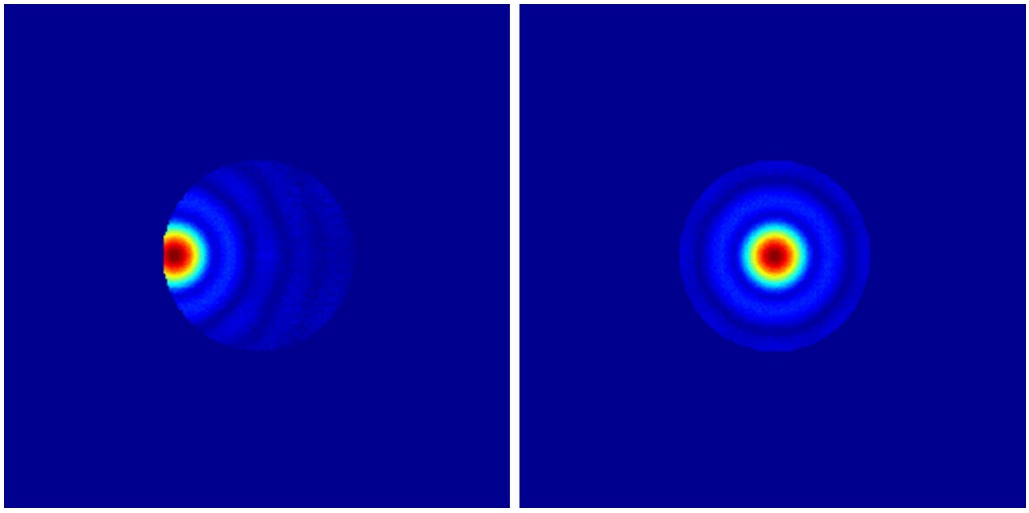

Figure 45. Amplitude distributions of a system with 20µm (left) and 0 µm shift between VCSEL and fibre core

3.3. Optimisation

The VCSEL emits a divergent beam that has to be coupled into the optical fibre. One possibility to increase the light coupling efficiency is the addition of a lens for collecting the divergent rays. By using the coupling structure and a GRIN-rod lens with the adequate diameter, the coupling efficiency can be maximised and the adjusting effort between the optical devices can be minimised.

First, the imaging properties of the GRIN-lens are explained and then some measurements are shown, in order to establish a comparison between theory and practice.

3.3.1. Paraxial imaging formula

The next imaging formulas are based on the paraxial ABCD-matrix theory [37].

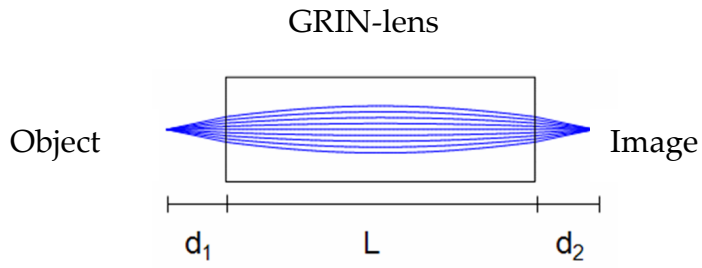

Figure 46. Imaging through a GRIN lens

For example, if the lens has a parabolic profile index profile [38]

$$n(r) = n_0 + n_{r2} r^2 \tag{3.19}$$

where n_0 is the refractive index in the core centre and n_{r2} is a parameter that depends on the material and fabrication method, the perfect imaging is achieved when d_1 the distance to the object, d_2 the distance to the image and L the length of the GRIN-rod fulfil the next equation.

$$\operatorname{atan}\left(d_2\sqrt{-2n_0 n_{r2}}\right) + \operatorname{atan}\left(d_1\sqrt{-2n_0 n_{r2}}\right) + \frac{L}{n_0}\sqrt{-2n_0 n_{r2}} = \pi \tag{3.20}$$

The scaling factor is given by:

$$m = \sqrt{\frac{1-2n_0 n_{r2} d_2^2}{1-2n_0 n_{r2} d_1^2}} \tag{3.21}$$

In order to describe the dispersion in the lens, the manufacturer makes use of the Sellmeier-formula:

$$\begin{cases} n_{\text{zemax}}^2(\lambda, r) = n_{ref}^2(r) + K_1(r)\cdot\left(1 - \dfrac{\lambda_{ref}^2}{\lambda^2}\right) \\ n_{ref}(r) = n_0 + n_{r2}\cdot r^2 + n_{r4}\cdot r^4 \\ K_1(r) = K_{11} + K_{13}\cdot n_{ref}^2(r) \end{cases} \tag{3.22}$$

where n_{zemax} is the refractive index at the wavelength λ_{ref} used for the ray-tracing simulation in Zemax, n_{ref} is the refractive index modelled as a power-series without regard to dispersion, and the $K_{\#}$ constants refer to dispersion coefficients of a determined material at a determined temperature.

3.3.2. Simulation: Comparison of the exact and the approximated Formulas

The expression for the refractive index with dispersion is developed in a power series n_{fit}:

$$\begin{cases} n_{fit}(\lambda, r) \cong n_0(\lambda) + n_{r2}(\lambda) \cdot r^2 \\ n_0(\lambda) = \sqrt{n_0^2 + \left(K_{11} + K_{13} n_0^2\right) \dfrac{\lambda^2 - \lambda_{ref}^2}{\lambda^2}} \\ n_{r2}(\lambda) = \dfrac{n_0 n_{r2}}{n_0(\lambda)} \left(1 + K_{13} \dfrac{\lambda^2 - \lambda_{ref}^2}{\lambda^2}\right) \end{cases} \tag{3.23}$$

As shown in the Figure 47, the second order polynomial is a good approximation of the refractive index. The comparison is made for two reference wavelengths of 850 nm and 525 nm.

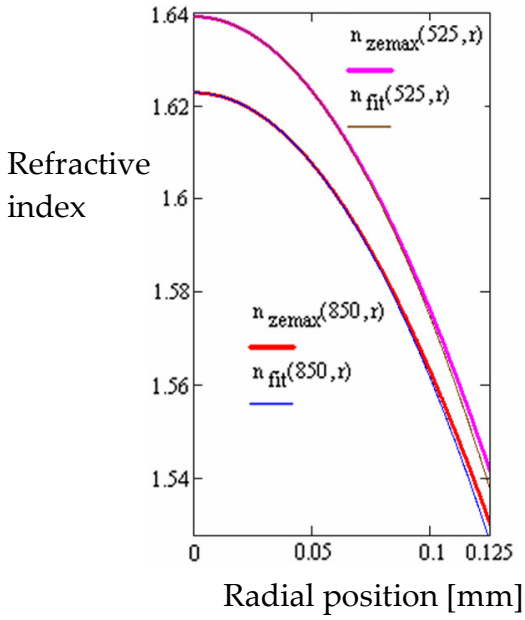

Figure 47. Comparison of the exact refractive index to the 2^{nd} order approximation

Figure 48 shows the spherical aberration of the GRIN lens.

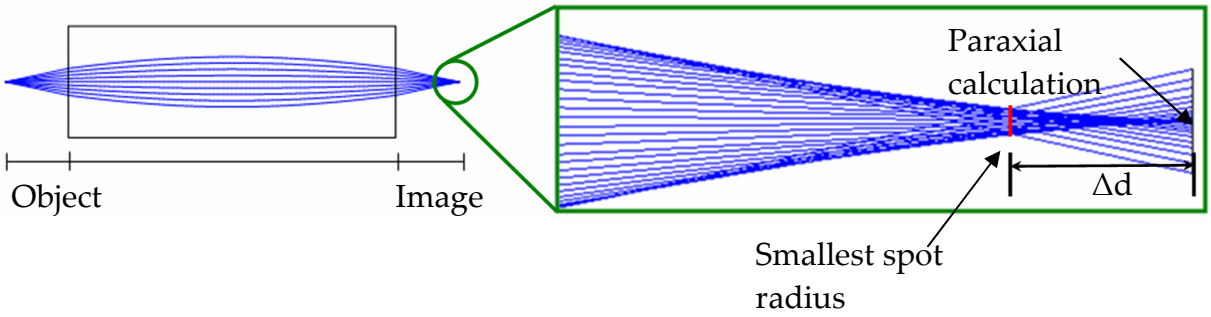

Figure 48. Negative spherical aberration of the GRIN lens

Using the approximated refractive index some foci are calculated and compared to the simulation with the Sellmeier-formula used by Zemax.

The results are shown in the Table 5, where the scaling factor m is also given.

λ_{ref} [nm]	850			525		
Distance to object d_1 [µm]	d_2 [µm] / m (paraxial)	d_2 [µm] smallest Spotradius (Zemax)	Δd [µm]	d_2 [µm] / m (paraxial)	d_2 [µm] smallest Spotradius (Zemax)	Δd [µm]
50	288 / 1.59	276	-16	253 / 1.50	237	-16
100	192 / 1.20	177	-15	167 / 1.15	150	-17
150	134 / 0.97	122	-12	114 / 0.93	100	-14
200	95 / 0.81	86	-9	77 / 0.78	68	-11
250	67 / 0.70	60	-7	51 / 0.67	45	-6

Table 5. Parameters for simulation of the coupling system

3.3.3. Measurement of a GRIN-Rod Lens

3.3.3.1. First Measuring Set-up: Search of the Lens-Focus

For verification of the imaging characteristics of the GRIN-rod lens a first experimental set-up was constructed (see Figure 49).

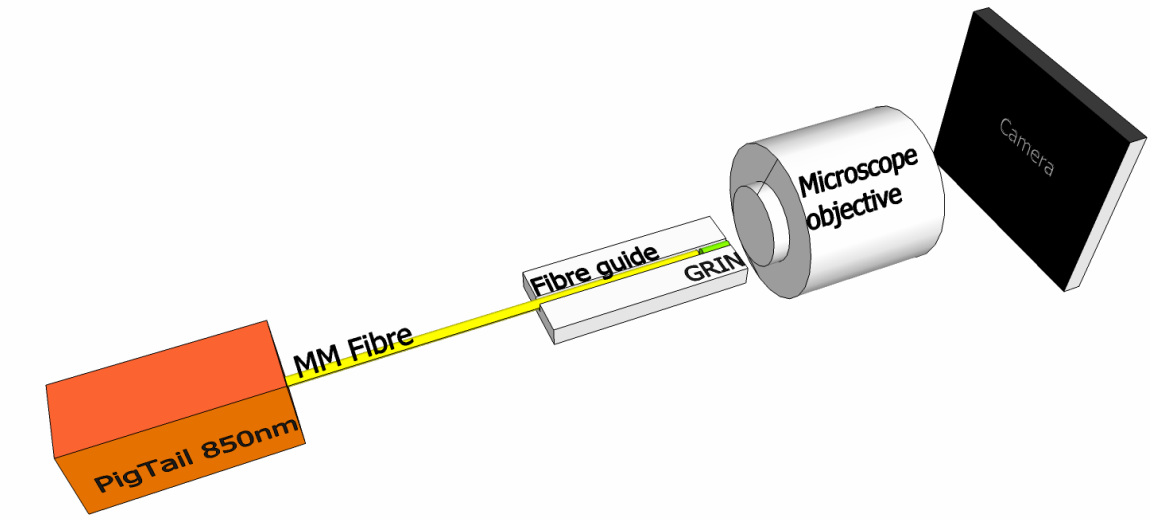

Figure 49. Sketch of the first set-up for verification of the GRIN imaging characteristics

The characteristics of the devices in the set-up are:

- Pigtailed Laser (VCSEL) λ=850nm
- MM Fibre: Core/Cladding/Coating [µm]=62,5/125/250
- GRIN-rod lens. Length=729µm Diameter=250µm
- Fibre guide manufactured lithographically
- Microscope-Objective Tube length=160mm N.A.=0,5
- CCD camera without white balance and brightness control.

In the first experiment, the laser was let off and the microscope objective was focused on the end-surface of the GRIN-lens. This position was taken as reference for the measurement of the image-distance d_2 as shown in the Figure 50.

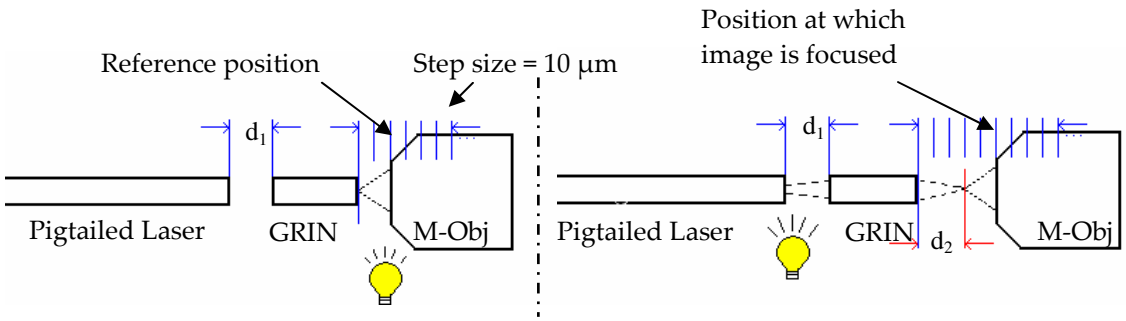

Figure 50. Left: Microscope objective focused on the end surface of the GRIN lens Right: Microscope objective focused on the imaged end surface of the pigtailed laser's fibre

In the second step, the microscope objective was moved along the optical axis in 10 µm steps from the reference position, until a sharp image of the pigtailed laser's fibre-end was obtained. The obtained images are shown in the Figure 51.

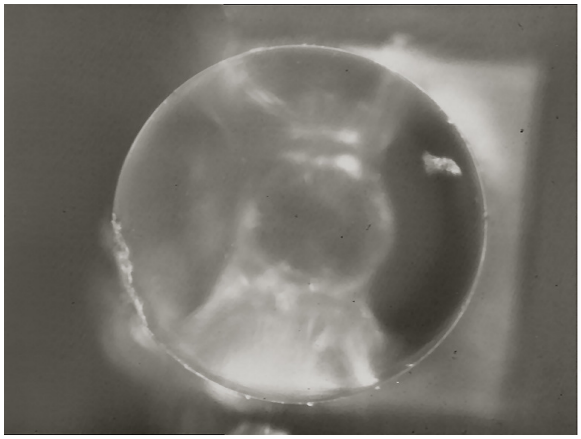

End surface of the GRIN-rod lens

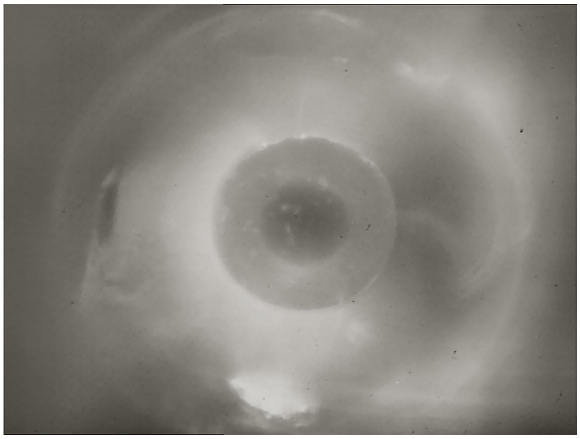

Through the GRIN lens imaged end surface of the pigtailed laser's fibre

Figure 51. Obtained images of the first experiment: surfaces illuminated with a thermal lamp

In the second experiment, the laser was turned on and the light bulb off, the microscope objective was focused on the end-surface of the GRIN-lens. This position was taken as reference again for the measurement of the image-distance d_2, as shown in Figure 52.

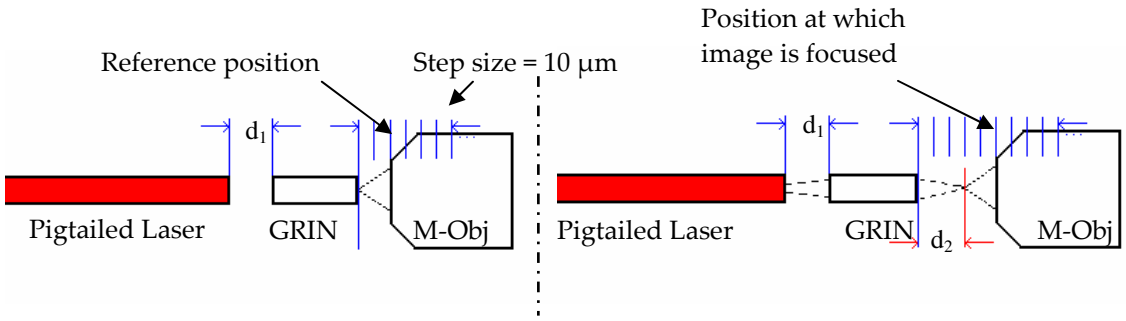

Figure 52. Left: Microscope objective focused on the end surface of the GRIN lens Right: Microscope objective focused on the imaged end surface of the pigtailed laser's fibre

As in the first experiment, the microscope objective was moved along the optical axis in 10 µm steps from the reference position until a sharp image of the pigtailed laser's fibre-end was obtained. As shown in the Figure 53 the end surface of the GRIN-rod lens cannot be identified, so that the reference distance was assumed from the first measurement. The distance to the image was estimated by observing some dust particles on the fibre's end surface of the pigtailed laser.

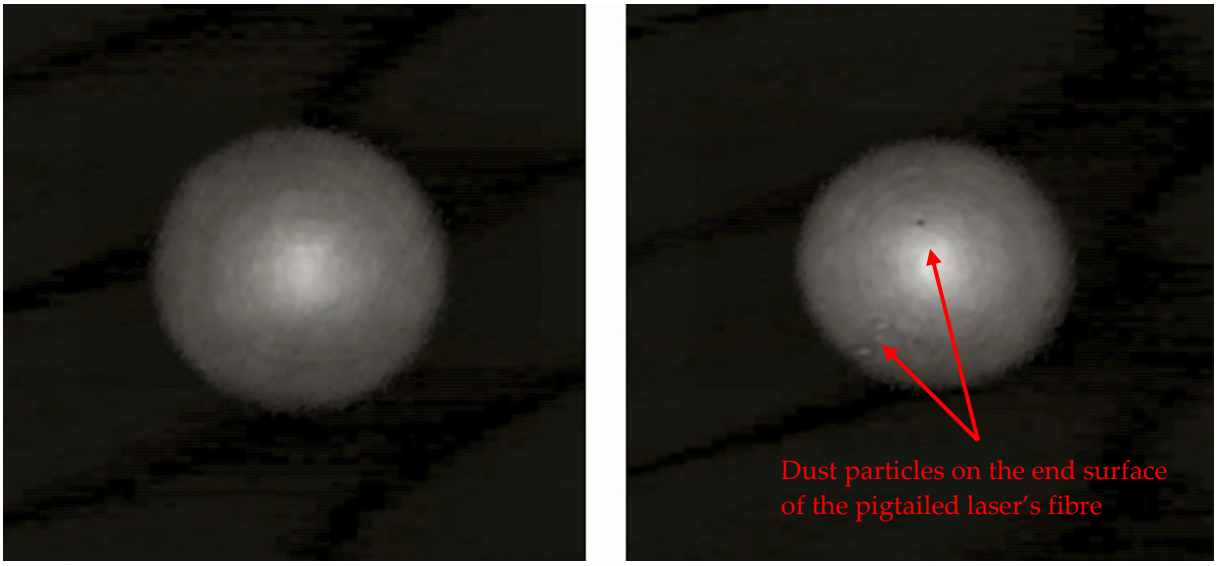

End surface of the GRIN-rod lens cannot be recognised

End surface of the pigtailed laser's fibre imaged by the GRIN lens

Figure 53. Obtained images of the second experiment: surfaces illuminated with the light of the pigtailed laser

3.3.3.2. Second Measuring Set-Up: Analysis of the Intensity Distribution

Another method for the determination of the imaging characteristics of the GRIN-rod lens is the analysis of the FWHM (Full Width Half Maximum) of the wave coming out from the GRIN, which propagates in the air. The propagation of a Gaussian wave starts from a point light source. A single mode fibre has a very small core diameter that can be used for this purpose. The set-up for this experiment is shown in Figure 54.

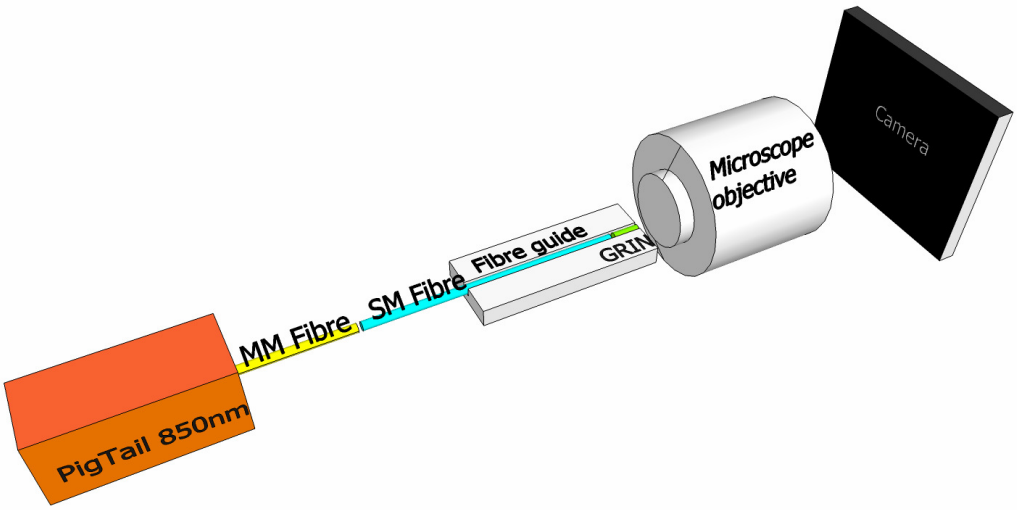

Figure 54. Sketch of the second set-up for verification of the GRIN imaging Characteristics

The dimensions of the single mode fibre are: Core/Cladding/Coating [μm]=5/125/250

The start position is the same as in the first experiment. The microscope objective was moved from the start position along the optical axis in 10 μm steps and, in each step, the image obtained by the camera was saved. After that, the FWHM was computed, taking into account that the brightest pixel takes the value 255 and the darkest 0. The profile of an intensity distribution is shown in Figure 55. There, the greyscale values of the image were added in the x-direction of the camera chip, and the result divided by the size (number of pixels) of the camera chip in the x-direction.

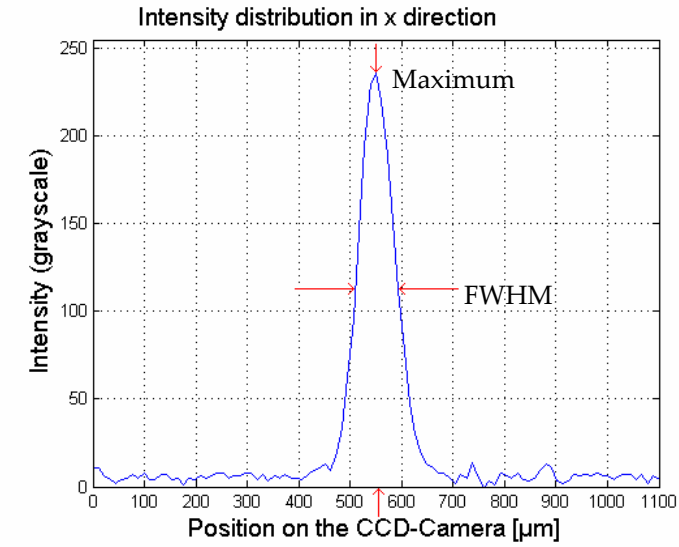

Figure 55. Intensity distribution obtained adding the pixel-values over the x-direction

The FWHM and the maximum of the obtained 1D-distribution were evaluated in 20 μm steps, starting at the reference position. The work distance d_2 is determined by evaluating the lowest FWHM and the highest maximum as shown in Figure 56.

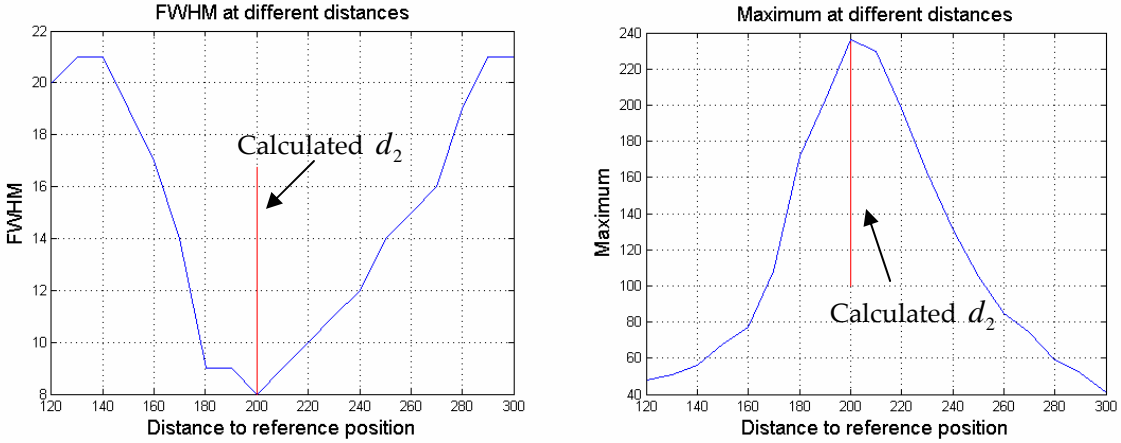

Figure 56. FWHM and maximum graphics for the evaluation of the work distance d_2

The red lines in Figure 56 show the calculated work distance at the image side, for a work distance of 95 µm at the object side.

These experiments were repeated for different work distances at the object side d_1, and compared with the visible light source utilised (see Table 6). The results of the simulation (Table 5) are included. The results can also be seen graphically in Figure 57.

Wavelength [nm]	525		
Working distance d_1 GRIN-Source [µm]	d_2 Calculation [µm]	d_2 Simulation [µm]	d_2 Measurement [µm]
50	252	237	200
90	180	163	170
130	132	118	130
139	123	109	120
172	96	84	90

Table 6. Comparison of the results for the experiments with visible light illumination

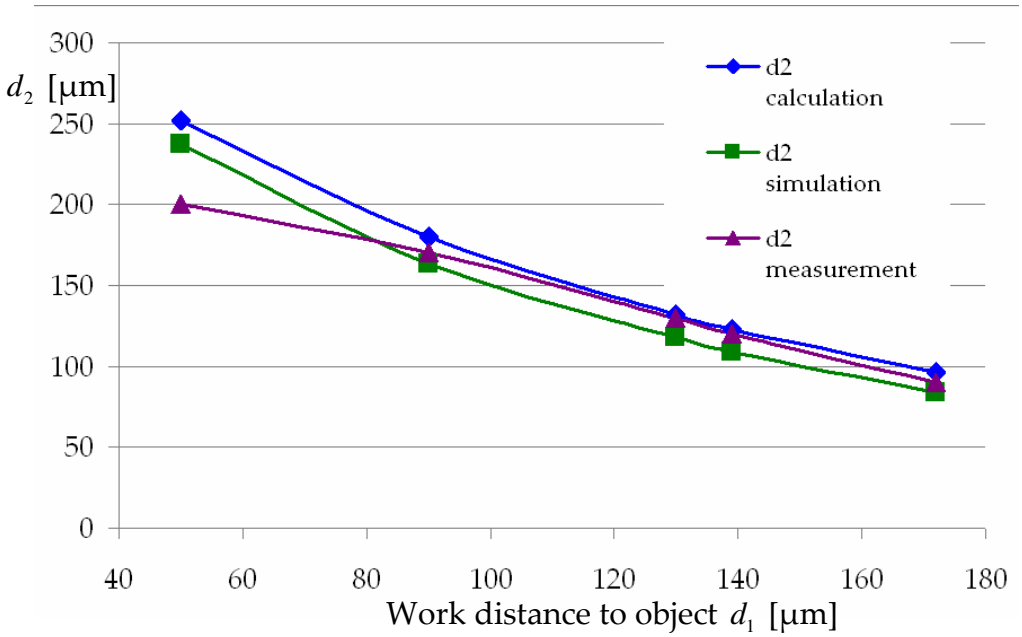

Figure 57. Graphic of the results in the Table 6

For the experiments made with infrared light, the results are shown in Table 7. The corresponding graphic is shown in Figure 58, where the results corresponding to the evaluation of the FWHM and the maxima are not shown because they are identical to those obtained in the measurement.

Wavelength [nm]	850			
Working distance d_1 GRIN-Source [µm]	d_2 Calculation [µm]	d_2 Simulation [µm]	d_2 Measurement [µm]	d_2 Evaluation of FWHM [µm]
55	275	264	250	250
95	200	185	200	200
133	151	138	150	140
151	133	121	130	130
220	82	75	90	90

Table 7. Comparison of the results for the experiments with infrared light illumination

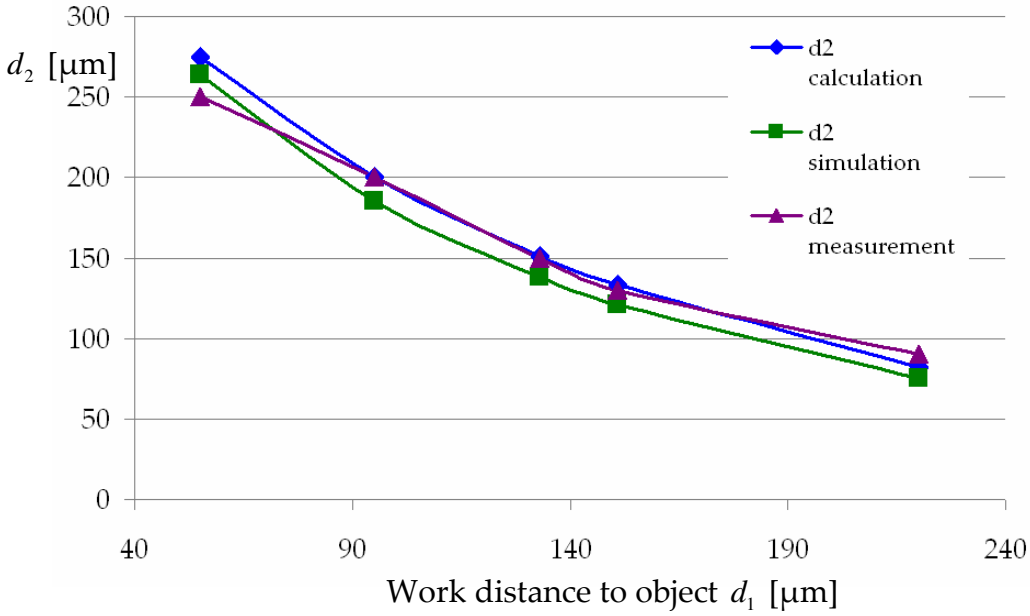

Figure 58. Graphic of the results in the Table 7

3.3.3.3. Third Measuring Set-Up: The Coupling Efficiency

The third experiment is based on the measurement of the efficiency in a direct coupling set-up. A sketch of the set-up is shown in Figure 59.

Figure 59. Sketch of the third set-up: measurement of the coupling efficiency

Here, the coupled power in the single mode fibre is measured and compared for the case of direct coupling of the divergent beam, and for the case in which the beam is focused with the GRIN-rod lens, as shown in Figure 60. The distances d and d_1 are held as parameters for the comparison, while d_2 is varied according to the measurement curve obtained in the second experiment.

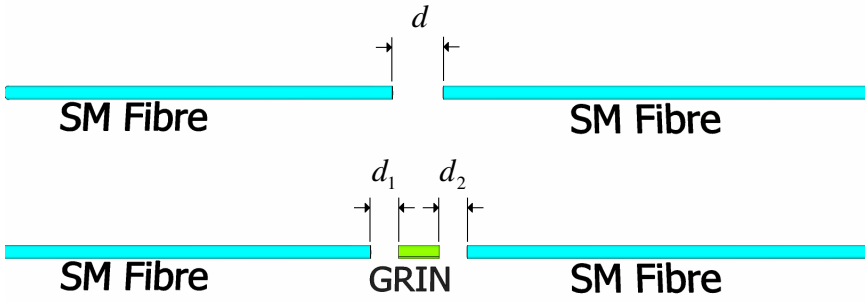

Figure 60. Distances taken as parameter for the comparison

The results are shown in the Table 8 and in Figure 61.

Work distance $d = d_1$ [μm]	Measured Power with GRIN/	dB
100	1.76	2.47
140	4.62	6.65
200	5.81	7.64
250	47.50	16.77

Table 8. Comparison of the results for the experiments with infrared light illumination

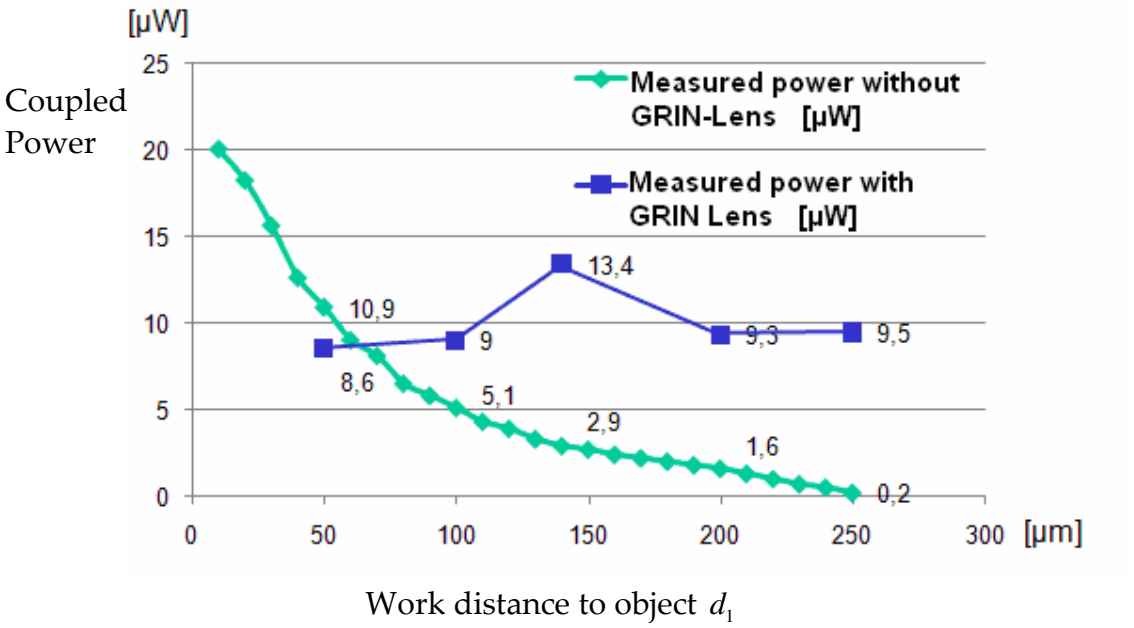

Figure 61. Comparison of the coupled power with and without GRIN

3.4. Conclusions

- A novel coupling concept was developed and implemented in single- and multi-channel versions. The coupler integrates several optical and mechanical devices in a monolithic construction that eases the test and the integration with electronic devices.
- The method purposed by Brenner for the calculation of fields that propagate between tilted planes was implemented. The tool is very helpful to rapidly determine tolerances and define limits in the design process of adjusting systems and the devices involved in it.
- GRIN-rod lenses can be easily integrated in the microcoupler so that they do not represent additional adjusting effort in the optical system but additional mechanisms have to be developed for the fixture of the lenses in the optical coupler.
- The imaging properties of GRIN-rods were studied and compared with laboratory measurements. The results show a very good agreement.
- The use of GRIN-rod lenses in the coupling systems increases the coupling efficiency considerably, specially for systems with more than 100µm work distance.

4. Optical Micro-Integration

The integration of optical and electronic micro devices for optical communication systems are related strongly to the fabrication methods of the optical devices and adjusting mechanisms, used for the alignment of the devices. As shown in Chapter 4, only a few micrometres of misalignment are allowed in order to guarantee a light-efficient coupling. As a result of the simulations, the accuracy requirements for the fabrication methods are also in the domain of 1 to 2 μm. With regard to the premise of a cost-effective fabrication method, the use of high precision instruments for the manufacture of each one of the couplers is not worth considering.

The optical coupler is fabricated by the replication of a master with plastic polymers. First, the master can be manufactured using complex and time-consuming methods that fulfil the requirements and, second, the fine structured master can be replicated using very low viscosity polymers, in order to guarantee an identical replica of the master. For the fabrication of the master, two methods were considered: photolithography, and the micromachining of metal substrates.

The alignment of the devices is made using markers on the PCB in which the devices are to be placed.

4.1 Fabrication of the optical coupler

4.1.1. Fabrication of the Master using Photolithography

The photolithography is a well known method for the fabrication of integrated circuits and micro optics [40]. The fabrication of the master is a two-step process that begins with the fabrication of a mask using laser lithography. The desired geometry is written directly on a chrome mask and after that the substrate is chemically etched, and the exposed areas are removed. A picture of the obtained binary mask used for the single channel coupler is shown in Figure 62, top-left.

The next step is known as deep ultraviolet (UV) lithography and consists of the exposure of a photoresist under ultraviolet radiation, as shown in Figure 62, top-right. The used negative photoresist is SU-8. The non-exposed resist is dissolved after chemical development of the substrate. The exposure dose and other parameters for the fabrication of the master were taken from results of the group of Brenner [35], as well as the method for the fabrication of inclined structures [39]. In Figure 62, bottom-left, the obtained master is shown. The photoresist in the areas of the fibre guide and the funnel was removed. In Figure 62, bottom-right, a plastic replica of the SU-8 master shows the rough surface of the mirror. The surface is structured in the direction of the incoming UV radiation. Examinations about the cause of these microreefs explain that they are a result of inhomogeneity of the UV lamp used for the exposure, and possibly the aging effects of the photoresist [35].

The obtained surfaces are compared to those obtained by the metal milling method, in order to choose of one of them for the fabrication of the prototypes.

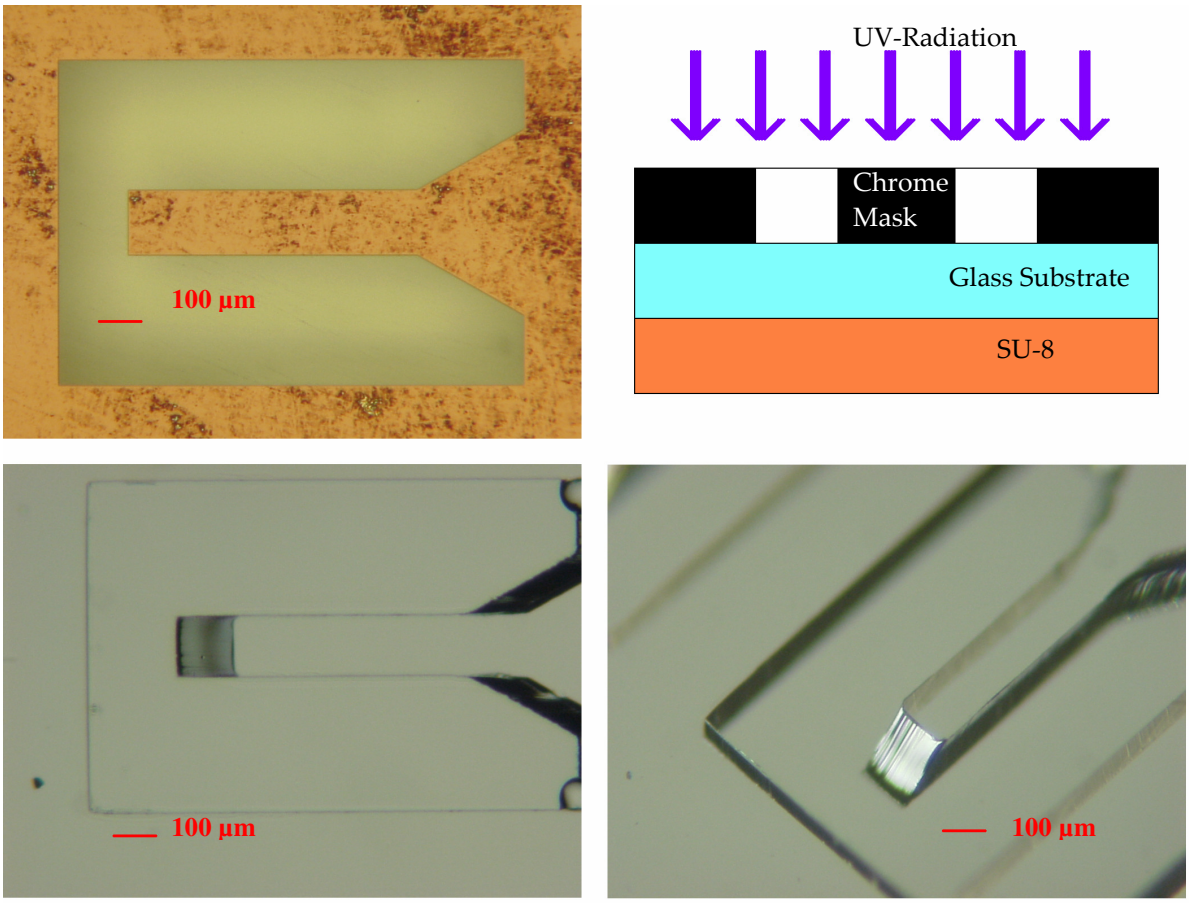

Figure 62. Fabrication of the master using photolithography. Top-left: chrome mask for the single channel, top-right: exposure of the SU-8 under UV-radiation, bottom-left: SU-8 master, bottom-right: plastic replica of the SU-8 master

There is an interesting feature of the lithographic method, namely the possibility of fabricating mirrors with surfaces other than planes. By writing the appropriate mask, cylindrical mirrors can be manufactured [35], and the divergent beams from the VCSEL can be collected in one of the dimensions of the wave front.

The obtained optical coupler is shown in Figure 63, with the embedded components for the adjustment and mounting.

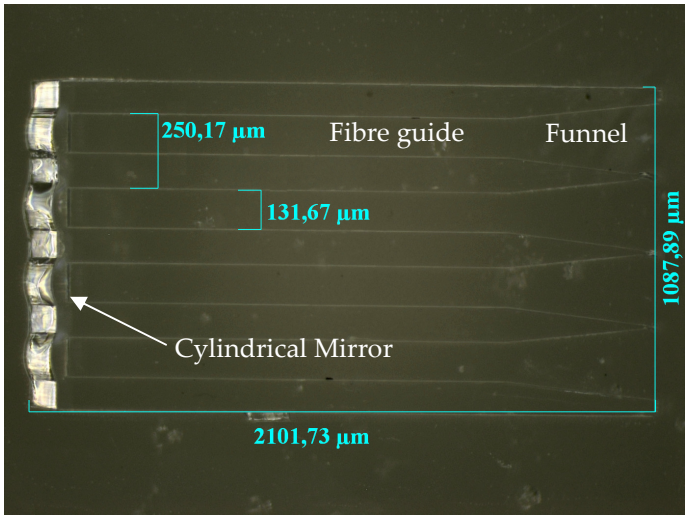

Figure 63. Fabricated multi-channel coupler using photolithography

4.1.2. Fabrication of the Master using Micromachining

Prior to the manufacture of the metal master, some techniques for the fabrication of microstructures were considered. The relevant characteristics, such as resolution of lateral structures, the form accuracy and the obtained surface roughness are compared in Table 9. The chosen method is hard metal milling. It is the most cost-effective method owing to the utilisation of commercial machines and materials for metal processing. In a cooperative project with the Börret Group at the University of Applied Sciences, Aalen, their HSC (High-speed Cutting) machine was characterised and tuned to improve the lateral resolution, and give accuracy to 1 µm.

The fabrication of the coupler using micromachining is also a two-step procedure that begins with the fabrication of the metal mould using an HSC machine. The methodology employed by the manufacture of the mould is based on an analysis of the error tolerances and the limitations of the machine in use, to find a compromise between accuracy requirements and minimised fabrication costs [41].

Since most state-of-the-art standard machine tools are, nowadays, equipped with the same spindles, guide-ways, controls and measuring systems as ultra-precision machine tools, the precision of a machine tool depends mostly on properties such as stiffness, dynamics, spindle eccentricity and inclination, as well as straightness and flatness of the machine table. The precision of the fabricated microstructure can be expressed by the processing uncertainty, which consists of accidental and systematic errors. Accidental errors are caused mainly by external effects such as vibrations, and alternation of load and temperature; i.e. they do not depend on the precision of the machine tool. CAD programming and NC programming must also be considered as possible error sources.

	Ultra precision Diamond Milling	**Hard metal Milling**	Grinding	W/EDM (Electric Discharge M.)	Laser ablation	Electro-chemical milling	LIGA	DMLS
Material	Brass Steel Al Plastics	**Brass Steel Al Plastics**	Tungsten Carbide	Metals Ceramic	Metals Ceramic Graphite	Metals	Ni	Metals
Lateral Structures [µm]	5 - 10	**10 - 1000**		5 - 40	20 – 100	0,25	1	125
Form accuracy [µm]	~0,03	**5 - 10**	0,15	2	nm	nm	nm	>50µm
Surface quality Ra [nm]	~ 10	**> 200**	~ 5	200 - 300	800	~ 5	10	10000

Table 9. Micro-fabrication techniques

Consequently, one step in microfabrication must be to localise accidental errors and try to minimise them. In the next step, the ratio of systematic and accidental errors must be evaluated to decide if the utilisation of an ultra-precision machine tool is necessary. The left column of Table 1 displays accidental processing errors of the machine tool applied to this project; systematic error components are listed on the right., Some error components of second order, dependent on the geometry for cutting, are placed in square brackets. Owing to the relatively simple shape of the microstructure, shown in Figure 64, machine geometry, stiffness, curving dynamics and backlash cause no effects.

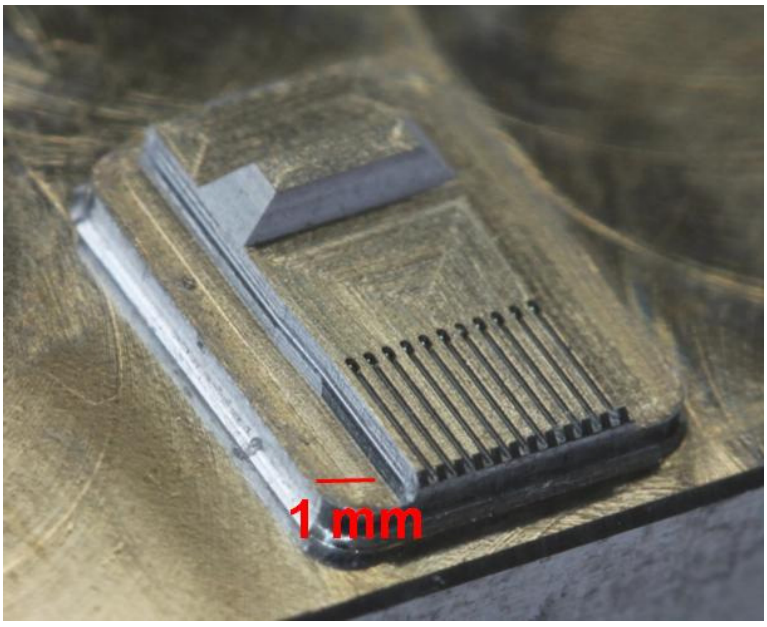

Figure 64. Fabricated metal master for the 12-channel system

Process accidental errors	machine tool systematic errors	software systematic errors
temperature 4 μm	machine tool geometry 0.03 μm	CAD approximation 0.01 %, << 1 μm
cutting tool deflection 3.6 μm	static spindle error (at collet) 1.5 μm	NC-calculation 0.5 %, < 1 μm
tool holder error 8μm	[stiffness]	
[dynamic tool-path error]	calculated run-out 1.5 μm	
Clamping	[backlash]	
	measuring resolution 0.1 μm	

Table 10. Processing errors

After a spindle revision and replacement of its bearings, the static spindle error could be reduced to less than 3 μm. Accidental errors owing to the process were caused mainly by temperature and by clamping after a tool change. An optical supervision system was applied to control the position of the cutting tool at the beginning of a new milling job, after a tool change. Another strategy was to finish the microstructure using one single cutting tool in the final milling job. The run-out could be reduced by the use of a shrinking chunk system. The tool deflection was calculated to less than 3 μm, applying a cutting depth of 5 μm, a cutting width of 6 μm at 24.000 rpm, and a tool diameter of 0.5 mm in the final finishing job. The resulting fabrication error was about 5 μm, at a nominal part size of 250 μm.

The funnel and guiding structures of Figure 64 were designed to receive a 125 μm optical fibre. For this purpose, and taking into account the fibre and fabrication tolerances, the metal mould was designed not have any 90° angle in the guiding structures, as shown in Figure 65. Moreover, the guidance of the fibres is eased, considering that the bare fibres do not have exactly the same diameter.

As shown in Table 9, the surface quality using hard metal milling does not achieve optical quality. For this reason the mirror surfaces must be polished.
The smoothing of the mirror surface was performed using a specially developed computer-controlled polishing process for steel moulds [42], which is able to achieve surface roughness values below 2nm rms, which are specified typically for precision optics. This low-surface roughness value reduces scattering below 0.3% for visible light.

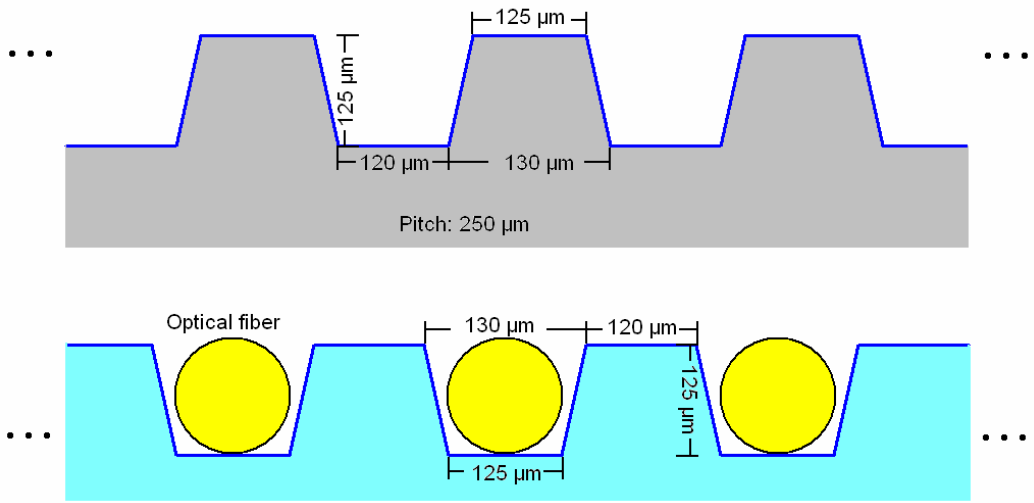

Figure 65. Sketch of the designed fibre guides. Top: dimensions of the metal master. Bottom: replica with the fibres assembled in the coupler.

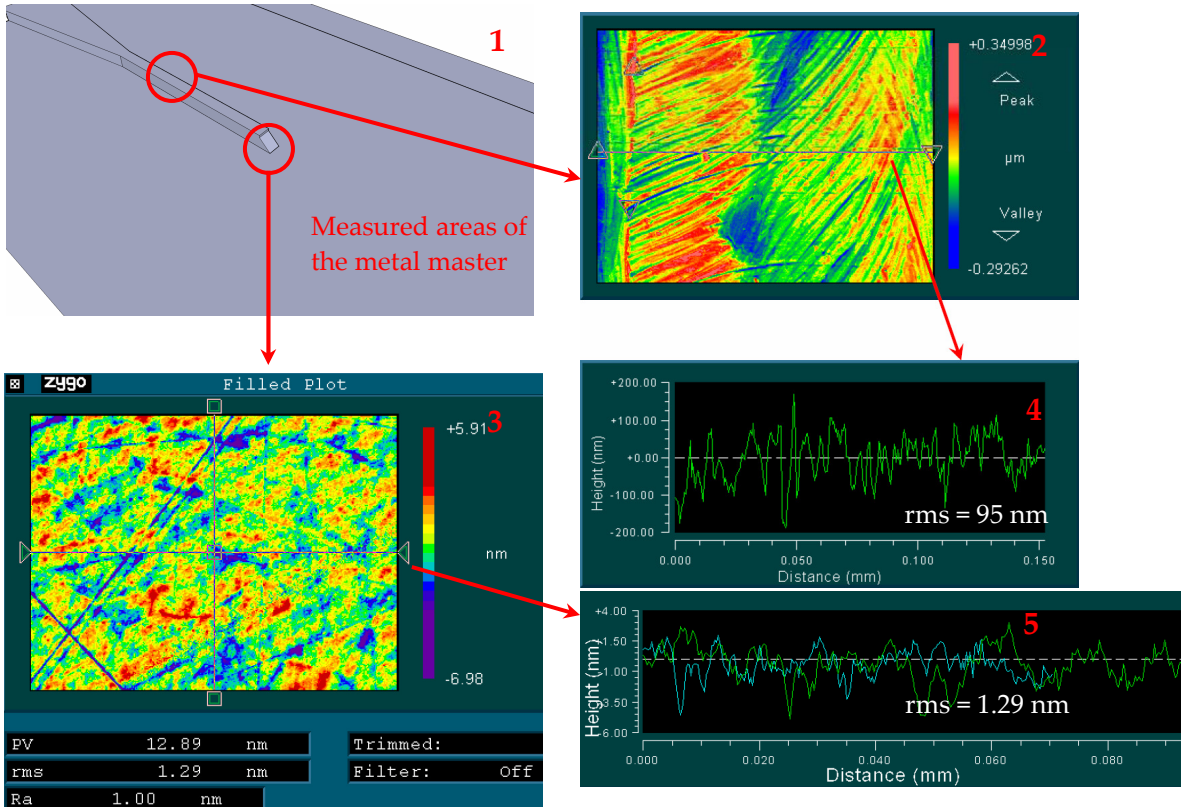

Figure 66. Quality of the surfaces. Comparison of the roughness on polished and unpolished surfaces. (Measurements by HS-Aalen)

In Figure 66 measurements on different areas of the metal master are shown: in the graphic with the label 1, the measured areas are encircled. For comparison of the roughness with- and without polishing, the surface of the master's funnel and the surface of the mirrors were measured. The graphics with the labels 2 and 4 show the

2D and 1D representation of the measurement corresponding to the non polished surface. The graphics with the label 3 and 5, show the measurements of the polished surface, that corresponds to the mirror's surface in the plastic replica.
The single channel master was fabricated from steel. The mirror's surface was polished using diamond polishing mounted in a robot arm. With this method, a very low roughness can be achieved but the process is extremely slow and requires a high programming effort.

4.1.3. Replication of Masters with Plastic Polymers

The replication of the mould is a one- or two-step process, depending on whether the mould has the negative shape of the coupler or not.

The mould fabricated lithographically has the positive shape of the coupler so that the mould must be replicated twice to obtain the actual coupler. In this case, the mould is first replicated using a Polydimethylsiloxane (PDMS) polymer, to obtain a replica of the master with the negative shape of the coupler. The advantages of using PDMS are: the low viscosity of the polymer at low temperatures, so that microstructures can be reproduced accurately; the material is transparent, so that the structure can be replicated using UV-hardening polymers; and it is easily separable from glass or plastic substrates. Once the master is replicated in PDMS, the process continues, as explained in the following for the replication of the metal master.
The replication of the mould with the negative shape of the optical coupler is performed using a UV-curable polymer [43]. The NOA-61 from Norland Adhesives has a very low viscosity; important for the ability of the polymer to replicate nanostructures. To have an idea of the NOA-61 viscosity, 300 mPas, it can be compared to that of water, 1 mPas, and honey, 10,000 mPas. The spectral transmittance of the utilised polymer is shown in Figure 67, for perpendicular incidence on the surface of the polymer.

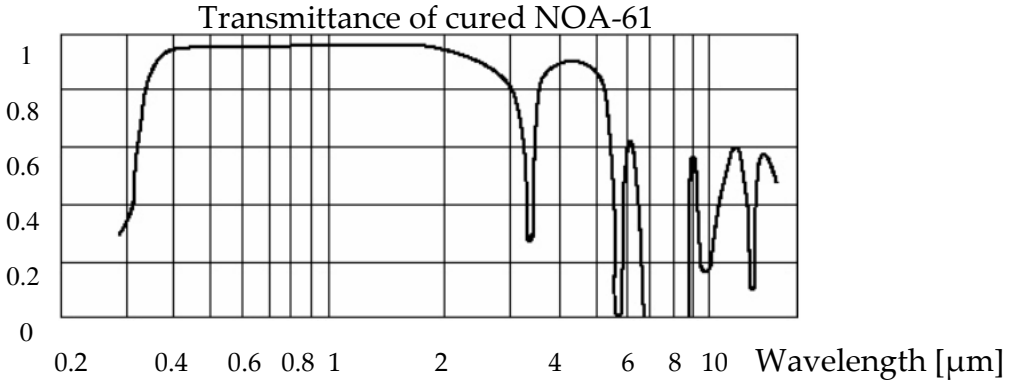

Figure 67. Spectral transmittance of the used UV-curable polymer, NOA-61. (Image taken from the datasheet information provided by Norland Adhesives)

From the graphic, the transmittance by perpendicular incidence at 850 nm is about 96%. The transmittance is given for any incidence angle by:

$$\mathrm{T} = |t_s|^2 \frac{n_t \cos \vartheta_t}{n_e \cos \vartheta_e} \tag{4.1}$$

where n_t=1.51 is the refractive index of the cured polymer for 850nm, n_e is the refractive index of the air, ϑ_e is the angle of incidence of the beam that propagates in air, ϑ_t is the angle of the transmitted beam in the polymer, and t_s is the transmission coefficient for s-polarisation given by:

$$t_s = \frac{2 n_e \cos \vartheta_e}{n_e \cos \vartheta_e + n_t \cos \vartheta_t} \tag{4.2}$$

Here, the wave is assumed to be s-polarised [45]. Only for holographic applications the geometry of a VCSEL is intentionally modified in order to polarise the wave other than perpendicular.

For perpendicular incidence is the transmission coefficient t_s=0.79 and the transmittance T=0.96, as shown in Figure 67.

Correspondingly, the reflectance and the reflection coefficient are:

$$\mathrm{P} = |r_s|^2 \tag{4.3}$$

$$r_s = \frac{n_e \cos \vartheta_e - n_t \cos \vartheta_t}{n_e \cos \vartheta_e + n_t \cos \vartheta_t} \tag{4.4}$$

For an incidence angle of 45° the transmittance and reflectance are T=0.9 P=0.1 Evidently, the reflectance of the surface is too low to guarantee a high coupling efficiency, if using the bare polymer for the mirror in the purposed coupling system. In order to increase the reflectivity of the surface it has to be coated with a reflecting material.

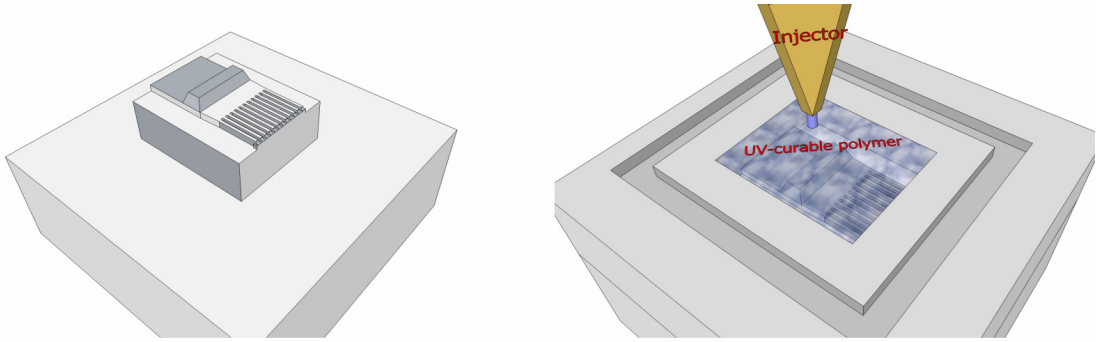

Metal master with the negative shape of the optical

Injection of the liquid polymer over the master

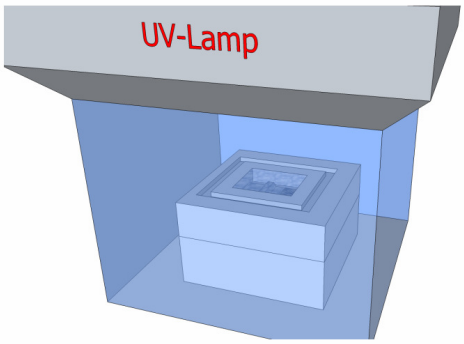

Curing of the polymer under UV-radiation

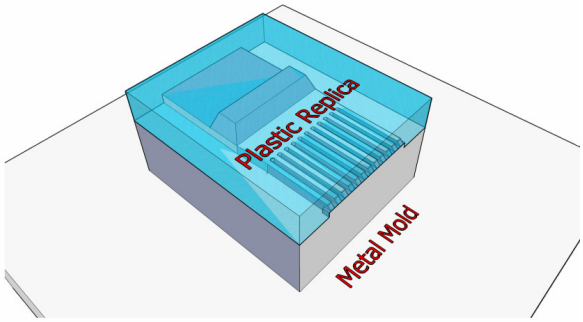

Cured replica and master before separation

Figure 68. Fabrication of the optical coupler using replication of a negative master

The mirror surfaces must be metallic coated

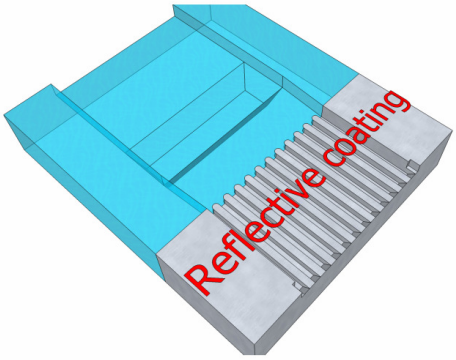

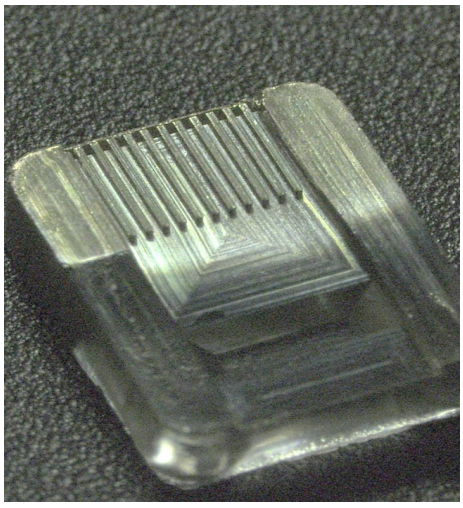

Figure 69. Reflective coating of the mirrors' surface. Sketch and manufactured coupler

Continuing with the fabrication of the optical coupler, first the mould is filled up with the polymer in liquid form, and afterwards cured with UV radiation. Finally, the mould and the replica are separated. The surface of the replicated mirror is sputtered with a metallic coating. The complete process is show in Figure 68. The replication with a metal mould ensures the optical quality of the mould in the plastic substrate, making it a very accurate fabrication method, which is also attractive because of its low cost.

The reflective coating is achieved by sputtering a 100nm silver layer on the surface of the mirrors. The sputtering process is a technique used to deposit thin films of a material onto a surface. By first creating a gaseous plasma, and then accelerating the ions from this plasma into the target, the source material is eroded by the arriving ions via energy transfer, and is ejected in the form of neutral particles; either individual atoms, clusters of atoms or molecules. As these neutral particles are ejected they will travel in a straight line, unless they come into contact with something; for example, other particles or a nearby surface. If a substrate such as a glass plate or the optical coupler is placed in the path of these ejected particles, it will be coated by a thin film of the source material.

Silver coatings oxidate [44]. as a result of the oxidation the reflectance of the coating degrades. In twelve months, under ambient conditions of temperature and humidity, the reflectance of a silver coating can decrease by up to 50% of the initial value. A comparison of the reflectance of different metal coatings is shown in Figure 70.

Gold shows a better reflectance than silver at 850 nm. On the other hand, the silver adherence on plastic surfaces is much better than gold. Moreover, the material costs could be a deciding factor if the process is run industrially.

In order to protect the silver coating against corrosion as result of metallic oxidation, the metallised surface is coated with an additional 10 nm transparent coating that has glass-like optical properties. This type of coating is part of an as yet unpublished work at the Fraunhofer Institute for Solar Energy Systems.

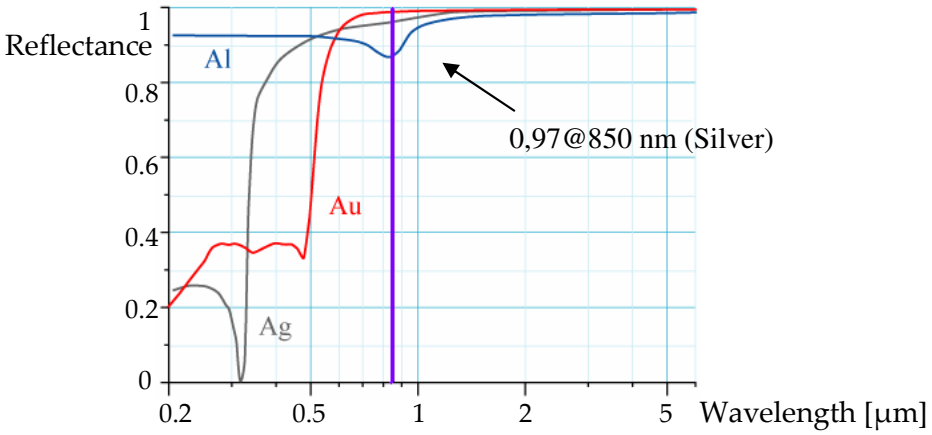

Figure 70. Spectral reflectance of some metallic coatings. (Image from Wikipedia)

4.1.4. Measurements

In order to compare the quality of the obtained surfaces, after the replication of the masters fabricated lithographically and using micromachining, the reflected images were compared qualitatively using the set-up shown in Figure 72.

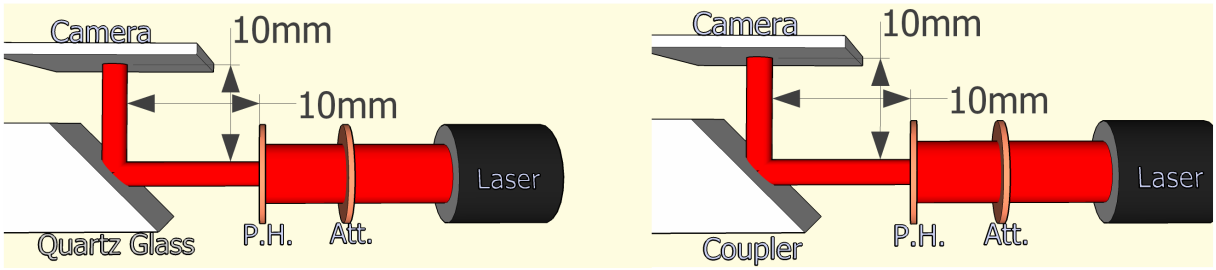

Figure 71. Sketch of the set-up shown in Figure 72

The characteristics of the used optical devices are listed below:

- 10 mW He-Ne Laser (λ=632nm)
- Attenuator 1 (T=1%)
- Attenuator 2 (T=0.1%)
- 100 μm Pinhole
- CCD Camera (Pixel size: 11 μm x 11 μm)

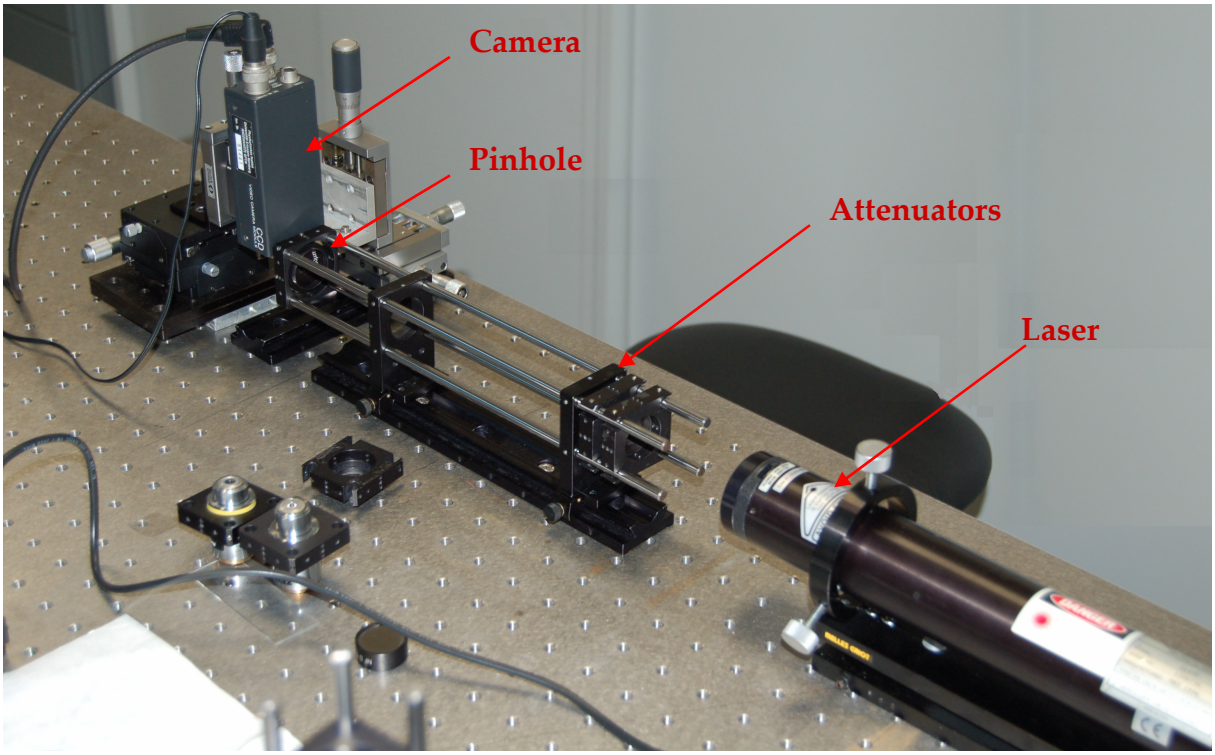

Figure 72. Set-up used for the comparison of the mirror surfaces. The surface of a quartz glass used as reference

The intensity distributions, obtained after reflection of the beam at the quartz glass and at the mirror surface without silver coating, is shown in the Figure 73.

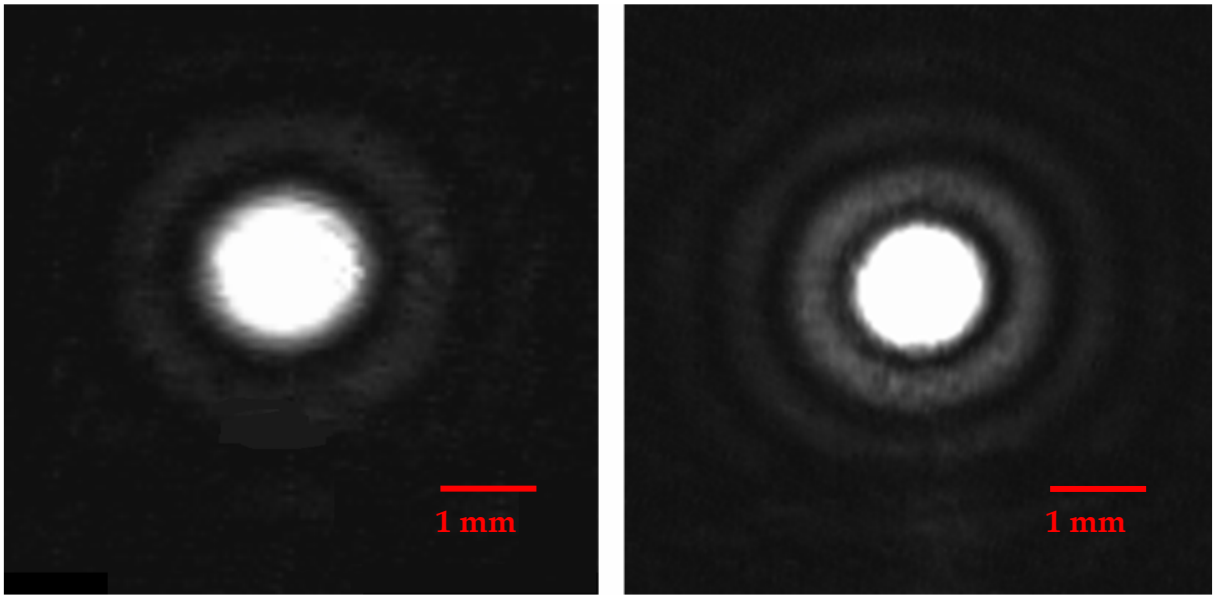

Figure 73. Intensity distributions of the reflected beams by quartz glass (left) and replication of polished metal master (right)

From the qualitative observation of the intensity distributions follows that the surfaces are comparable. There is not distortion of the form of the beam and the difference in the granularity of the images indicates some difference in the roughness of the reflecting surfaces. The signals in Figure 73 seem to be overdriven as graphic effect. In the further analysis, these distributions will be evaluated numerically. In the Figure 74 the simulated intensity distribution is shown. The simulations were made with the simulation tool described in chapter 3.

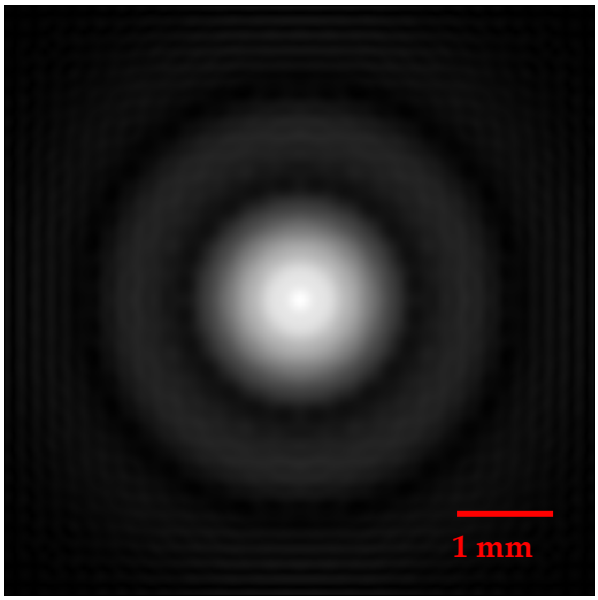

Figure 74. Simulated intensity distribution of the reflected beam for a perfect mirror

The distribution of the beam reflected by the coupler, replicated from the master fabricated lithographically (see Figure 62), is shown in Figure 75. The striation on the master is a result of the combination of non-uniform response of the SU-8 to the UV radiation, and the non-uniform intensity distribution of the UV lamp [35].

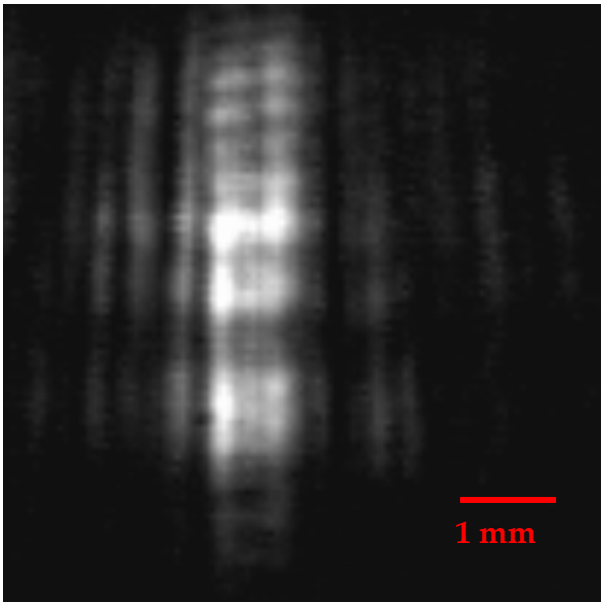

Figure 75. Intensity distribution of the coupler replicated from the master fabricated lithographically. (Same scale used as in Figure 73)

4.1.4.1. Analysis of the Intensity Distributions

Figure 76 shows the intensity distributions of the plastic replications of unpolished and polished metal masters.

The curves shown at the bottom of the figure represent the addition in the x and y direction of the 2D distributions shown at the top of the figure. The obtained 1D distributions were normalised by the maximum of the 1D distribution, obtained from the reflection on quartz glass.

There is a clear difference between the 1D distributions in the x and y direction of the unpolished surface. The distribution in the y direction is wider than in the x direction. This is owing to the manufacturing process. The direction of travel of the hard metal spindle is the x axis, which produces grooves in the direction of travel. These grooves scatter the reflected light in the y direction. These defects are corrected by polishing, and the distributions are very similar in both directions.

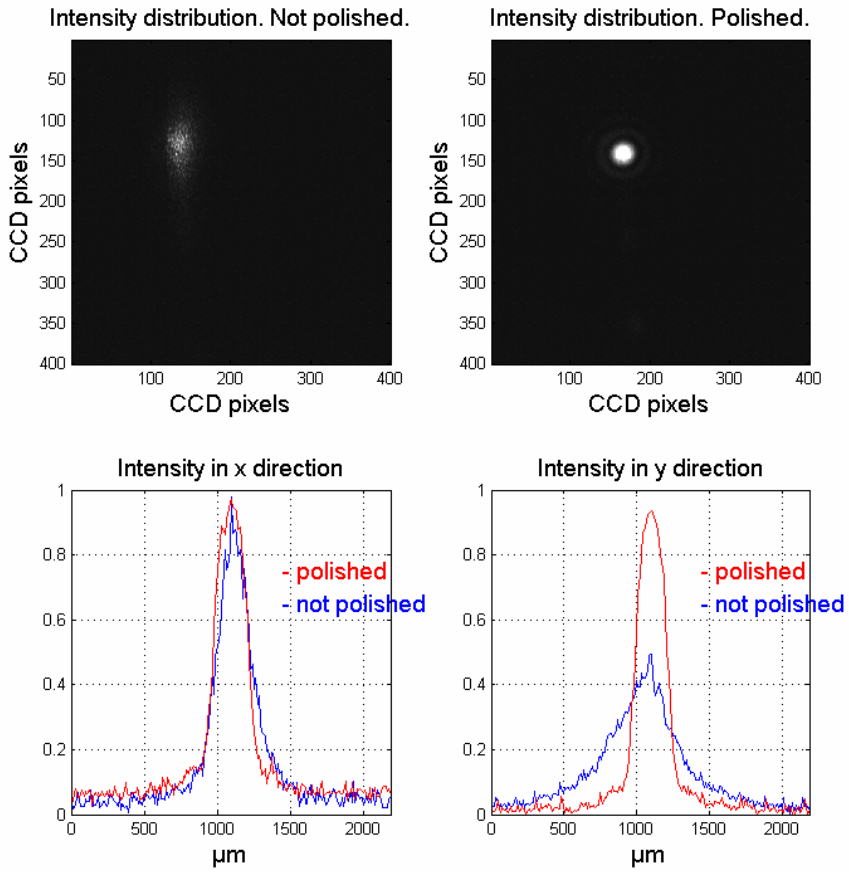

Figure 76. Intensity distributions of the reflected beam by a replication of a not polished (left) and a polished metallic master (right)

The micromirrors were observed under a microscope using two different illuminations to ease the observation. In Figure 77, a zoomed picture of the plastic replica of the unpolished metal master is shown. The grooves in the x direction, caused by the hard metal spindle, can be seen. The polished mirrors are shown in Figure 78.

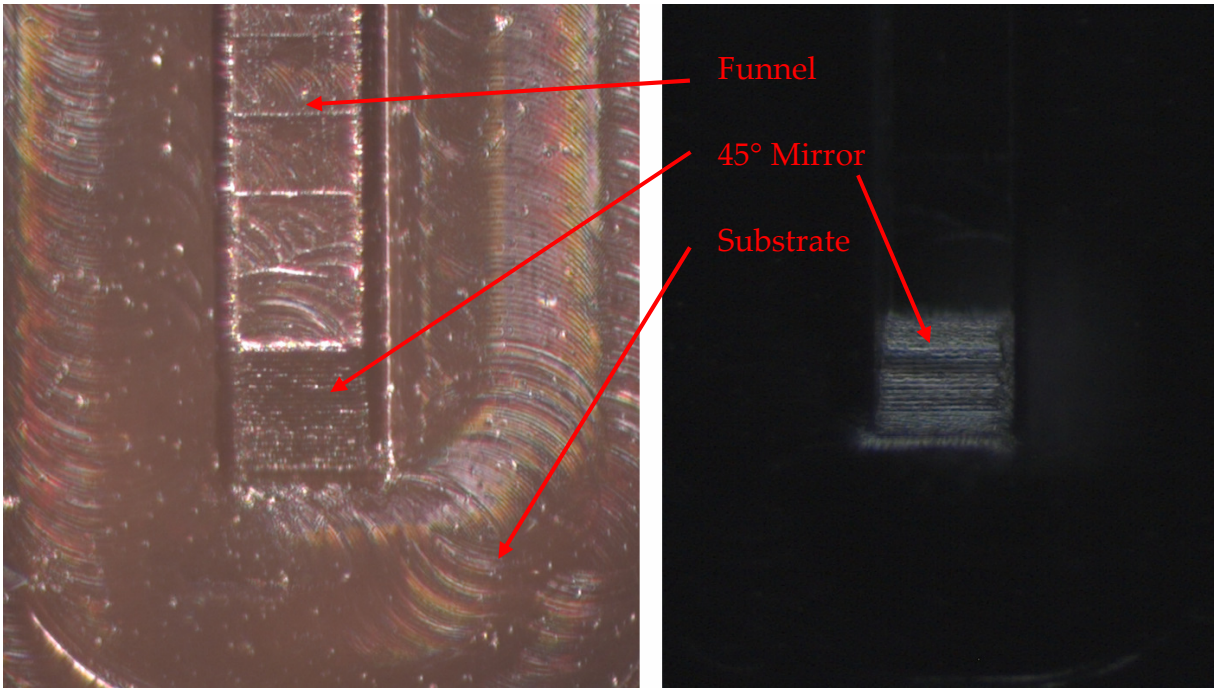

Figure 77, Unpolished micromirror observed with two different illuminations

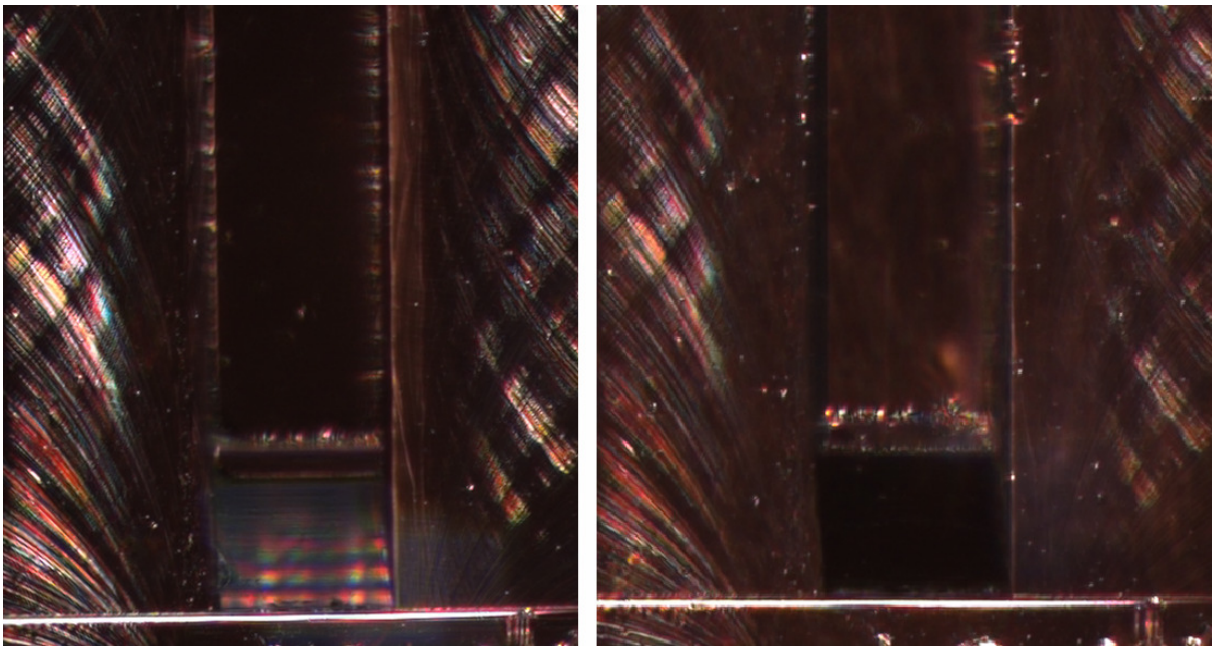

Figure 78. Polished micromirror observed with two different illuminations

4.1.4.2. Measurement of the Mirrors using a White Light Interferometer (Pictures from HS-Aalen)

Measurement with white light interferometer 'Zygo New View 200' in HS-Aalen:

- white light mode

- 20x Mireaux-Objective, 2x optical Zoom, System Zoom 40x
- Scan length 40µm
- FOV 0.15mm x 0.11mm

The results of the measurement of one of the mirrors are shown in Figure 79.

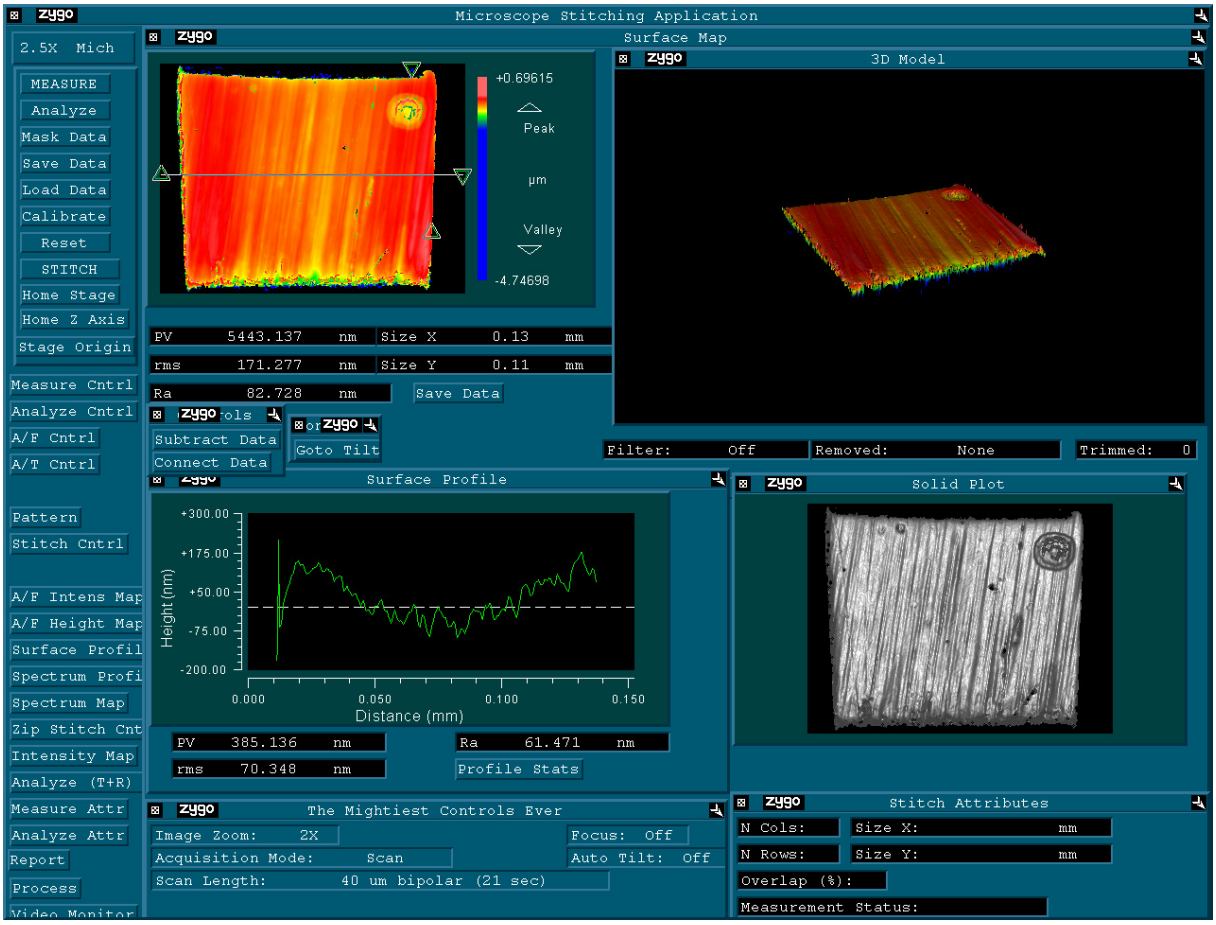

Figure 79. White light interferometer measurement of one of the mirrors in the multi-channel system

Mirror Nr.	1	2	3	4	5	6	7	8	9	10	11	12
RMS roughness [nm]	94	70	82	107	93	101	72	82	83	85	76	86

Table 11. Roughness of 12 micromirrors. RMS values

The multi-channel master was also fabricated from steel but the polishing method was changed. The mirrors' surfaces were polished using diamond polishing paper with a hand operated mechanical setup, in which the polishing paper is moved parallel to a defined plane.

4.1.5. Coupling efficiency

The coupling efficiency was measured by comparing the power of the reflected beam from the mirrors to the output power of a pigtailed 850 nm laser, with the set-up shown in Figure 80. The laser is pigtailed to a multimode fibre whose core has a diameter of 125 μm: the funnels' width in the optical coupler.

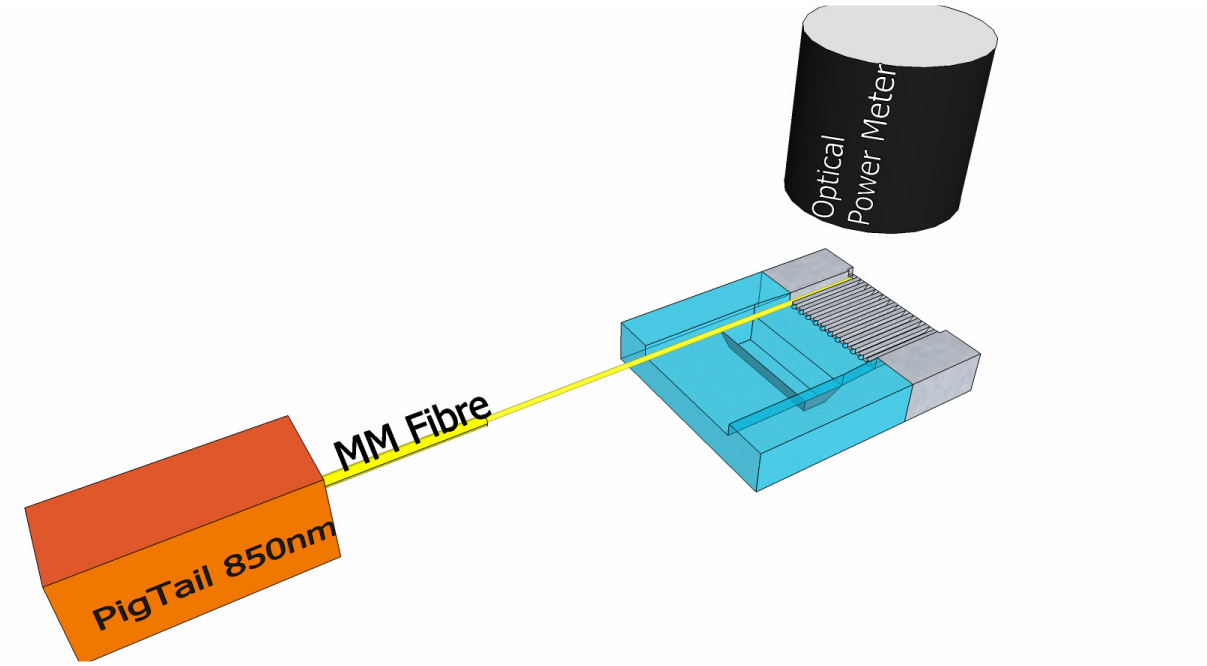

Figure 80. Set-up for the measurement of the coupled power

The procedure was repeated for the 12 mirrors and the results are shown in the Table 12.

Mirror Nr.	1	2	3	4	5	6	7	8	9	10	11	12
Coupling efficiency [%]	85	85	84	84	83	82	80	78	77	75	74	72

Table 12. Coupling efficiency of the 12-channel coupler

The differences between the expected efficiency of about 90% and the measurements result from two factors: first, the distance from the micromirror to the detector is about 10 mm; and second, the form of the mirrors is not planar, as expected.

With regard to the first factor, the sensitivity of the detector used in the optical power meter is not constant over the whole sensing surface. It was found that the efficiency of the optical power meter drops with the radius.

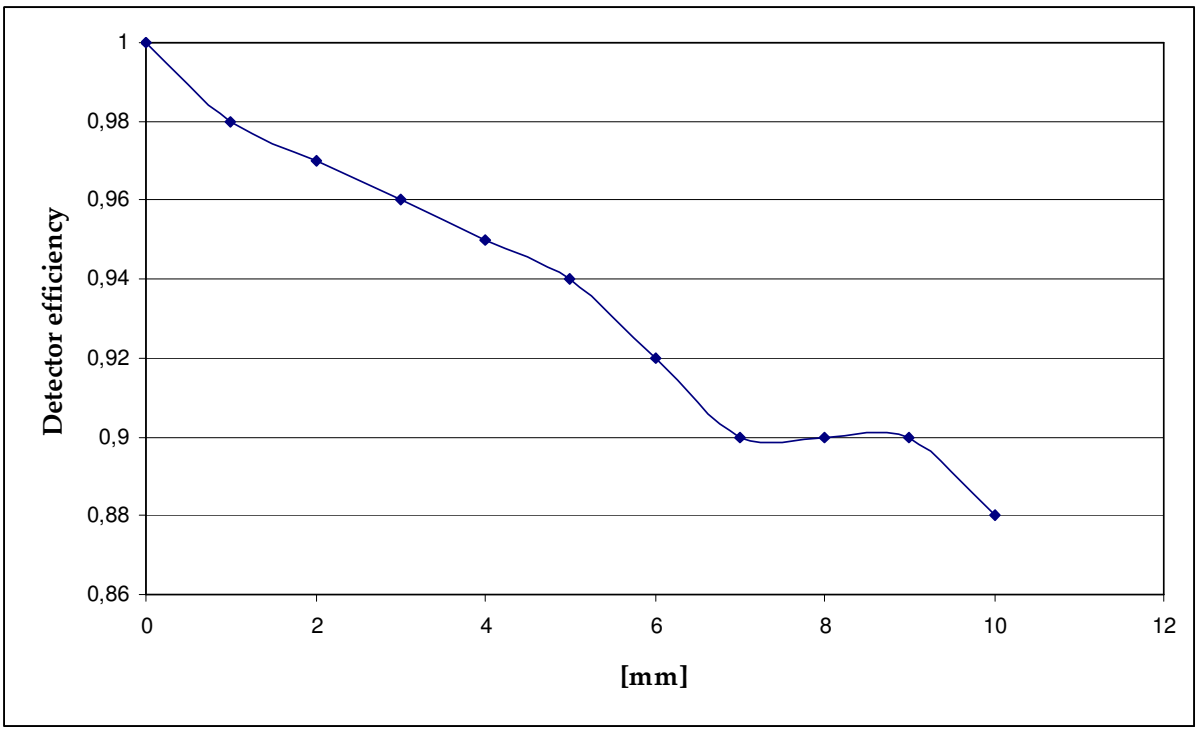

Figure 81. Dependence of detector's efficiency on the detector's radius. Normalised to the maximum at the centre of the detector

Regarding the second factor, the surface of the mirrors was observed under a microscope and an imperfection was found: the mirrors' surface is not completely planar. Figure 82 shows the effect of an error in the polishing process.

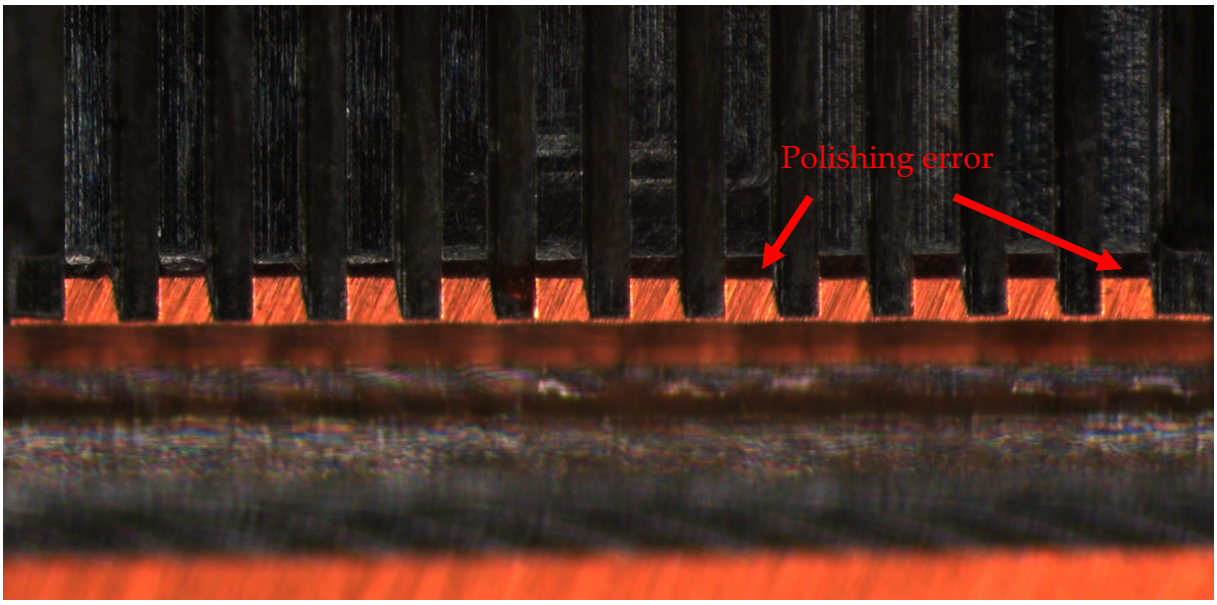

Figure 82. Surface of the 12 mirrors on the metal master

The non planarity of the surfaces causes the reduced coupling efficiency.

4.2 Assembly and Adjustment Set-up

The assembly of the system is based on a modular construction that allows the independent testing of both the electronic and the optical systems. For the transmission of the electrical signal, transmission lines and high-speed connectors are needed. The electrical signals are converted into optical signals by the VCSEL, which is driven by a specific circuit that sets parameters for the correct function of the VCSEL. A sketch of the electronic system and the markers is shown in Figure 83.

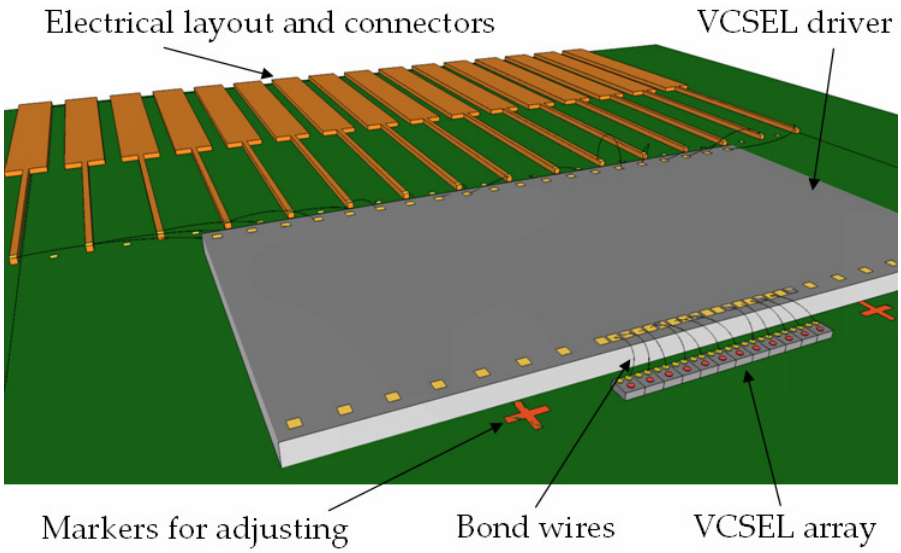

Figure 83. Electronic system for the send side

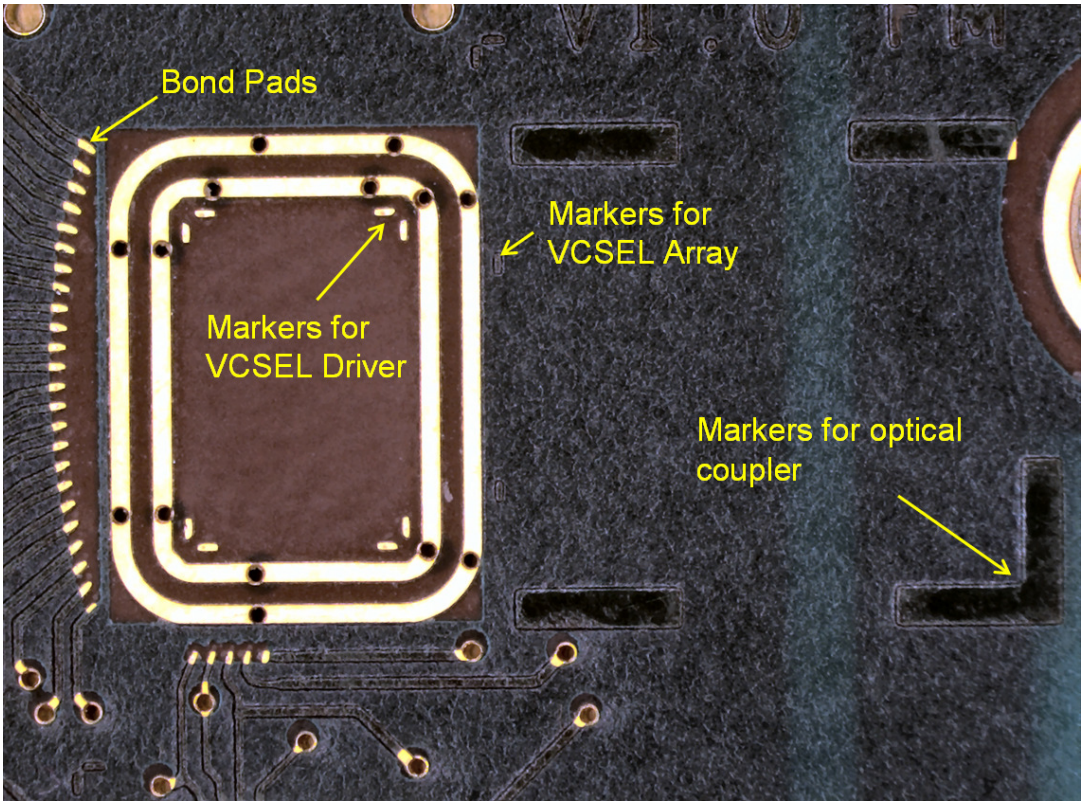

Figure 84. Markers on the PCB used for the passive alignment

The optical system comprehends the optical coupler and the optical fibres (see Figure 85).

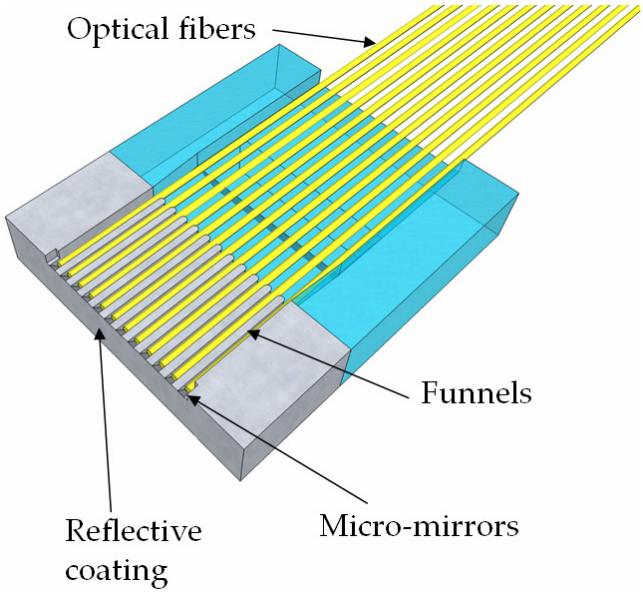

Figure 85. Optical system

The optical fibres are guided by the funnels to the mirrors by means of a micrometric screw-based system that has five degrees of freedom: the position along the three Cartesian coordinates is variable with an accuracy of 10μm, and the tilt angle around the x and z axis can be varied with an accuracy of 0.2° (see Figure 87).

This accuracy is important for the adjustment of the devices. The assembly is controlled under a microscope and, in this way, the contact of the fibres with the mirrors' surface is avoided. Figure 86 reveals a zoomed picture of the system.

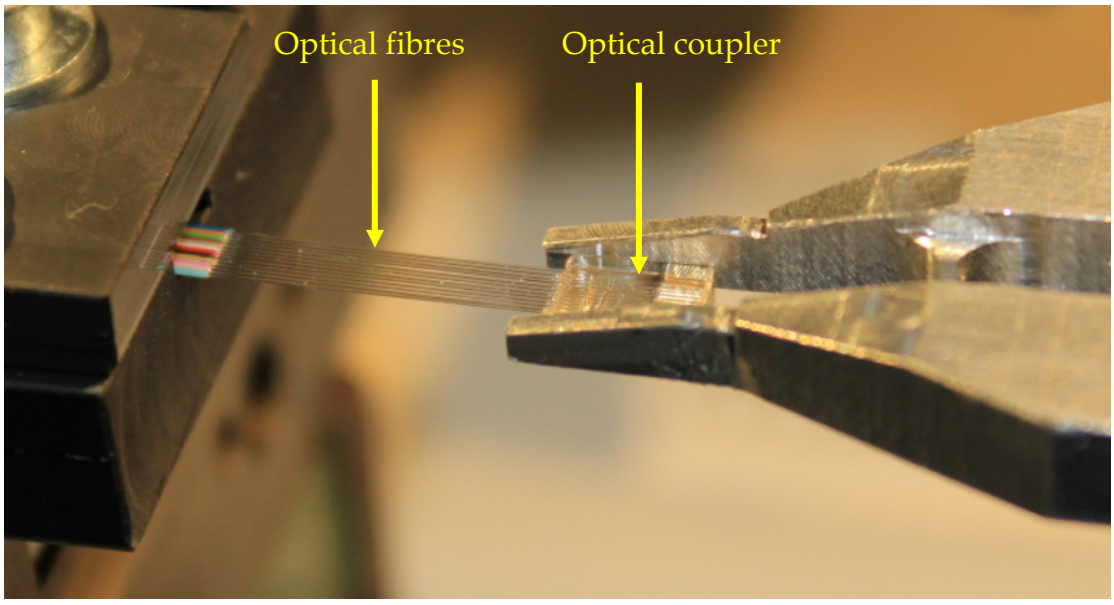

Figure 86. Assembly of the optical system

In Figure 88 the mechanical system is shown. On the left-hand side, the holder for the PCB can be replaced by the holder for the fibre ribbon. On the right-hand side, the holder for the optical coupler has the aforementioned five degrees of freedom. The accuracy of the mechanical systems is needed to guarantee a high coupling efficiency.

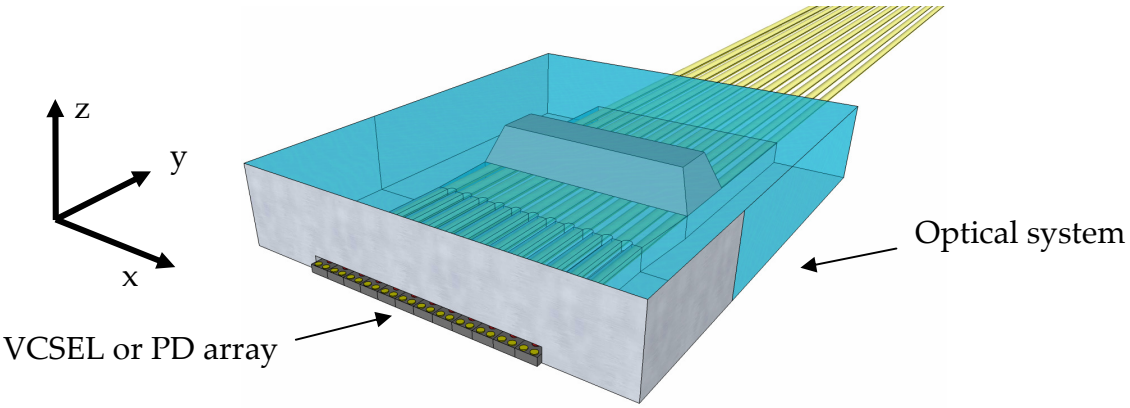

Figure 87. Adjustment of optical system and the VCSEL, or photodiode array

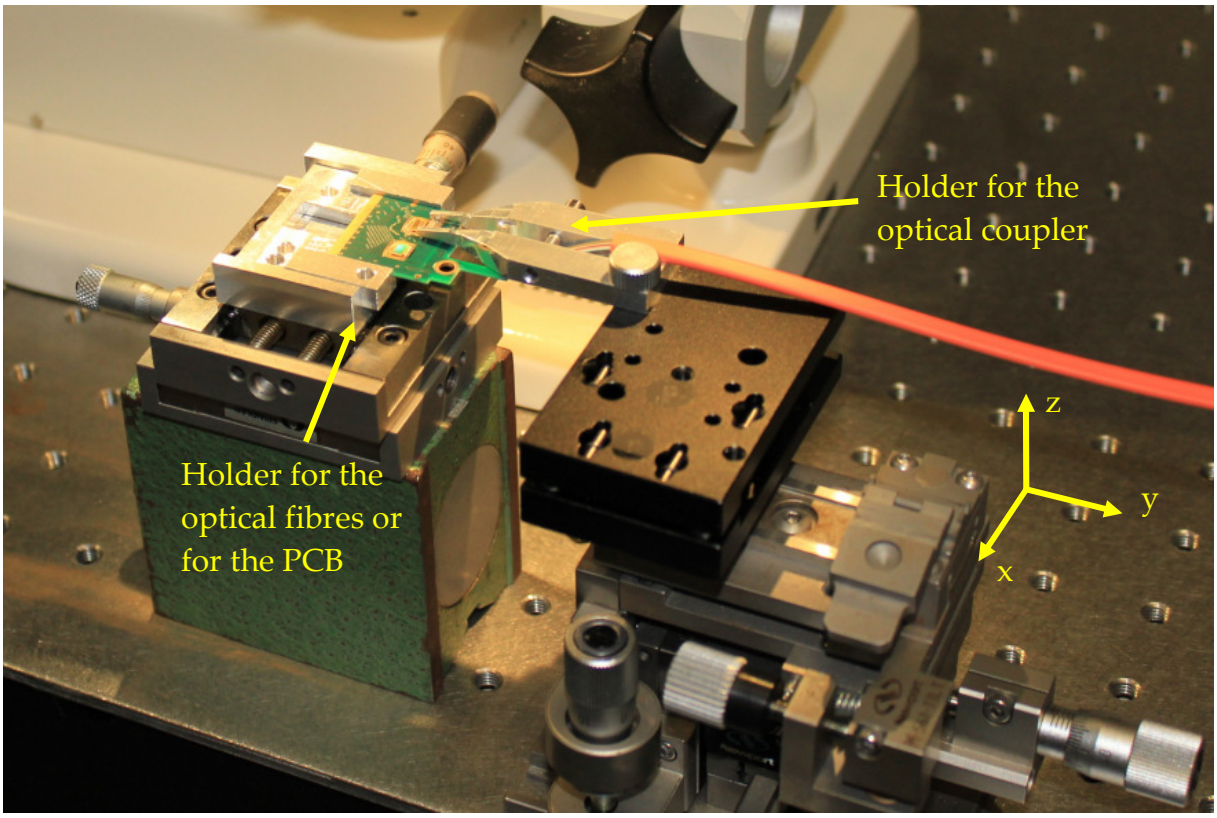

Figure 88. Mechanical system used for the assembly of the optical subsystems, and the integration of the optical- and electronic modules

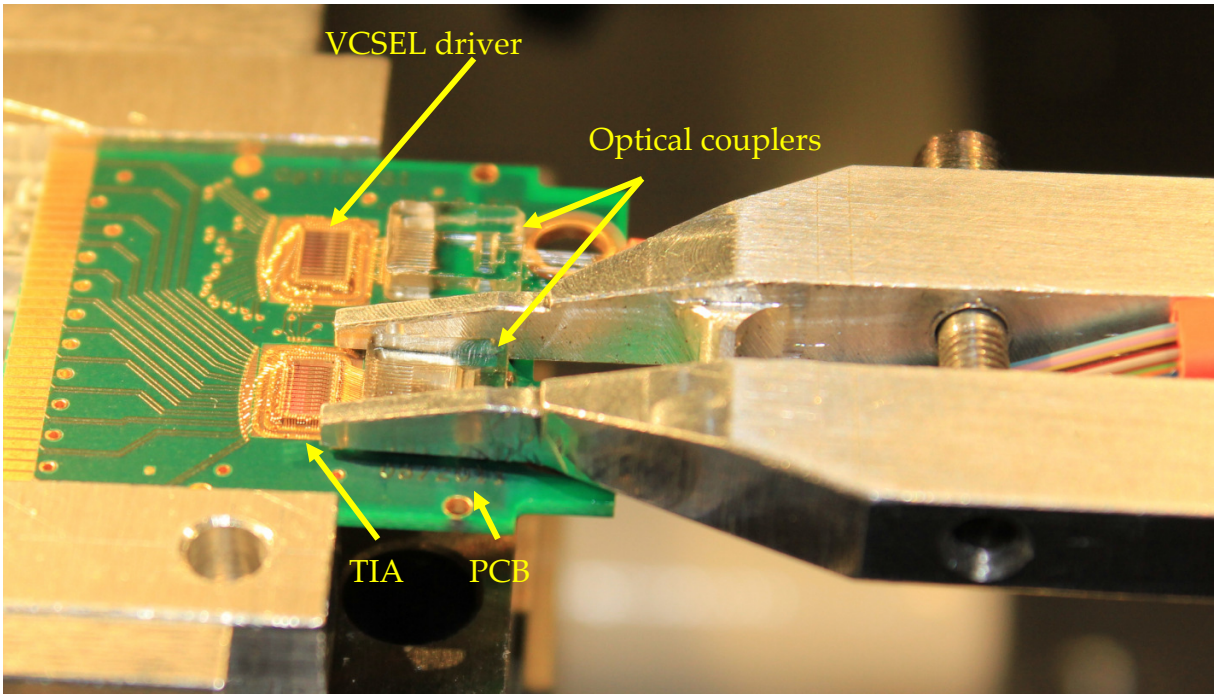

Figure 89. Zoomed image of the adjustment process

4.2.1. Passive Alignment

The alignment of the electronic and the optical systems can be done in a two-step procedure. First, a passive alignment based on markers is done with the presented mechanical systems.

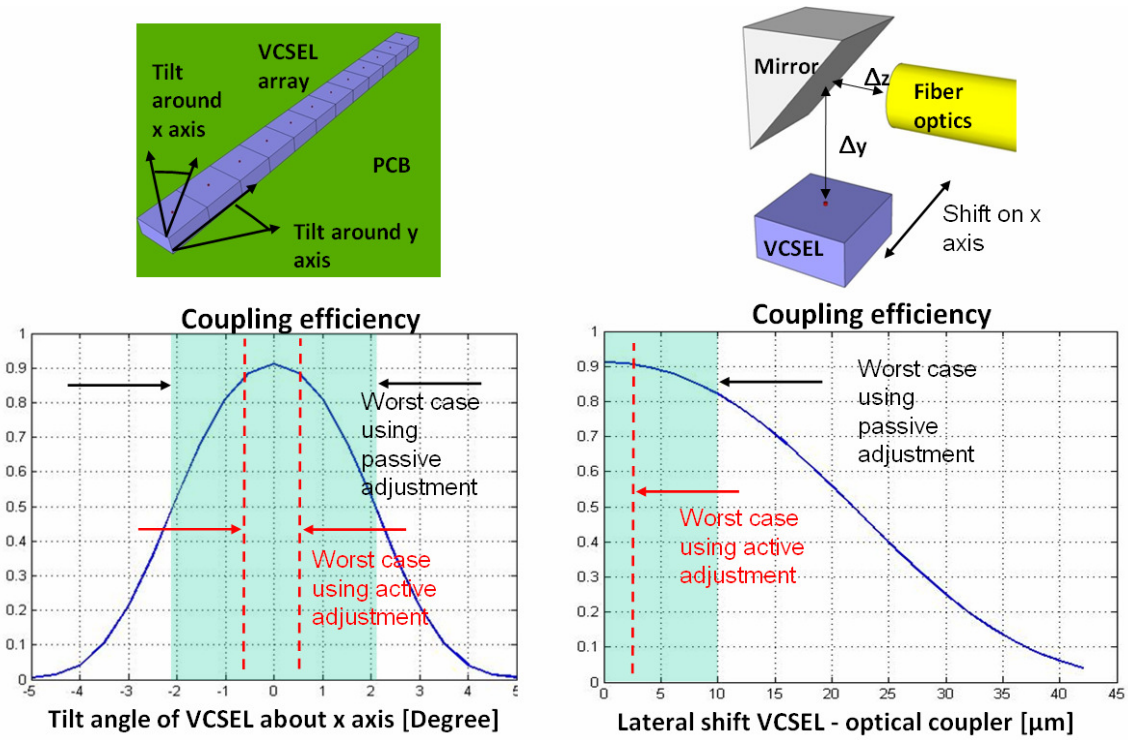

Figure 90. Passive and active adjustment

The accuracy of the mechanical adjusting systems is within the tolerances calculated in Section 4.2.3. The results are presented again in Figure 90, with the acceptable tolerances for a worst case of 50% of the possible maximum coupling efficiency. An important aspect to take into account is the ability of the PCB assembly systems to place the optoelectronic devices on the PCB plane, without tilt angles. In order to control the tilt angles in a total of eight assembled PCBs, the height of diverse points on the devices were measured. The height difference between PCB and adjacent points on the chips were as shown on the right-hand side of Figure 91.

The maximum measured height difference was 10μm, hence the maximum measured tilt angle was $\theta = 2.3° = \arcsin\left(10/250\right)$.

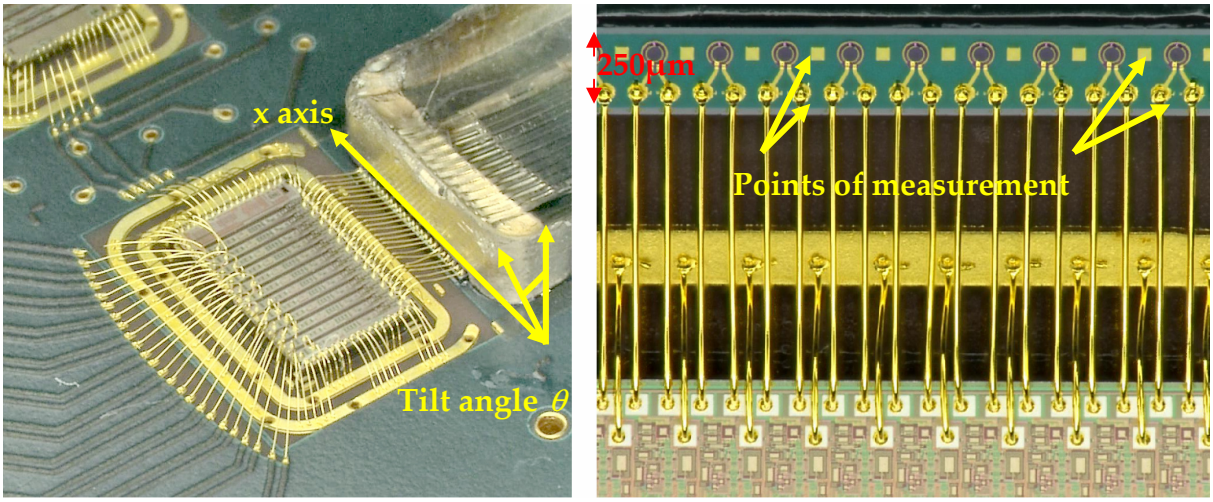

Figure 91. Measurement of tilt angles

There is a possible second step for the fine adjustment of the systems: the active alignment.

4.2.2. Active Alignment

If the coupling efficiency is not satisfactory after passive alignment, there is the possibility of fine tuning by monitoring the signal amplitude while adjusting the position dynamically. Figure 92 demonstrates the signal path. The green boxes represent the electronic and optoelectronic devices, while the blue boxes represent the optical devices. The electrical signals can be measured directly at the high-speed connector while, for the measurement of the optical signals, additional tools had to be manufactured.

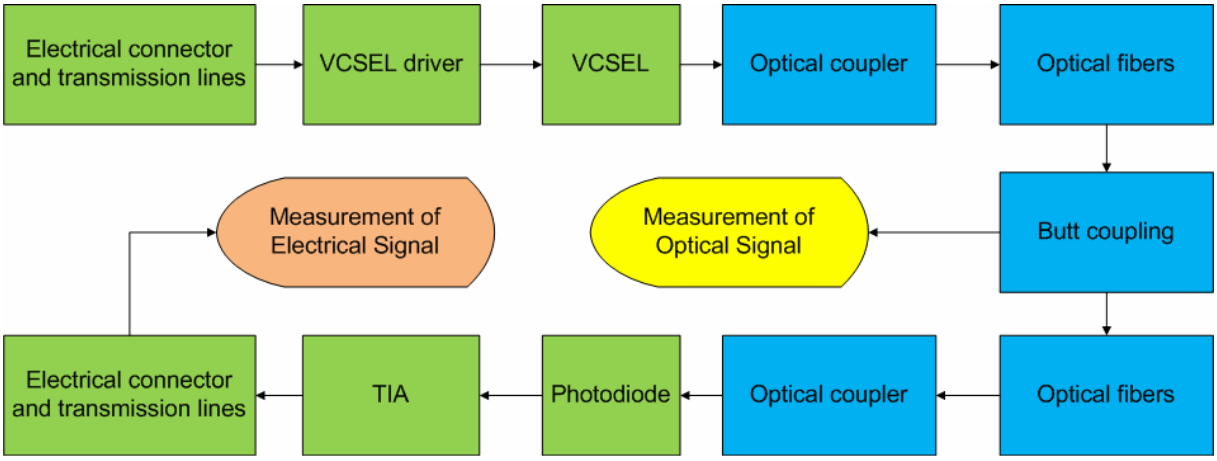

Figure 92. Block diagram of the system and measurement points for the active alignment

For the measurement of the optical signal, the optical fibre has to be cut and, after the measurement, the fibres are spliced with commercial equipment.

The optical signals have to be coupled with a fibre that is connected to the sensor of the oscilloscope using a butt coupling.

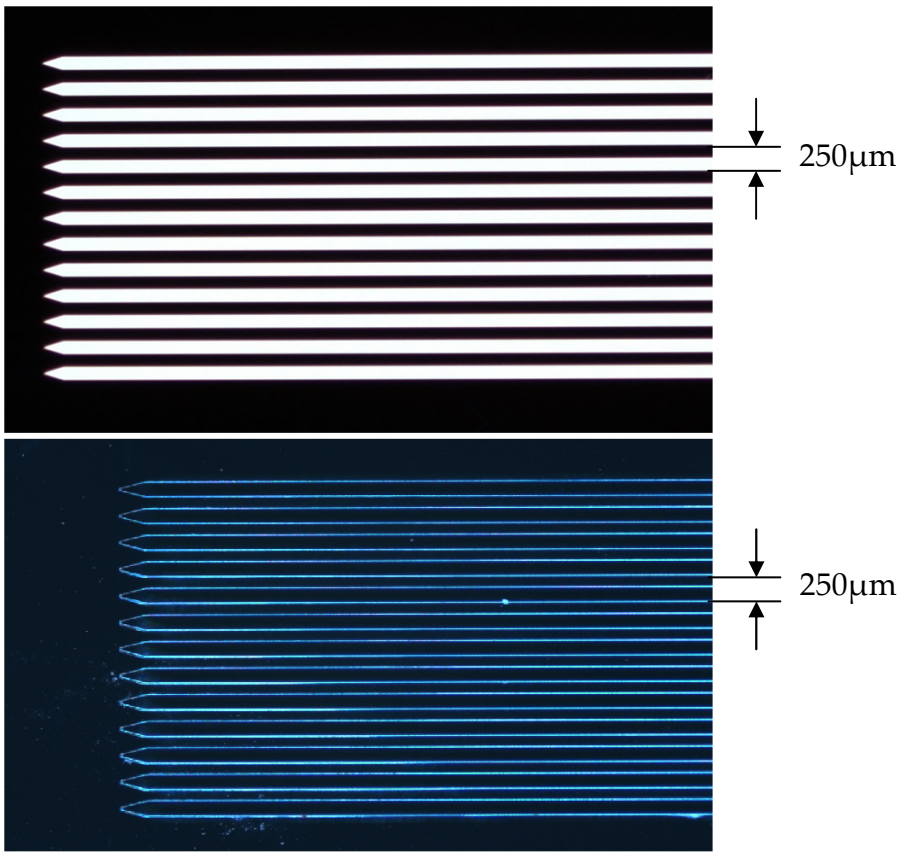

Figure 93. Mask (top) and coupler (bottom) manufactured for the butt coupling

This coupler was fabricated using a SU-8 process. It starts with the fabrication of a chrome mask, by using laser lithography. A SU-8 substrate is exposed to UV radiation under the mask to obtain the desired structures (see Figure 93) [48].

The butt coupling is shown in Figure 94, where the fibres were separated intentionally for visualisation purposes.

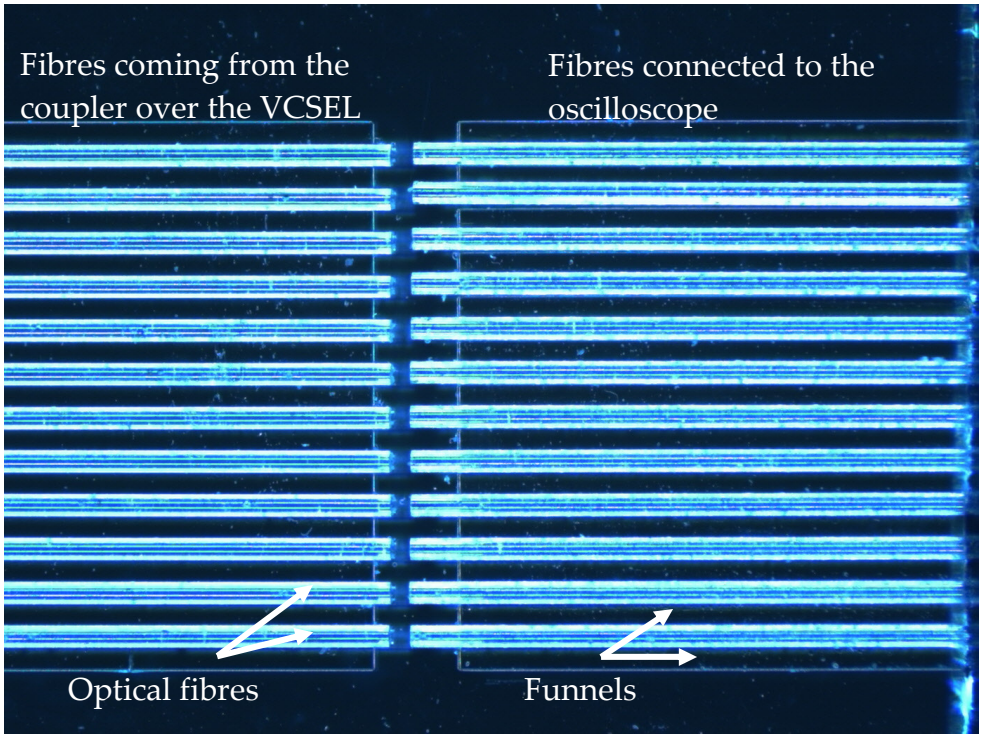

Figure 94. Butt coupling

This method achieves coupling efficiencies of about 50% in the complete communication system, what is needed mainly when the length of the optical fibres is larger than 100m.

4.3 Conclusions

- The fabrication of optical couplers using plastic replication of masters is a reliable, cost effective method for the manufacturing of optical devices. The possibility to automate the process was taken into account in the design and therefore several mechanical devices were included in the construction.
- Metal masters have the following attractive properties:
    - They can be manufactured with high precision. Structures of some micrometers are achievable with modern techniques like diamond milling or high speed cutting micromachining.
    - Optical surfaces can be polished to reach a roughness of some nanometres.
    - Metals can be replicated almost infinitely without changing their properties.
    - Material costs are almost negligible while the tools for the manufacture of the masters represent a high cost, with the advantage that it has to be paid only once.

- The modular construction of the integration system eases the test and verification of each of the components or subsystems, in that way the risk of malfunction is minimised.
- In order to achieve higher coupling efficiencies, the possibility of an active alignment was studied and a solution was proposed, based on the cut of the optical fibre for the measurement of the optical signal and afterwards the use of butt coupling in the cut fibres.

5. Optoelectronic systems for application of the optical coupler

In the previous chapters the attention was focused on the optical and optoelectronic systems. In chapter 4, the integration of the devices on a small PCB was presented. This chapter concentrates on the applications; that is, possible implementations in order to supply actual necessities.

5.1. Real time video-processing and transmission

In the first part, the block diagram of the systems is explained. The architecture for the single- and the multi-channel systems is the same. The single-channel system was made before the multi-channel system, and proves the principle of the send side of an optical-fibre communication system, based on the intended coupling concept. It is as simple as an electronic circuit that drives a single VCSEL and the measurement of the optical signal, after being coupled into an optical fibre. The multi-channel system consists of the parallelisation of twelve single channels, in which the optical and optoelectronic devices are placed on a small PCB, and the circuitry concerning a specific application is placed in a separate board.

5.1.1. Block diagram

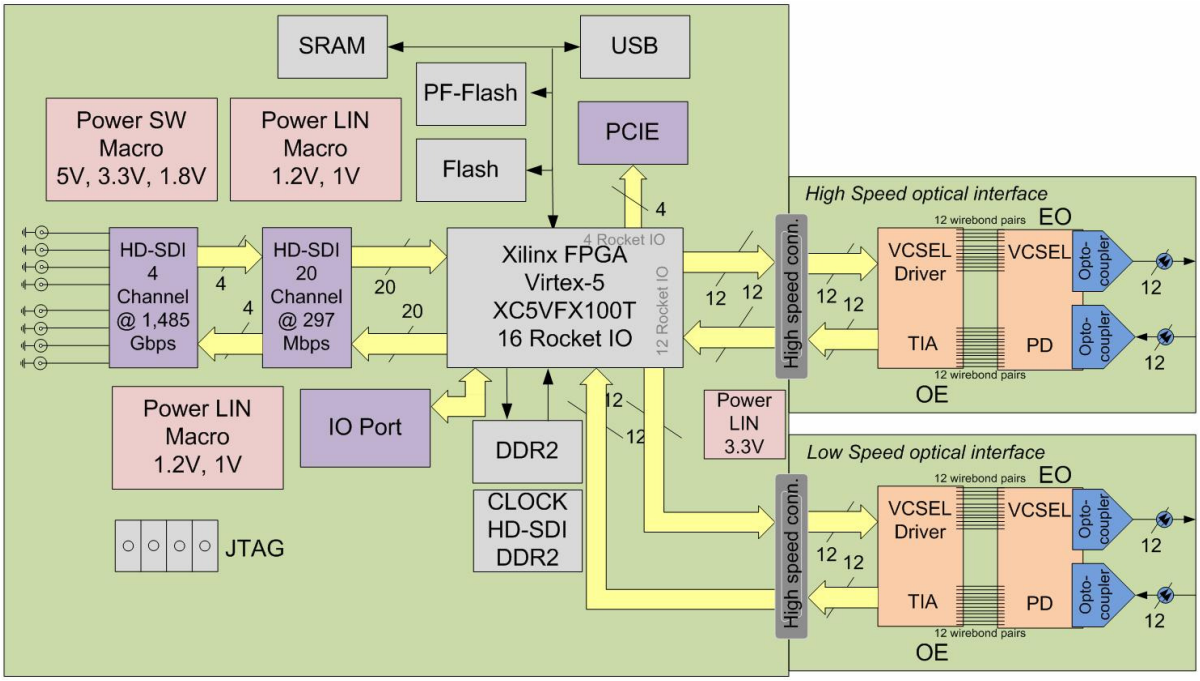

Figure 95. Block diagram of the multi-channel system

The block diagram of the multi-channel system is shown in Figure 95. It is a FPGA (Field Programmable Gate Array) based electronic circuit, which receives four

high-definition video streams over the serial digital interfaces (HD-SDI), shown on the left-hand side of the diagram. A single HD-SDI input, based on SMPTE 274M/SMPTE 296M, with a data rate of 1,485 Gbps is combined with several data streams, comprising four channels each; i.e. 5,94 Gbps. Taking into account some additional data for error checking and control information exchange, the target data rate for this application is considered to be 6.5 Gbps per channel. The system is capable of linking 12 optical channels, for a total bit rate of 71.28 Gbps (without overhead) and 78 Gbps, respectively. This video information can be processed in real time by the FPGA, and produce twelve differently processed video streams per HD-SDI input. This is shown in Figure 96 for one HD-SDI input channel, and for four of twelve possible streams that inflate the original data rate. It is useful for high-definition multi-camera systems in which real-time processing is mandatory; e.g. video control in airports, train stations, etc. The board is equipped with common communication ports such as PCIe, as well as high-speed memories such as DDR2. On the right-hand side, the high-speed drivers of the FPGA are connected over electrical transmission lines made on the PCB. The high-speed connectors allow the transfer of signals from the main board to the optoelectronic PCB, and vice versa.

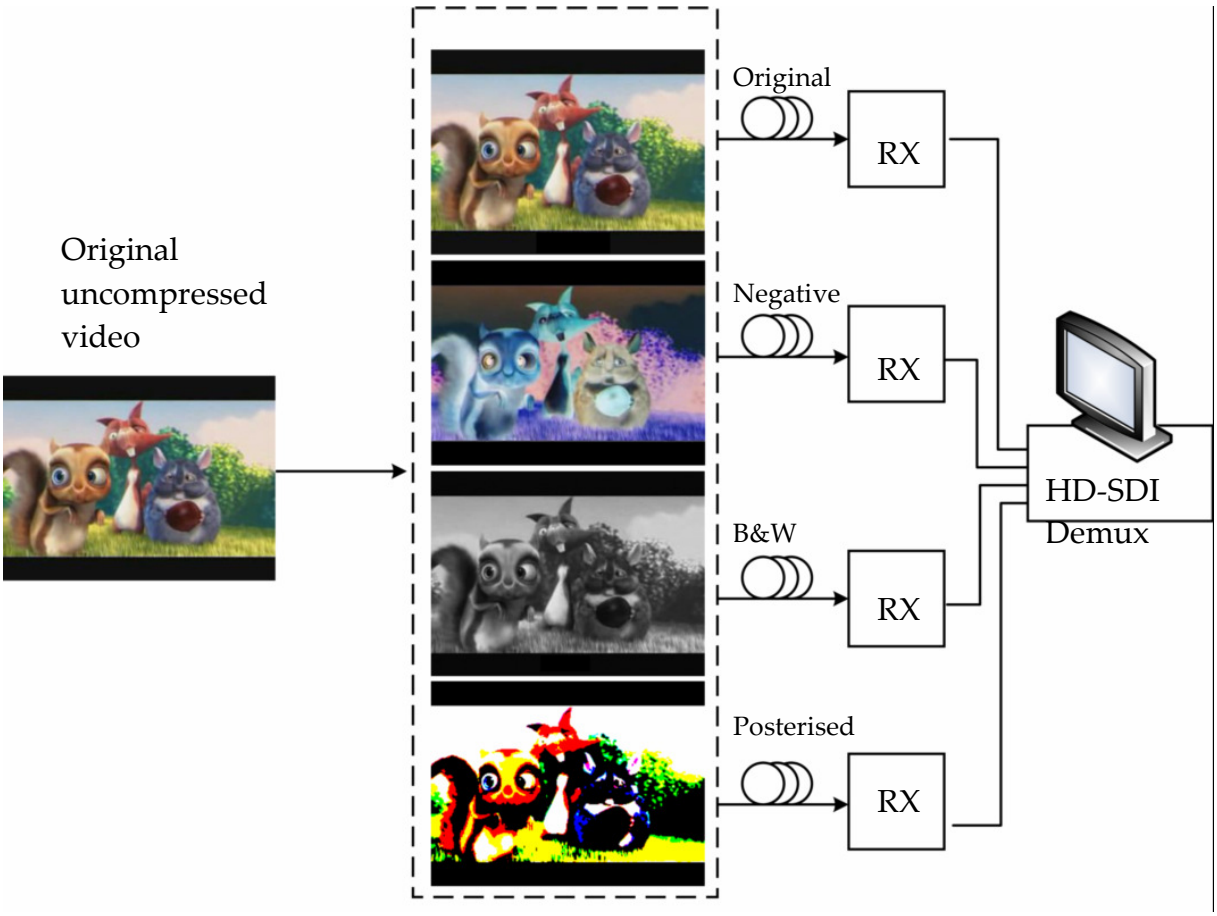

Figure 96. Single-channel uncompressed video transfer and post-processing

5.1.2. Short Description of the Electronic System

5.1.2.1. Electronic System Design

The chosen FPGA has 16 high-speed, low-swing differential serial transceivers, used at a speed of 6.5 Gbps/lane. The high-speed section will be supplied by a stabilised low noise 1.2 V power supply. The FPGA DDR2 I/O block needs a nominal supply voltage of 1.8 V to comply with the DDR2 SODIMM. The high performance 65nm CMOS technology FPGA core requires a 1 V supply. 2.5 V and 3.3 V supply voltages are used for the system clock generator, the general purpose FPGA I/O sections and all other components, such as the HD-SDI, the Flash, SDRAM and USB2.0 devices.

5.1.2.2. Power Supply Stack

In most system-on-board designs, multiple voltage levels are required for powering devices. The supplies for devices are typically low voltages in the region of 3.3 V down to 1 V. At these low power supply voltages, it is important that noise levels be kept to a minimum. Power delivery requirements are more and more challenging, owing to the fact that power and signal integrity are no longer separate issues. Power supply resonances and high dynamic currents will affect the on-chip and off-chip signal quality.

The 3.3 V and 2.5 V supplies are generated from the external 5 V plane supply by a highly integrated 8A switch mode DC/DC power regulator system. The 1.8 V power supply domain is also generated by the 5.0 V plane. The 5.0 V to 1.8 V DC/DC synchronous buck converter provides the DDR2 memory system's voltage domain with a 3-A sink/source tracking linear regulator and buffered low noise reference.

The 1.2 V power supply domain for the FPGA high-speed I/O block requires a stabilised 1.5 V bias. Following the FPGA design guide recommendation, the high-speed I/Os should have separate 1.2 V power supply domains for receiver and transmitter functionality. The intention in using a cascade of switched DC/DC buck converter and linear low drop regulators is to minimise switching noise artefacts, and guarantee a low output impedance voltage source for the noise-sensitive high-speed I/Os. For power and signal integrity, one LDO regulator is used per nibble (= 4 I/Os). The 1 V FPGA core supply is generated by the 3.3 V plane using a high-performance multi-phase switched-mode DC/DC converter topology.
Table 13 summarises the worst case power estimation. Note that the 1.5 V supply includes the 1.2 V supply domain power consumption. The total system power is approximately 55.4 W.

Voltage	3,3 V	2,5 V	1,8 V	1,5 V	1,2 V	1,0 V
Current	2,91 A	2,4 A	8,3 A	4,53 A	4,2 A	18 A
Power	9,6 W	6,0 W	15 W	6,8 W	5,0 W	18 W

Table 13. Worst case power estimation

The schematic contains the ground and power distribution network parasitic elements and all external components. The DC/DC dual buck converter input voltages are blocked with 22µF parallel to 100nF. The device output voltages are decoupled locally, with 47µF in parallel to 100nF. In addition the voltages are blocked at the load with 330µF locally. The 3.3 V worst case load current was estimated with 2.91 A in total. The 2.5 V load current was estimated with 2.4 A in total. The dynamic load current is approximately 500mA for both supply voltage domains.

5.1.2.3. FPGA-based Circuitry

Field programmable gate arrays (FPGAs) possess many advantages compared to ASICs or DSPs, such as flexibility, reprogrammability, performance and affordability. At present, high-speed FPGAs are commercially available, which provide adequate capacity and interfaces for multi-gigabit optical communications. Owing to these advantages, such techniques have already been used widely for sophisticated high-speed signal processing. High-resolution real-time digital video and image processing entails some fast and also complex signal processing in pixel operations, delay of frames, synchronisation, and various other calculations. Thus, it is imperative that HD video signal processing is implemented in real-time on an FPGA platform for the feasibility study described herein.

As already implied, video and image processing involves more than just moving lots of data around the network. In particular, nowadays, latency-critical applications such as live communication, video surveillance, interactive multimedia and medical applications deploy high-performance video solutions on FPGA platforms.

HD video data is received by the FPGA through dedicated HD-SDI interfaces for real-time signal processing, supporting HD video at a resolution of 1920x1080p. The chosen FPGA (i.e. Xilinx Virtex-5 FX100T) has sufficient resources to process several digital video signals in parallel. Taking advantage of parallel processing, the signals can be processed conveniently at a lower clock rate before being serialised to multiple Gbps at the output. Dedicated high-speed IO interfaces (so-called RocketIOs when using Xilinx FPGAs) then deliver the serialised data to the optics. Xilinx RocketIO GTX transceivers can support a line rate of up to 6.5 Gbps.

5.1.2.4. Implemented Logic

After the video signals are received at the FPGA, they are pipelined to perform high-speed image processing and to inflate the data to be transmitted via the optics. Algorithmic functions are applied individually to each pixel of an image and involve a constant operator. In addition, spatial filters and feature detectors are applied, forming an output of N times the input. At a later stage, a multiplexing circuit is implemented and all processed data is recombined for transmission.

All data processing will be implemented by means of VHDL RTL coding. The following mapping of this RTL to the chosen FPGA by maintaining functional equivalence is crucial. Available FPGA resources should not be utilised above 80% at most, owing to potential timing errors and suboptimal logic placement. In any case, debug logic will be added which acts as a chip level logic analyser; i.e. the signals inside the FPGA can be monitored with the help of JTAG without bringing out on FPGA pins.

5.1.3. Measurements

The following eye diagrams were measured in the single-channel version of the constructed systems.

The electrical signal was measured at the output of the FPGA working at a bit rate of 3.25 Gbps. The result is an opened eye diagram: 70% height and 80% width for a BER (Bit Error Rate) of 8.35e-24, which is very low (see Figure 97).

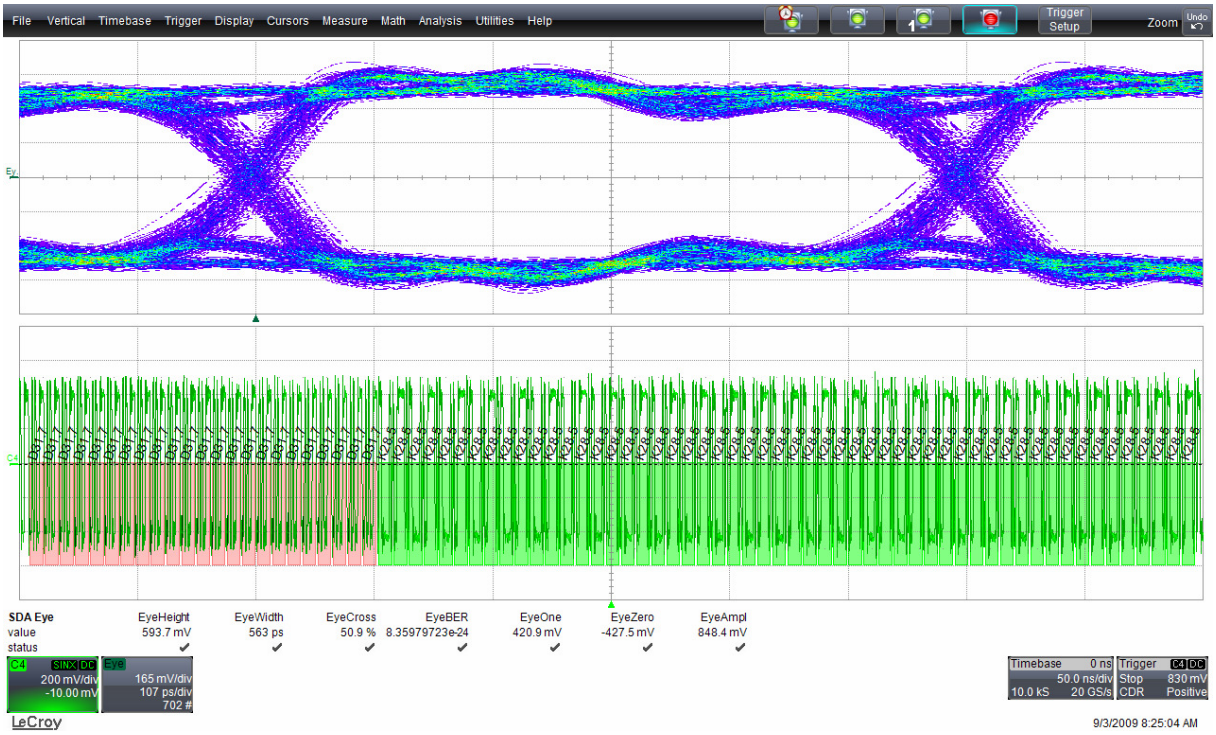

Figure 97. Electrical eye diagram

In spite of a good electrical signal, the optical signal suffered distortion. The electrical signal is afflicted by parasitics, mainly in the electrical path from the VCSEL driver to the VCSEL. The result is a less open eye diagram: 40% height and 45% width for a BER (Bit Error Rate) of 9.2e-12, which is acceptable taking into account that a BER of 1e-12 characterises a standard communication system (see Figure 98).

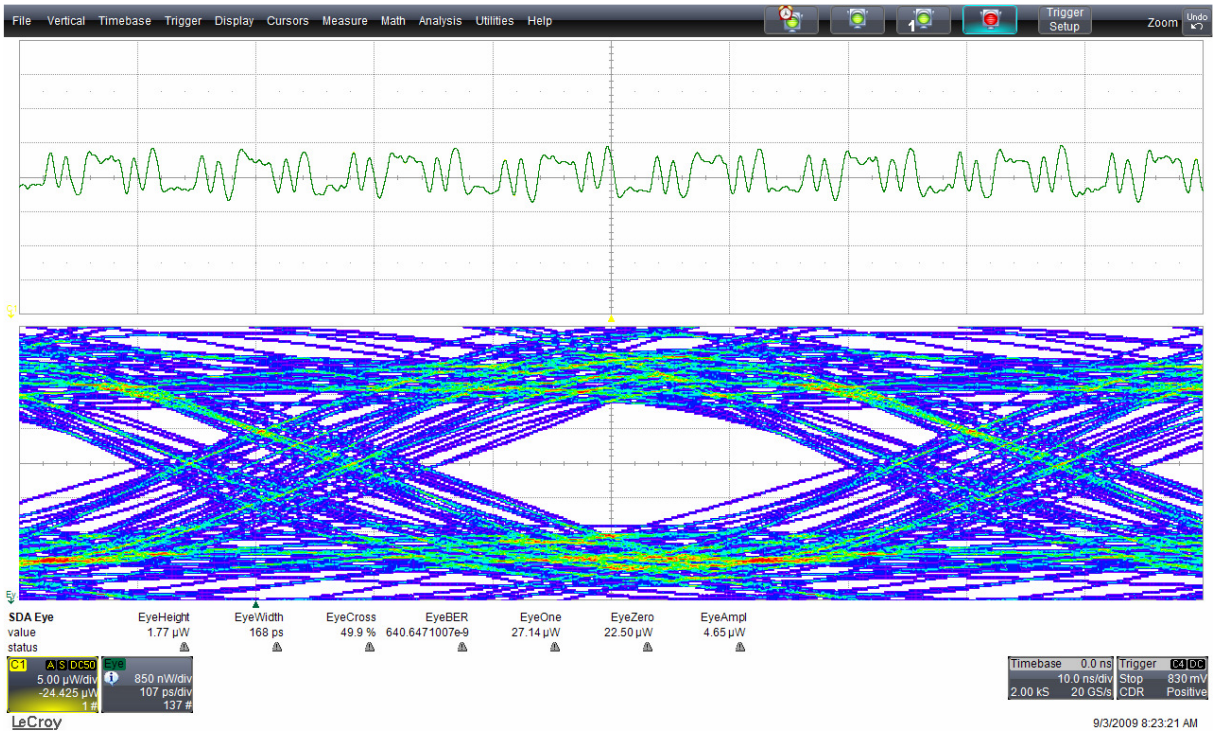

Figure 98. Optical eye diagram

5.1.4. Pictures of the Systems

In order to give an impression about the aspect of the systems, some pictures are included in this section.

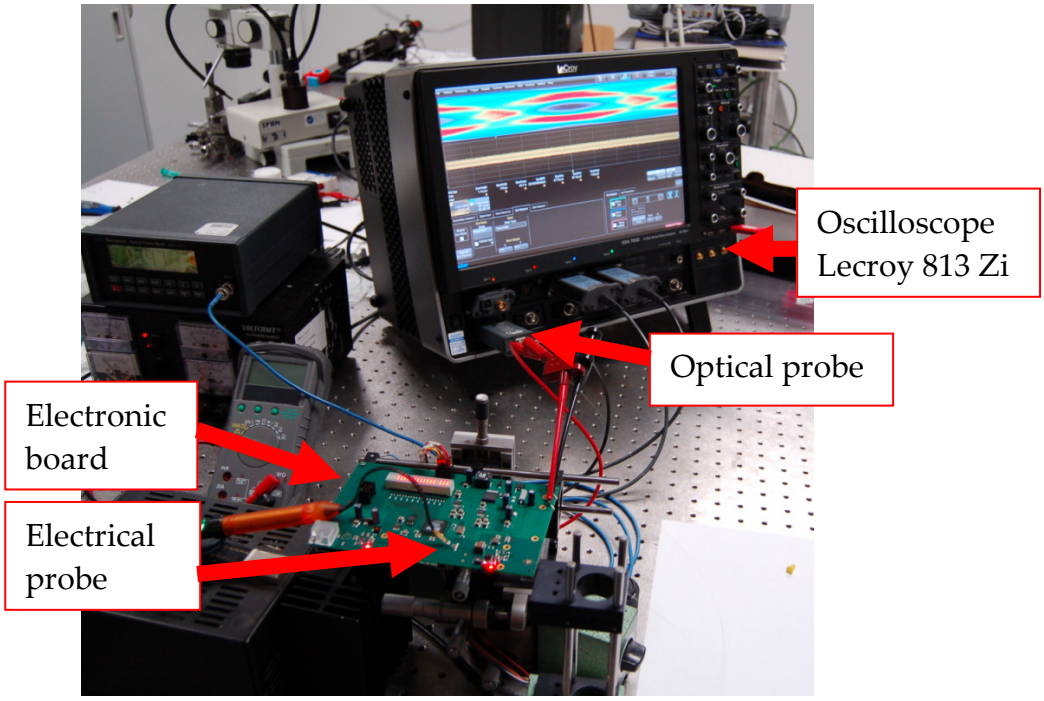

Figure 99. Measurement of the optical eye diagram on the single channel system

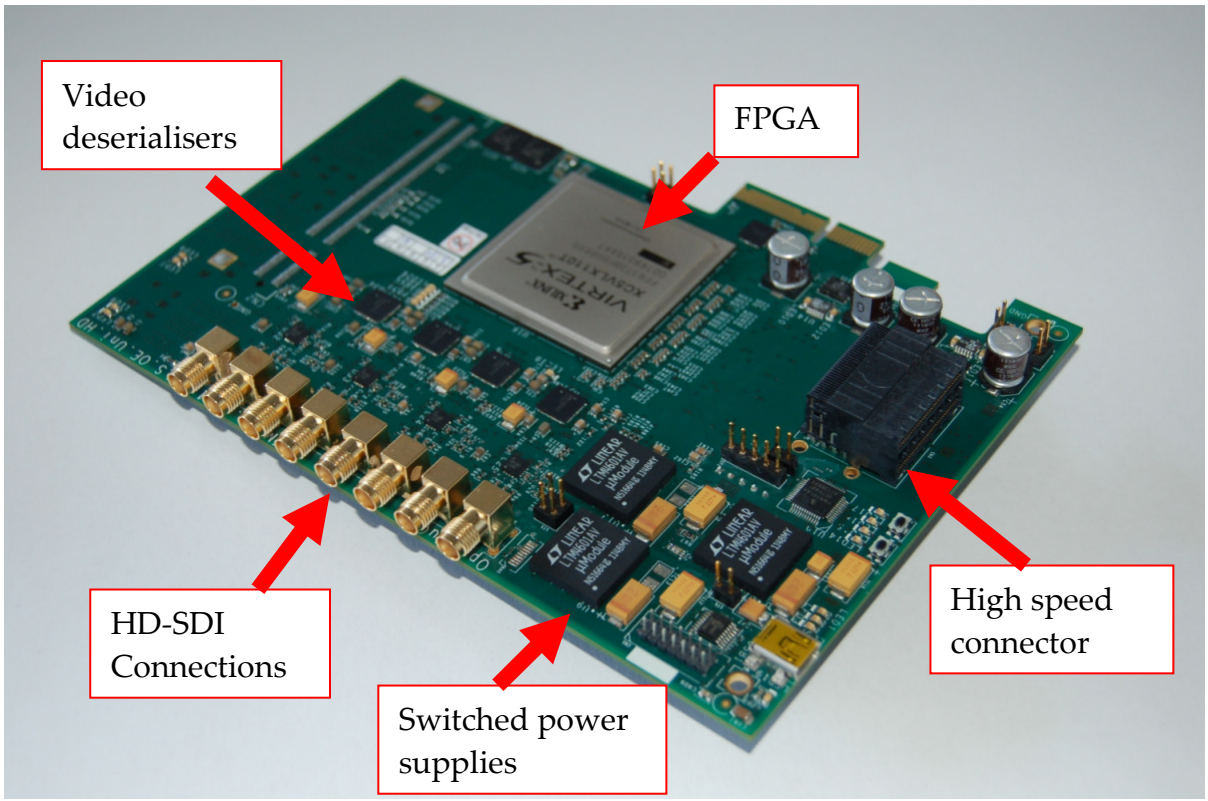

Figure 100. Multi-channel system, top view

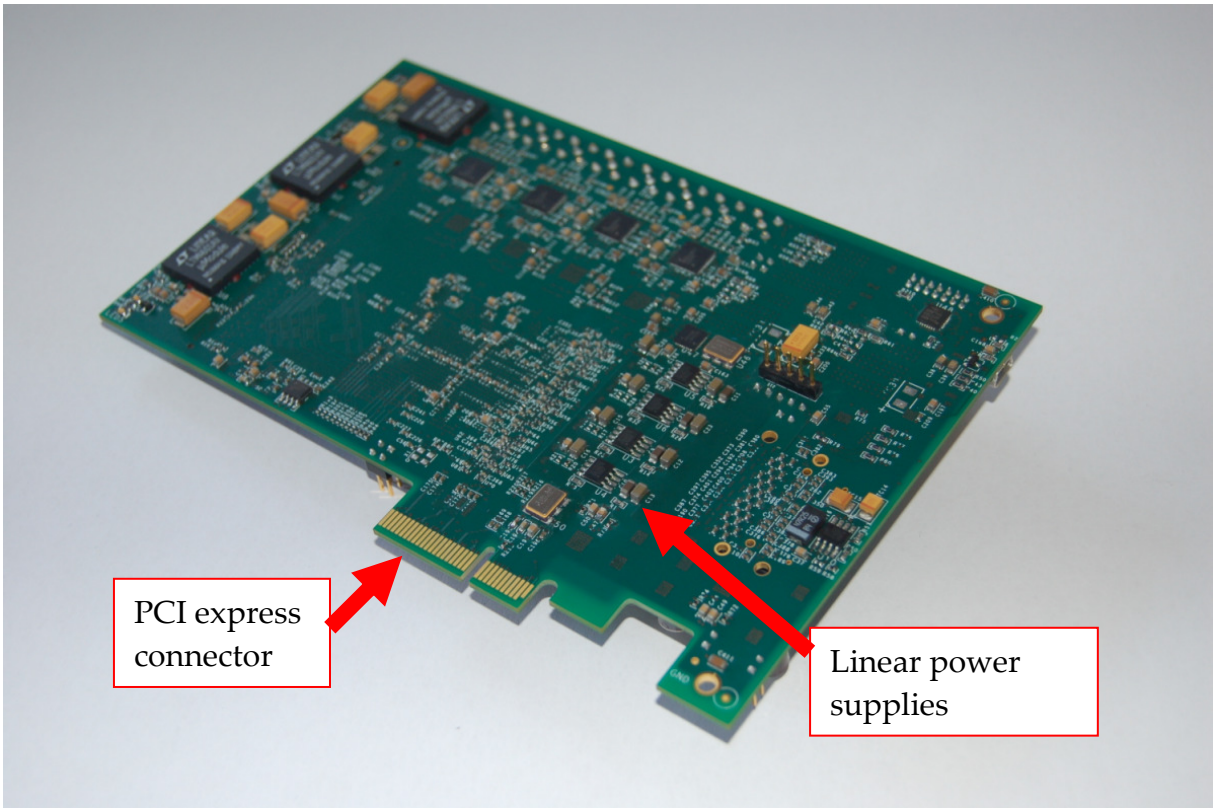

Figure 101. Multi-channel system, bottom view

Of course, the presented systems can be connected using an active optical cable. Indeed, it is done in that way. However, the coupling system can be mounted directly on the main board, or wherever the electronic devices are mounted. The AOC is just a possibility for easily interconnected high-speed electronic systems, but, if desired, the electrical connector can be eliminated by placing the optical devices directly on the main systems.

5.2. Active Optical Cables (AOC)

The term 'active optical cable' suggests the utilisation of both high-speed electronics and optical fibres for the transport of large data volumes. Similar to an USB connector, power is provided through the electrical connect.

In this technology, the transmission rate is limited by the speed of electronics. In an attempt to make the electrical paths shorter, miniaturised electronics are already commercially available. Miniaturisation of electronics succeeds when the discrete devices are replaced by integrated circuitry.

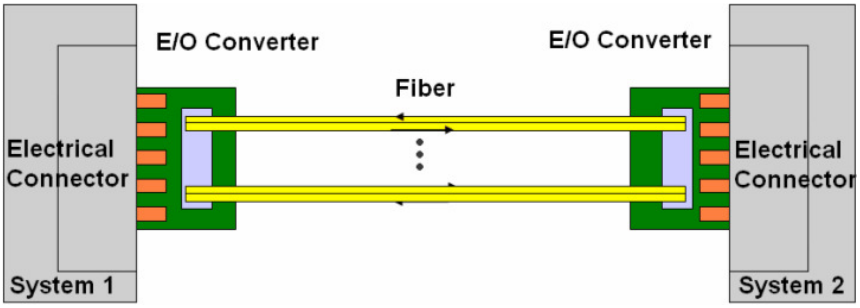

Figure 102. AOC Concept

Through parallelisation of many channels with current transfer speeds — i.e. some Gigabits per second — higher data rates can be reached. In addition, this concept represents a low-cost solution, since commercially available circuitry is used.

There are two main goals in the fabrication of this type of active optical cable: first, an increase of the bandwidth of the cable by parallelisation of several high-speed channels; and second, a reduction in costs and increased ease of handling for these cables, since copper cables for high-speed communications are heavier and more expensive than optical fibres.

Another less important but interesting advantage is the capability of the cable to establish a one-channel communication with a very high speed, or to communicate many channels with the same cable at a high speed. This feature is possible by configuring the logic circuitry inside the connector, without changes in the hardware.

Figure 102 shows the conceptual diagram of the cable. The ends of the cable are provided with electrical connections where several high-speed channels connect to the electronic circuitry. Next to them are the laser diodes and the photodiodes, in the diagram called 'electric-optic converter'.

In Figure 103 and Figure 104 the fabricated AOC is shown.

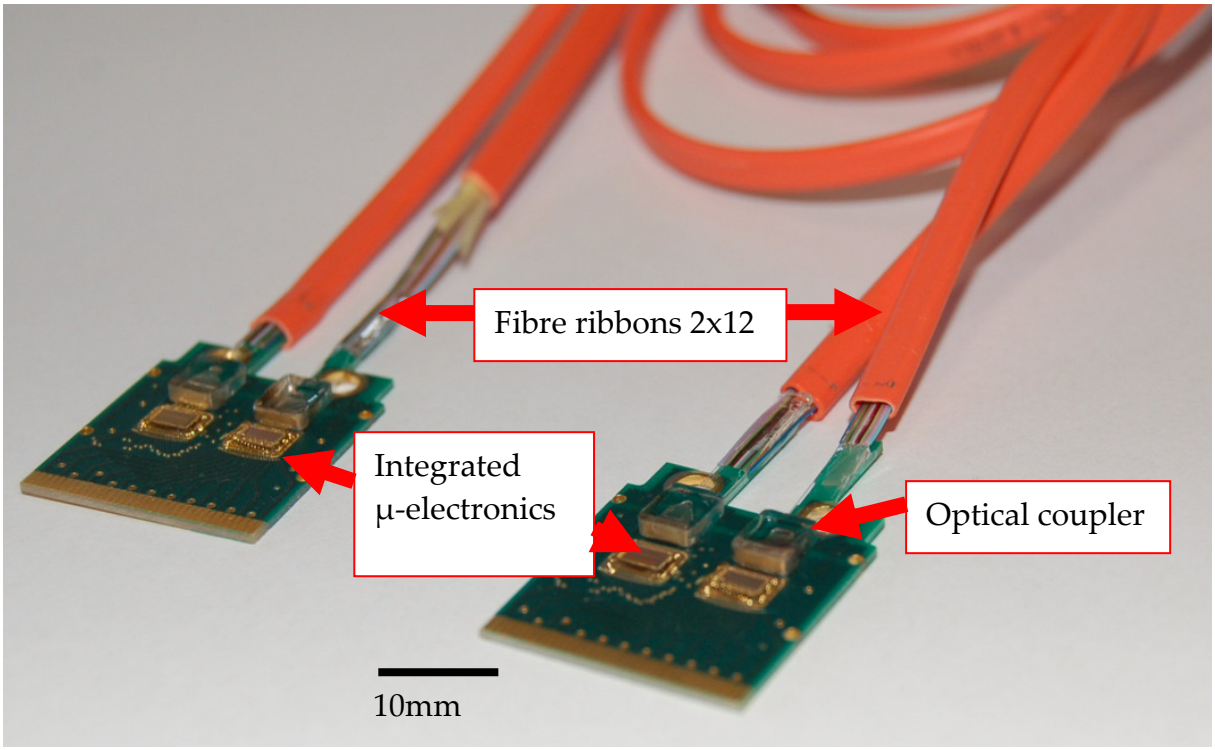

Figure 103. Fabricated AOC

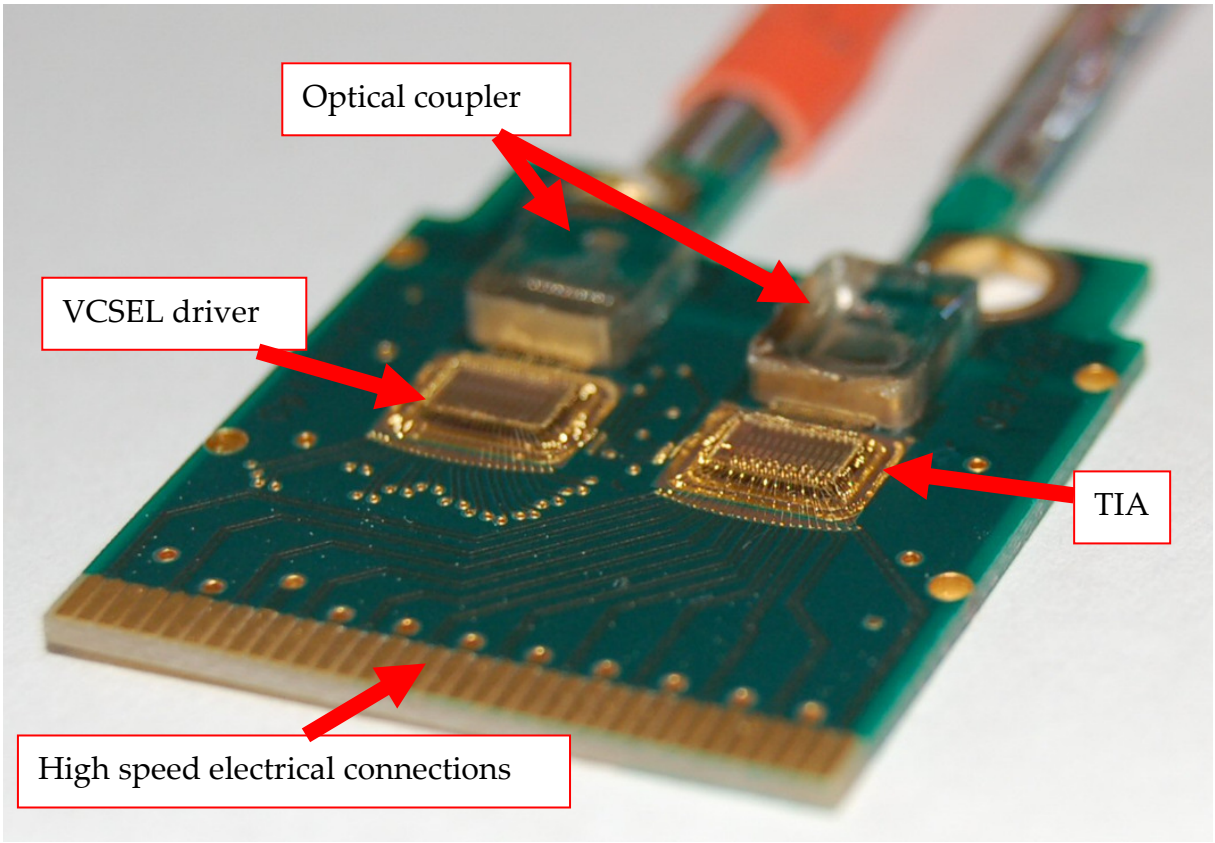

Figure 104. Zoomed image of the fabricated AOC

5.3. Conclusions

- The constructed optical and optoelectronic systems were successfully implemented in applications that supply actual necessities. These applications are state of the art systems for very high speed data transmission.
- Micro optical- and electronic systems were successfully integrated in complex systems. The use of the newest FPGA devices would allow the transmission at higher bandwidths. Remaining within fair compromise between cost and benefit, the constructed system allows a total bandwidth of 78 Gbit/s. It can be raised to 240 Gbit/s by using the newest FPGA devices.

6. Approaches for Micro-Integration of Optical- and Microelectronic Devices

As mentioned previously, in the design of actual and future communication systems, based on optical waveguides, the electronics and optics have to be taken in account equally. Some modern approaches replace the electric transmission lines by optical acrylate-based waveguides [34]. In the system shown in Figure 105, the optical waveguides were made by 'printing' channels in the FPC (Flexible Printed Circuit) that are filled with polymers. Here, there is also the possibility of fabricating optical vias (interlayer connections) by using micromirrors coated with gold.

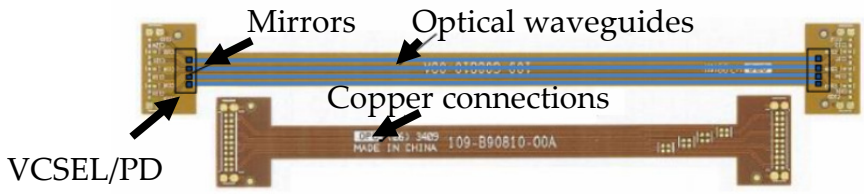

Figure 105. Copper cables replaced by optical waveguides in mobile flex cables

Other systems are designed to integrate optics directly in the electronics and, considering that high temperatures would damage both systems, a thermal design is also needed in many cases [49]. Another important aspect is the compatibility of new systems with standard or available devices. In instances in which new technologies replace current ones, the system design has to be made respecting mechanical guidelines [50].

In this chapter, some approaches for the integration of optical and electronic devices are proposed, as well as possible fabrication methods. They are based on the discussed and used methods for the fabrication of the prototypes.

Proposed approach

For an industrial solution, further requirements concerning the reproducibility and low-cost manufacturability have to be fulfilled. A PDMS master, which can be replicated from a SU-8 lithographic process, is transparent to UV light. This property makes possible the further replication with UV-curable polymers on almost any substrate. The centring could be done prior to curing because of the transparency of the master. A metal master fabricated by micromachining has high reproducibility and accuracy (~1 micron), owing to the hardness of the material. A combination of both advantages could be achieved by microprecision machining of glass.

Figure 106 provides a sketch of the first two steps. Some of the optical and mechanical devices are embedded in the master. Before the replication on the desired substrate, the lenses (optional) and optical fibres are mounted.

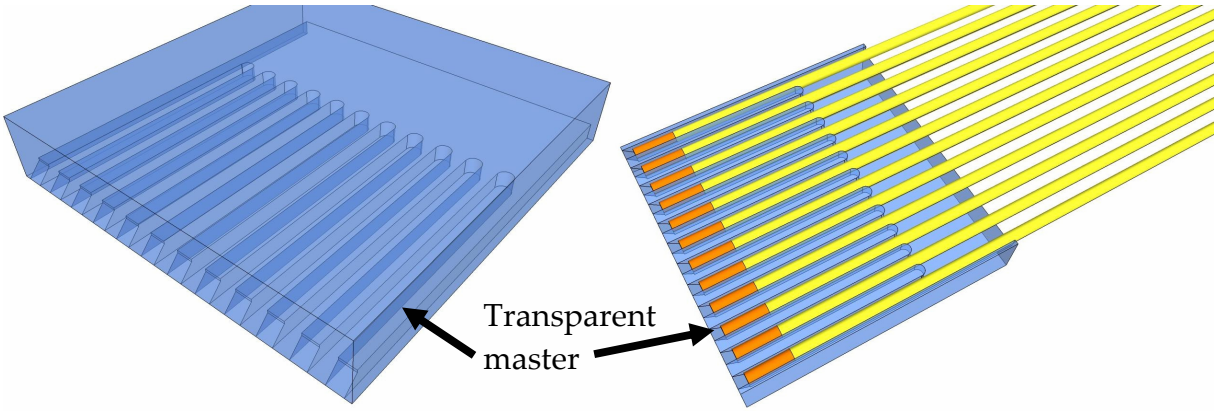

Figure 106. Transparent master and assembled optical devices on the master before replication

In the next step, the liquid polymer is dosed on the desired surface and the master is placed on the glue. The passive adjustment is possible using markers and corresponding mechanical systems (see Figure 107).

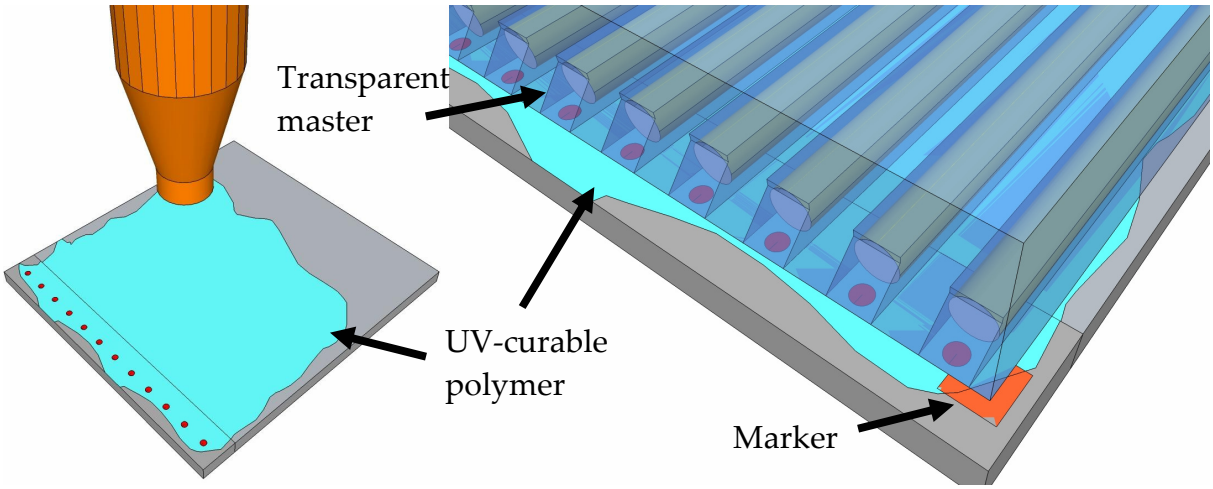

Figure 107. Liquid polymer is dosed on the chip and the master, while the negative shape of the optical coupler is centred using markers

This concept is based on the idea of an integrated chip, in which the VCSEL-array and the driver electronics (or Photodiode-array and TIA) are manufactured in the same wafer, so that long (>3mm) transmission lines are avoided, and higher transmission frequencies are easily achieved.

Figure 108 shows the complete system. The optical coupler is fabricated directly on the integrated circuits [51].

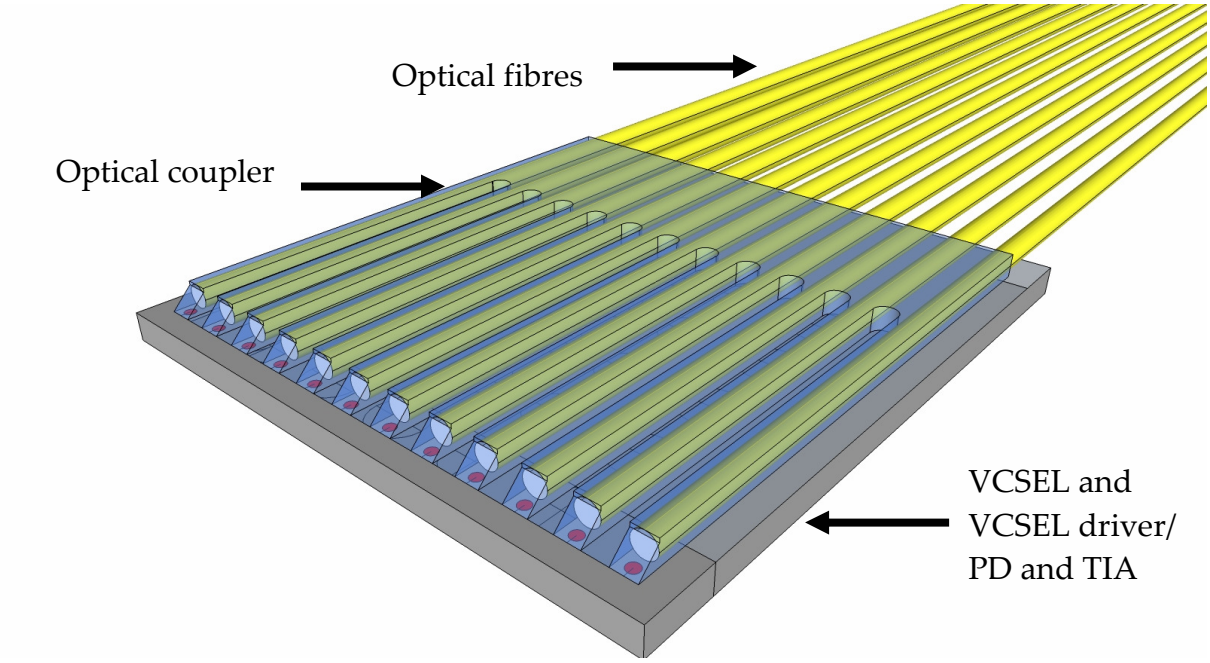

Figure 108. Complete multi-channel system. Integrated VCSEL, drivers and optical devices in one device

The advantage of this system is clearly the easy handling for the population of PCBs in commercial applications, since current methods can be used. The chip is connected by BGA (Ball Grid Array) and can be assembled on any PCB (see Figure 109).

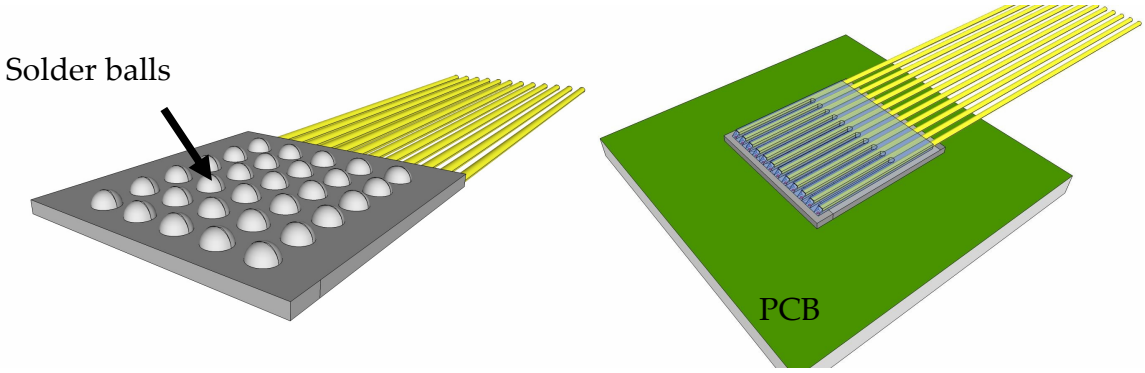

Figure 109. BGA for the connection of the chip to a PCB and complete system on a PCB as currently is done

This concept could be integrated into the developing 3D package, in which several functional blocks are integrated in different stages.

In the near future (2014), 3D packages with 4 stages will be available. A further challenge could be the integration of optoelectronics and optics in the same package.

Figure 110 provides a sketch of the 3D-package. The computing power, memory and high-speed communication systems are embedded in a single package.

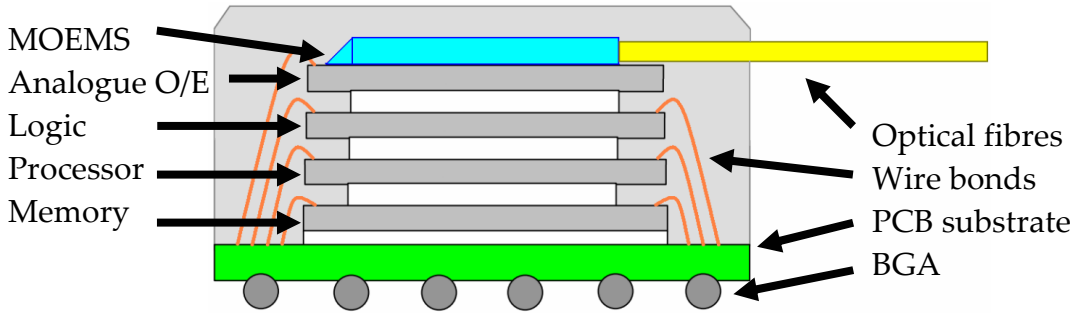

Figure 110. 3D-package with integrated high speed optical channels

7. Summary

In this thesis, the monolithic construction, and the simulation and integration of optical microcouplers were investigated. First, with regard to the components, the complete communication path was described. The output stage of a high-speed digital device was taken as the source of the electrical signal that was transmitted over different electrical transmission lines and high-speed connectors. In order to design a system that fulfils the required characteristics, the most critical factors were determined, and their effects minimised. For example, the number of contacts through the PCB (vias) were minimised, 'vias' configurations such as GSSG (Ground-Signal-Signal-Ground) were used, and the length of the electrical connections were kept as short as possible.

On the optical side, a novel coupling concept, based on the use of VCSELs, was presented. Some characteristics of the VCSEL that makes it attractive are: low power consumption; small form factor; arrays' availability; and emission in the same direction as oscillation inside the resonator. The basic idea of the design is the conservation of a flat construction, by redirecting the outgoing beam from the VCSEL by 90 degrees. The optical coupler integrates micro-optical and micromechanical devices in a monolithic substrate. It is made using polymeric replication of moulds. The mould or master with the negative shape of the coupler was fabricated in aluminium and steel, using hard metal micromachining. A standard HSC machine was fine tuned, and its error minimised in order to achieve the required accuracy. After milling the mould, the optical surfaces were polished. On the mirrors, the roughness of some tens of nanometres was measured.

For the replication of the master an UV polymer was used. The ability of this polymer to replicate moulds with a high accuracy is a result of its very low viscosity. After the exposure of the polymer to UV radiation the monolithic optical device was obtained. Owing to the propagation in air of the optical signal, the mirrors had to be coated with silver to increase their reflectivity.

The optical coupling system was simulated using an angular spectrum-based simulation tool, in which a novel method for propagation between tilted planes was implemented. This tool was important for the definition of tolerances in the fabrication process of the coupler, and in the adjustment system for the integration of the coupler and the electronic systems.

For the test of the optical coupler, an electronic system was designed and constructed. A multi-channel communication system based on FPGA technology processes multiple HD-video streams in real time, and generates up to 48 new streams that are transmitted over the optical links. The system has another standard port, such as PCIe, for embedding the system in a personal computer.

The system is purely electronic. The electrical signal is transmitted to a high-speed connector, into which the active optical cable is plugged.

The active optical cable was designed, based on the use of wire bonds for the interconnection of electronic devices, as well as for their connection with the PCB. Wire bonding is a well-known technique for the population of PCBs with bare-die electronic devices. The conversion of the electrical signal into an optical one succeeds inside a small PCB where electronics, optics and mechanics are integrated.

The integration concept is based on a modular construction that aims to test the electronics and the optical systems separately.

At the design phase of both the electronics and optical coupler, the integration methods were taken into account. Markers on the PCB and spacers in the optical coupler were defined accurately, in order to ease the integration of the different devices, and guarantee operational reliability.

At the end of the document, in the chapter 8, some models of possible future constructions were presented as a prospect for further developments. The integration of electronic and optical systems at chip level, using effective coupling methods, is inevitable when designing and constructing future high-speed communication system in the short-haul range.

References

[1] V J. Jahns, K.-H. Brenner, W. Däschner, C. Doubrava, T. Merklein: "Replication of diffractive microoptical elements using a PMMA molding technique", Optik 89, No. 3, 98 - 100, (1992)

[2] K.-H. Brenner, M. Kufner, S. Kufner, J. Moisel, A. Müller, S. Sinzinger, M. Testorf, J. Göttert, J. Mohr: "Application of three-dimensional micro-optical components formed by lithography, electroforming, and plastic molding", Appl. Opt. 32, No. 32, 6464 - 6469, (1993).

[3] G. Bagordo, K.-H. Brenner, T. Merklein, A. Rohrbach: "Fabrication of Micro-Optic Elements by UV-initiated Polymerisation", in "Integrated Optics and Micro-Optics with Polymers", Ehrfeld, Wegner, Karthe, Bauer, Moser editors, Teubner-Texte zur Physik, Band 27, 177 - 192, (1993)

[4] S. Sinzinger, K.-H. Brenner, J. Moisel, T. Spick, M. Testorf, "Astigmatic gradient-index elements for laser-diode collimation and beam shaping", Appl. Opt. 34, No. 29, 6626 - 6632, (1995)

[5] J. Moisel, C. Passon, J. Bähr, K.-H. Brenner, „Homogeneous concept for the coupling of active and passive single-mode devices utilizing planar gradient-index lenses and silicon-V-grooves“, Appl. Opt. 36, No. 20, 4736 - 4743, (1997)

[6] J. Bähr, K.-H. Brenner, "Optical motherboard: a planar chip to chip interconnection scheme for dense optical wiring", in Optics in Computing '98, Proceedings of SPIE 3490, 419 - 422, Bruegge (1998)

[7] U. W. Krackhardt, R. Klug, K.-H. Brenner, "Faser-optische Kurzstreckenverbindungen zur breitbandigen und parallelen Signalübertragung", ORT 1999, Tagungsband 4. Workshop Optik in der Rechentechnik, ISSN 1437-8507, 10 - 15, Jena (1999)

[8] U. W. Krackhardt, R. Klug, and K.-H. Brenner, "Multimode Fiber Interconnect for Parallel, High Bandwidth - Short Distance Data Link", in Progress in Electromagnetics Research Symposium (PIERS), The Electromagnetics Academy, PIERS 2000 Proceedings, 726, ISBN 0-9679674-0-6, Cambridge, Massachusetts, USA (2000)

[9] J. Bähr, T. Schmelcher, K.-H. Brenner, "Tolerant Coupling of integrated Multimode Waveguides", in LEOS 2000, IEEE Annual Meeting Conference Proceedings, Vol. 2, 571 - 572, ISBN 0-7803-5947-X, Puerto Rico (2000)

[10] Ulrich Krackhardt, Karl-Heinz Brenner, „Integrated Guiding Structures for automatic Alignment of micro optical Components“, SPIE 46. Annual Meeting, Gradient Index, Miniature, and Diffractive Optical Systems II, Proceedings of SPIE, Vol. 4437, 91 – 98, ISSN 0277-786X/01, San Diego (2001)

[11] V. Gopalakrishnan, S. Bhattacharjee, K.K. Ramakrishnan, R. Jana, and D. Srivastava. "CPM: Adaptive Video-on-Demand with Cooperative Peer Assists and Multicast", in Proc. INFOCOM, 2009, pp.91-99.
[12] Ali M. Niknejad. Electromagnetics for high-speed analog and digital circuits. Cambridge University Press, 2007.
[13] Paul R. Gray and Robert G. Meyer. Analysis and Design of Analog Integrated Circuits. New York: John Wiley, 3rd edition, 1993.
[14] Howard W. Johnson, Martin Graham. High-Speed Digital Design, a handbook of black magic. Prentice Hall, 1993.
[15] James C. Rautio. Microstrip Conductor Loss Models for Electromagnetic Analysis. IEEE transactions on microwave theory and techniques, vol. 51, no. 3, march 2003.
[16] Lisha Li, Sripriya Raghavendran, and Donald T. Comer. "CMOS Current Mode Logic Gates for High-Speed Applications". 12th NASA Symposium on VLSI design, Idaho, USA, 2005.
[17] Sutono A., Cafaro, Laskar, Tentzeris. Experimental Study and Modeling of Microwave Bond Wire Interconnects. IEEE AP-S Interconnect and Packaging, Salt Lake City, USA, 2000.
[18] M. Kirschning and R. H. Jansen. ``Accurate Wide-Range Design Equations for the Frequency-Dependent Characteristic of Parallel Coupled Microstrip Lines,'' IEEE Transactions on Microwave Theory and Techniques, vol. 32, no. 1, pp. 83-90, Jan. 1984
[19] Sadiku, Matthew N. O.. Elements of Electromagnetics (1st ed.), Saunders College Publishing, 1989.
[20] I. Novák, B. Eged and P. Bajor. Crosstalk Reduction on Stripline Printed Circuit Boards with additional Center Traces, International Symposium on Electromagnetic Compatibility, May 17-19, Sendai, Japan, 1994.
[21] K.C. Gupta, Ramesh Garg and Rakesh Chadha . "Computer-Aided Design of Microwave Circuits", Artech House 1981
[22] Alwayn Vivek. Optical Network Design and Implementation. Cisco Press, Networking Technology, 2004.
[23] Fumio KOYAMA. VCSELs: Their 30 Years History and New Challenges. Optoelectronic Materials and Devices III, Proc. of SPIE Vol. 7135, 2008.
[24] P. Bhattacharya. Semiconductor Optoelectronic Devices, 2nd edition. Prentice Hall, 1997.
[25] S. Prasad, H. Schumacher, A. Gopinath. High-Speed Electronics and Optoelectronics. Cambridge, 2009.
[26] Chuang S.L.. Physics of Optoelectronic Devices. John Wiley & Sons, 1995.
[27] K.-H Brenner. Skript zur Vorlesung „Introduction to Photonics". Lehrstuhl für Optoelektronik, ziti, Universität Heidelberg, 2011.
[28] C. Wilmsen, H. Temkin, and L. Coldren. Vertical-Cavity-Surface-Emitting Lasers. Cambridge University Press, 1999.

[29] Taylor H. F., Ekonoyan O., Park C. S., Choi K. N., Chang K., Traveling-wave photodetectors. SPIE Optoelectronics Signal Processing for Phased Array Antennas II, 59-63, 1990.
[30] A.W. Synder and J.D. Love. Optical Waveguide Theory. Chapman and Hall, London, 1983.
[31] E. Hecht. Optik. 3. Auflage. Oldenburg, 2001.
[32] Shigeru Kawai. Handbook of optical interconnects. Taylor and Francis Group, 2005.
[33] Stéphane Bernabé, Christophe Kopp, Laurent Lombard and Jean-Marc Fedeli. Microelectronic-like packaging for silicon photonics : a 10 Gbps multi-chip-module optical receiver based on Ge-on-Si photodiode. Proceedings ESTC Optoelectronics, Berlin. 2010.
[34] M.Immonen, J.Wu, P.Chen, Y.H.Luo, H.He, W.Huang, J.X.Xu, T.Rapala-Virtanen. Active Optical Flex Module for Ultra-Short Distance Data Applications. Proceedings ESTC Optoelectronics, Berlin. 2010.
[35] K. Matsushima, H. Schimmel, F. Wyrowski, “Fast calculation of optical diffraction on tilted planes by use of the angular spectrum of plane waves“, J. Optical Society of America, Vol.20, N. 9, p.1755/ September 2003.
[36] K.-H. Brenner, Aspekte der Lichtausbreitung zwischen verkippten Ebenen. DGaO-Proceedings (Online-Zeitschrift der Deutschen Gesellschaft für angewandte Optik e. V.),ISSN: 1614-8436, 112. Jahrestagung in Ilmenau, (2011).
[37] Hsing T. R., Imaging system using gradient index fibers Fiber Optics. J C Daly (Boca Raton, FL: CRC Press), 1984.
[38] F C McNeillie, J Thomson and I S Ruddock. The imaging properties of gradient index optical fibres. Eur. J. Phys. 25 (2004) 479–487
[39] D. Wohlfeld. Dissertation. Combined faculties for the natural sciences and for mathematics of the Ruperto-Carola University of Heidelberg, Germany, 2009.
[40] S. Sinzinger and J. Jahns. Microoptics. Wiley VCH, 1999.
[41] U. Berger, L. Cardon, "The Application of Standard HSC Milling Machine Tools for Micro Fabrication", 3rd international conference polymers & moulds innovations, Ghent, Belgium, 17th -19th September 2008, proc. pp. 50-55.
[42] Boerret, R., Klingenmaier, J., Berger, U., et al., "Minimized process chain for polymer optics," Proceedings of SPIE Vol. 7061, 706118 (2008).
[43] K.-H. Brenner, M. Kufner, S. Kufner, J. Moisel, A. Muller, S. Sinzinger, M. Testorf, J. Göttert, and J. Mohr, "Application of three-dimensional micro-optical components formed by lithography, electroforming and plastic moulding", Appl. Opt. 32, No. 32, 6464 - 6469, (1993)
[44] Andreas Georg, Wolfgang Graf, Werner Platzer. Korrosionsmechanismus von low-e Schichten mit Silber als IR-Reflektor. Fraunhofer Institut für Solare Energie Systeme, Jahres Bericht 2010.

[45] Carl Wilsmsen, Henryk Temkin and Larry A. Coldren. Vertical-Cavity Surface-Emitting Lasers. Cambridge studies in modern optics, 1999.
[46] K.-H Brenner. Skript zur Vorlesung „Grundlagen der Optik“. Lehrstuhl für Optoelektronik, Universität Mannheim, 2007.
[47] Refractive Index Reference - P. Winsemius, F. F. van Kampen, H. P. Lengkeek, and C. G. van Went, J. Phys. F 6, 1583 (1976)
[48] Xiyuan Liu, Karl-Heinz Brenner, “Guide structures for splicing single-mode fibres fabricated using deep lithography”, Photonik international 2009/2, pp. 42-43, (2009)
[49] Marc de Samber1, Eric van Grunsven1, Erik Eggink1 and Wil Peels2 , 1 Philips Applied Technologies, 2 Philips Lighting LightLabs. Integrated LED modules. ESTC 2010 (Electronics System Integration Technology Conferences), Digital Proceedings, p0072 (2010)
[50] Jörg- R. Kropp1, James A. Lott1, Nikolay N. Ledentsov1, Pavel Otruba2, Karsten Drögemüller3, Gerrit Fiol4, Dieter Bimberg4, Ivan Ndip5, Robert Erxleben5, Uwe Maaß5, Matthias Klein5, Günter Lang5, Hermann Oppermann5, Henning Schröder5 and Herbert Reichl5. A small form-factor and low-cost opto-electronic package for short-reach 40 Gbit/s serial speed optical data links. 1VI Systems GmbH, 2EZconn Europe GmbH, 3ix-cad GmbH, 4Inst. für Festkörperphysik TU-Berlin, 5 Fraunhofer IZM Berlin, Germany. ESTC 2010 (Electronics System Integration Technology Conferences), Digital Proceedings, p0311 (2010)
[51] Patent: D. Wohlfeld, K.-H. Brenner, U. Brüning, „Über optische Verbinder und dessen Herstellung“ UHD07a, DE 10 2010 018 248.6
[52] C. C. Sun, C. Y. Chen, H. Y. He, C. C. Chen, W. T. Chien, T. X. Lee and T. H. Yang, “Modeling the radiation pattern of LEDs,” Optics Express 16, 20060-20066 (2008)
[53] N. Tran, F. Shi. “LED package design for high optical efficiency and low viewing angle”Microsystems, Packaging, Assembly and Circuits Technology, 2007. IMPACT 2007. Conference Publications, p.10-13.

Acknowledgements

Foremost, I would like to express my gratitude to my advisor Prof. Dr. K.-H. Brenner for the continuous support of my Ph.D study, research and the execution of my projects, for his patience, motivation, and immense knowledge. His guidance helped me in all the time of research.

Besides my advisor, I would like to thank the rest of my thesis committee: Prof. Dr. J. Jahns and Prof. Dr. U. Brüning for their encouragement and insightful comments.

My sincere thanks also goes to Dr. D. Wohlfeld, Dr. C. Kreidel and F. Lemke, for their support on the design and construction of the optical- and electronic- systems.

I thank my fellow in the chair for optoelectronics: Dr. X. Liu, M. Auer, E. Slogsnat and T. Stenau for the stimulating discussions, for their support in special situations, and for all the fun we have had in the last four years. Also I thank W. Stumpfs who often made me look farther than the walls in my office and also for his support. I also thank Mrs. Volk for the organisation of the trips to the conferences and the administrative support of my projects.

Last but not the least, I would like to thank my family: my parents Rebeca and Emiliano, for giving birth to me at the first place and supporting me spiritually throughout my life. My sister Liliana and my brother Oscar for their support to me and Dimitriya, specially when I had to be abroad. Thank you my loved Dimitriya for giving me the strength and motivation to keep walking forward. Your love give me the calm to follow my goals. Thank you my loved sons Leo and Dani: one day you will discover that all my actions, including this step on the infinite stairs of knowledge, are motivated by each manifestation of your love. Love and physics maintain the world working as it should.

About the author

José Fernando Merchán Alba was born September 1., 1978, in Bogotá D.C., Colombia. He studied electronic engineering at the "Pontificia Universidad Javeriana" in Bogotá and obtained his diploma in 2003. His diploma thesis was made in digital image processing with the title: "Form, colour and texture extraction for the classification of coffee beans". In the same year he moved to Germany. In the winter semester he began the master of science in information technologies at the Mannheim university of applied sciences and obtained the M.Sc. degree in 2006. His master thesis was made in electronic design with the title: "Design and fabrication of a transimpedance amplifier for an OCT (Optical Coherence Tomography) system". For almost three years in the German industry, he developed digital and analogue electronic systems for OCT systems. 2008 began his Ph.D. work at the chair of optoelectronics at the university of Mannheim, Germany.

List of publications

- F. Merchán, D. Wohlfeld, K.-H. Brenner, "High speed communication using micro optical integration", DGaO-Proceedings (Online-Zeitschrift der Deutschen Gesellschaft für angewandte Optik e. V.), ISSN: 1614-8436, 110. Jahrestagung in Brescia/Italien, (2009)
- F. Merchán, D.Wohlfeld, K.-H. Brenner, " Development of active optical cables", Workshop of Optics in Computing (Optik in der Rechentechnik, ORT), Proceedings of the Workshop Optics in Computing 2009, ISBN 978-3-200-01636-1, pp 45 – 47, Wien (2009)
- D.Wohlfeld, F. Merchán, K.-H. Brenner, "Integrated VCSEL to fiber couplers fabricated with micro-machining", World of Photonics congress, Manufacturing of Optical Components, 2009, Munich, Germany
- F. Merchán, D. Wohlfeld, K.-H. Brenner, "Micro integration of optical components for the fabrication of active optical cables", Journal of the European Optical Society - Rapid Publications Vol. 5, Pub.nr. 10056 (2010)
- F. Merchan, X. Liu, K.-H. Brenner, "Effiziente Faserkopplung mit Gradientenindex-Stablinsen", DGaO-Proceedings (Online-Zeitschrift der Deutschen Gesellschaft für angewandte Optik e. V.), ISSN: 1614-8436, 111. Jahrestagung in Wetzlar, (2010)
- F. Merchán, K.-H. Brenner, R. Börret, U. Berger, „Cost optimized fabrication of Micro-Optical Couplers", Optical Fabrication and Testing (OF&T), OSA, 13.-16-06.2010, Jackson Hole, Wyoming, USA, (2010). ISBN 978-1-55752-893-3, OWC3: OSA / IODC/OF&T 2010

- F. Merchán, Karl Heinz Brenner, Peter Gregorius, Sven Hendrik Voß, “FPGA-Board and Active Optical Cable Design for Multi-Gigabit Communication”, ESTC 2010 (Electronics System Integration Technology Conferences), Digital Proceedings, poster session 1, p0032 (2010)
- F. Merchán, K.-H. Brenner, "A concept for the assembly and alignment of arrayed microelectronic and micro-optical systems for Optical Multi-Gigabit Communication", Optoelectronic Interconnects and Component Integration XI Conference OE112, 22.-27.01.2011, San Francisco, California, USA, Proc. of SPIE Vol. 7944, 79440D · © 2011 SPIE
- F. Merchán, K.-H. Brenner, P. Gregorius, S.-H. Voß, „FPGA-Board and Active Optical Cable Design für optische Multi-Gigabit Übertragung“, PLUS 12 / 2010 (Produktion von Leiterplatten und Systemen / Fachzeitschrift für Aufbau u. Verbindungstechnik in der Elektronik, Leuze Verlag), Band 12, ISSN 1436-7505 B 49475, pp. 2800-2809, (2010)
- F. Merchan, K.-H. Brenner, “Neuartiges Integrationskonzept für kostengünstige Herstellung optischer Mikrosysteme”, DGaO-Proceedings (Online-Zeitschrift der Deutschen Gesellschaft für angewandte Optik e. V.),ISSN: 1614-8436, 112. Jahrestagung in ilmenau, (2011)